

**NANO - CONFINED WATER IN ELECTRIC
FIELD: STRUCTURE, RESPONSE AND
PROPERTIES**

A Thesis Submitted
To
Sikkim University



**In Partial Fulfilment of the Requirement for the
Degree of Doctor of Philosophy in Physics**

By
Smita Rai
Department of Physics
School of Physical Sciences

May 2024

6 माइल, सामदुर, तादोंग -737102
गंगटोक, सिक्किम, भारत
फोन-03592-251212, 251415, 251656
टेलीफैक्स -251067
वेबसाइट - www.cus.ac.in



सिक्किम विश्वविद्यालय
SIKKIM UNIVERSITY

6th Mile, Samdur, Tadong -737102
Gangtok, Sikkim, India
Ph. 03592-251212, 251415, 251656
Telefax: 251067
Website: www.cus.ac.in

(भारत के संसद के अधिनियम द्वारा वर्ष 2007 में स्थापित और नैक (एनएएसी) द्वारा वर्ष 2015 में प्रत्यायित केंद्रीय विश्वविद्यालय)
(A central university established by an Act of Parliament of India in 2007 and accredited by NAAC in 2015)

DECLARATION

I, **Smita Rai**, hereby declare that the thesis titled “**NANO - CONFINED WATER IN ELECTRIC FIELD: STRUCTURE, RESPONSE AND PROPERTIES**” submitted by me for the award of the degree of **Doctor of Philosophy** to the Department of Physics, Sikkim University, is my original work. This work has been carried out by me under the supervision of **Dr. Dhurba Rai** at the Department of Physics, Sikkim University. I confirm that all sources used in this research have been properly acknowledged and cited.

This thesis has not been submitted for any other degree to any other university or institute.

Smita Rai

Smita Rai

Roll No.: 17PDPY01

Regn. No.: 17/Ph.D/PHY/01

Place: Gangtok, Sikkim

Date: 19/05/24

It is recommended that this thesis be placed before the examiners for evaluation.

Dhurba Rai

सहायक प्राध्यापक
Assistant Professor
भौतिकी विभाग
Department of Physics
सिक्किम विश्वविद्यालय
Sikkim University

Dr. Dhurba Rai
(Supervisor)

Assistant Professor

Department of Physics

School of Physical Sciences

Sikkim University

Date 17 May 2024

6 माइल, सामदुर, तादोंग -737102
गंगटोक, सिक्किम, भारत
फोन-03592-251212, 251415, 251656
टेलीफैक्स -251067
वेबसाइट - www.cus.ac.in



सिक्किम विश्वविद्यालय
SIKKIM UNIVERSITY

6th Mile, Samdur, Tadong -737102
Gangtok, Sikkim, India
Ph. 03592-251212, 251415, 251656
Telefax: 251067
Website: www.cus.ac.in

(भारत के संसद के अधिनियम द्वारा वर्ष 2007 में स्थापित और नैक (एनएएसी) द्वारा वर्ष 2015 में प्रत्यायित केंद्रीय विश्वविद्यालय)
(A central university established by an Act of Parliament of India in 2007 and accredited by NAAC in 2015)


CERTIFICATE

This is to certify that the thesis titled “NANO - CONFINED WATER IN ELECTRIC FIELD: STRUCTURE, RESPONSE AND PROPERTIES” is being submitted by **Ms. Smita Rai (Reg. No. 17/Ph.D/PHY/01)** to the Department of Physics, Sikkim University, for the award of the degree of **Doctor of Philosophy**. This thesis is a record of bonafide research work carried out by her under my guidance and supervision. All sources used in this research have been properly acknowledged and cited.

The results are original and have not been submitted to any other university or institute for the award of any degree or diploma.

It is recommended that this Ph.D. thesis be placed before the examiners for evaluation.

सहायक प्राध्यापक
Assistant Professor
भौतिकी विभाग
Department of Physics
सिक्किम विश्वविद्यालय
Sikkim University


Dr. Dhurba Rai
(Supervisor)
Assistant Professor
Department of Physics
School of Physical Sciences
Sikkim University

Place: Gangtok, Sikkim

Date: 17 May 2024

6 माइल, सामदुर, तादोंग -737102
गंगटोक, सिक्किम, भारत
फोन-03592-251212, 251415, 251656
टेलीफैक्स -251067
वेबसाइट - www.cus.ac.in



6th Mile, Samdur, Tadong -737102
Gangtok, Sikkim, India
Ph. 03592-251212, 251415, 251656
Telefax: 251067
Website: www.cus.ac.in

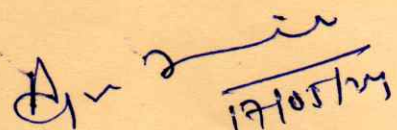
सिक्किम विश्वविद्यालय SIKKIM UNIVERSITY

(भारत के संसद के अधिनियम द्वारा वर्ष 2007 में स्थापित और नैक (एनएएसी) द्वारा वर्ष 2015 में प्रत्यायित केंद्रीय विश्वविद्यालय)
(A central university established by an Act of Parliament of India in 2007 and accredited by NAAC in 2015)

CERTIFICATE

This is to certify that the Ph.D. thesis titled “**NANO - CONFINED WATER IN ELECTRIC FIELD: STRUCTURE, RESPONSE AND PROPERTIES**”, is being submitted by **Ms. Smita Rai (Reg. No. 17/Ph.D/PHY/01)** to the Department of Physics, Sikkim University, for the award of the degree of **Doctor of Philosophy**. This thesis is a record of bonafide research work carried out by her. The results are original and have not been submitted to any other university or institute for the award of any degree or diploma.

It is recommended that this Ph.D. thesis be placed before the examiners for evaluation.


अध्यक्ष
Head
भौतिकी विभाग
Department of Physics
सिक्किम विश्वविद्यालय
Sikkim University
Dr. Ajay Tripathi
(Head of the Department)
Associate Professor

Department of Physics
School of Physical Sciences
Sikkim University

Place: Gangtok, Sikkim

Date: 17/05/24

6 माइल, सामदुर, तादोंग -737102
गंगटोक, सिक्किम, भारत
फोन-03592-251212, 251415, 251656
टेलीफैक्स -251067
वेबसाइट - www.cus.ac.in



सिक्किम विश्वविद्यालय
SIKKIM UNIVERSITY

6th Mile, Samdur, Tadong -737102
Gangtok, Sikkim, India
Ph. 03592-251212, 251415, 251656
Telefax: 251067
Website: www.cus.ac.in

(भारत के संसद के अधिनियम द्वारा वर्ष 2007 में स्थापित और नैक (एनएएसी) द्वारा वर्ष 2015 में प्रत्यायित केंद्रीय विश्वविद्यालय)
(A central university established by an Act of Parliament of India in 2007 and accredited by NAAC in 2015)

Date: 13/05/2024

PLAGIARISM CHECK REPORT

This is to certify that the plagiarism check has been carried out for the following Ph.D. Thesis with the help of **DrillBit Software** and the result is **7%** which is within the permissible limit (below 10% tolerance rate) as per the norms of Sikkim University.

**“NANO - CONFINED WATER IN ELECTRIC FIELD: STRUCTURE,
RESPONSE AND PROPERTIES”**

Submitted by **Ms. Smita Rai** under the supervision of **Dr. Dhurba Rai**, Department of Physics, School of Physical Sciences, Sikkim University, Gangtok, India.

Smita Rai
(Smita Rai)

Signature of Research Scholar

Dhurba Rai
सहायक प्राध्यापक
Assistant Professor
भौतिकी विभाग
Department of Physics
(Dr. Dhurba Rai)
सिक्किम विश्वविद्यालय
Sikkim University

Signature of Supervisor

for
[Signature]

Vetted by Librarian

पुस्तकालयाध्यक्ष
LIBRARIAN
केन्द्रीय पुस्तकालय
सिक्किम विश्वविद्यालय
SIKKIM UNIVERSITY

Dedicated to my parents

Acknowledgements

I am deeply grateful to everyone whose support and belief helped me overcome the challenges of my Ph.D. journey in physics. First and foremost, I extend my heartfelt gratitude to my mentor, Dr. Dhurba Rai, for his guidance, kind support, and encouragement throughout my doctoral pursuit. His wealth of knowledge and expertise has been instrumental in enriching my understanding of my research area. He granted me the freedom to explore new ideas and venture into new territories in my field of study. His immaculate work ethic, setting a standard of diligence and dedication, has certainly inspired me. Yet, amidst his scholarly accomplishments, it is his inherent goodness as a person that leaves the most indelible mark on my journey, and I am forever humbled and grateful to have worked under him.

My deepest gratitude to all the faculty members of the Department of Physics, Sikkim University. Their perspective observations and timely insights into my work have greatly influenced my research culminating in a thesis in present form. Special thanks to my sisters in the department, Laden, Asha, Sweta, Puja and Previsika. Thank you for the cherished bond and beautiful memories we created together in Sikkim. To all my brothers in the department, I extend my sincere thanks for the invaluable companionship in the Ph.D. journey. Outside university, I thank Dr. Vivekanand V. Gobre, Goa University, for his collaboration. The computations carried out at the PARAM-SHAVAK computing facility, at Goa University, which have been indispensable to the advancement my research work, is much appreciated and sincerely acknowledged.

To my family-like friends in Darjeeling, Dirgha, Ishani, Sofia and Pragyan, thank you for your encouragement and understanding throughout my Ph.D. journey. Your unwavering emotional support has been my anchor through the rough seas of life. I am eternally grateful to my parents, for it is their sacrifices and boundless love that paved the way for me to embark on this journey. I thank my father for sparking my interest in science and my mother for instilling in me a resilient spirit, both of which have been the driving forces throughout this journey. I owe a profound debt of gratitude to my sister for shouldering all my responsibilities back home and for never questioning my decisions concerning academic challenges. To my family, I dedicate everything, including this thesis.

Lastly, I acknowledge the University Grants Commission (UGC), New Delhi, India for fellowship through the Department of Physics, Sikkim University, India.

Smita Rai
May 2024

Preface

This thesis deals with nano-confined water in the presence of electric field, their structure, field response and properties. The thesis is organized into five chapters that flow seamlessly into the next as one read. Every chapter opens with an abstract that provides a synopsis of the work presented in that chapter. The background material for each chapter includes references to the classic, reviews and recent studies. Motivation for each work is presented in the section, “Scope of the Work”, followed by systematic investigations presented in the “Results and Discussion” section in Chapters 2 to 4. Each of these chapters ends with the “Summary and Concluding Remarks”, followed by a list of references. At places, comprehensive follow-up studies replete with tables and figures that are not the part of the published articles, are presented. The last chapter provides a succinct overview of the work presented in the thesis along with prospective views and outlooks on a few selected topics.

Chapter 1 provides a brief review of the necessary background materials for the work carried out in this thesis, which begins with an introduction to nano-confined water, their characteristics and significance. With an emphasis on studying field effects, relevant theory and computational background are presented. Several exchange-correlation functionals used in the work are briefly discussed. These functionals are appropriate for describing the characteristic interactions present in the systems under consideration. How molecular systems react to an external electric field is discussed, as well as various features pertinent to examining field influence are presented. There are instances when figures that are extremely relevant to the subject under discussion are extracted from the literature and appropriately acknowledged.

Chapter 2 examines the stability and energetics of in-field structured water nano-chains. The representative structures considered are essentially the network of 3 to 8 units of 4-, 5- or 6-membered ring water clusters that resemble the extended structures with tape or ribbon motifs. Features that could be exploited for device applications are discussed.

Chapter 3 focuses on the electric field response of ~ 1 to 4 nm diameter water nano-rings, which are composed of twisted hydrogen-bonded networks of water molecules. Their potential implications for device applications based on their structural features, flexibility, and related attributes are discussed.

Chapter 4 opens with a systematic investigation of response of a water molecule confined in sub-1nm carbon cages to the external electric fields. Three small fullerenes, viz., C_{28} , C_{30} , C_{32} , are considered for the purpose. The potentials of field-induced structural evolution of CO clathrate hydrates, viz., $CO@5^{12}$, $CO@5^{12}6^2$, $CO@5^{12}6^4$, for promising practical applications are explored.

Chapter 5 briefly summarizes the main conclusions of the research conducted for this thesis. The future directions of research work in this area are discussed. A list of future works on a few selected topics is presented, along with an outline and explanation.

The thesis concludes with an index to facilitate the search for key terms and subjects discussed in the thesis.

List of Publications

(A) Referred Journals:

- Smita Rai, Nayan Sharma, and Dhurba Rai, “Structured water chains in external electric fields”, *Molecular Physics*, e1662957 (2019).
doi.org/10.1080/00268976.2019.1662957
- Smita Rai, Dhurba Rai, and Vivekanand V. Gobre, “Water nano-rings in electric fields”, *Molecular Physics*, e2273977 (2023).
doi.org/10.1080/00268976.2023.2273977

(B) In Preparation:

- Smita Rai and Dhurba Rai, “Electric field influence on CO clathrate hydrates”.
- Smita Rai and Dhurba Rai, “Electric field response of a water molecule confined in carbon nanocages”.

Presentations in National/ International Conferences/Workshops

- **Participated** a workshop on “Introduction to Gaussian: Theory and Practice” in New Delhi, India (8-12 January 2018).
- **Oral Presentation** on the topic “Structured water chains in external electric fields” at the 1st International e-Conference on Recent Advances in Physics and Materials Science-2020 (IC-RAPMS-2020), Kurseong College, West Bengal, India (9-10 July 2020).
- **Poster Presentation** on the topic “Water nano-rings in electric fields” at the National Symposium on Condensed Matter, Materials Science and Statistical Physics, Presidency University, Kolkata (28-29 April 2023).

Contents

Acknowledgements	ii
Preface	iv
Presentations in National/ International Conferences/Workshops	vii
Abbreviations	xi
Symbols	xiii
List of Figures	xiv
List of Tables	xix
1 Introduction: The Background	1
1.1 Preamble	2
1.2 Density Functional Approach	5
1.2.1 The Kohn-Sham DFT	7
1.2.2 XC Energy Functional	9
1.3 Weak Interactions in DFT	10
1.3.1 B97D Functional	11
1.3.2 ω B97X-D Functional	11
1.3.3 M06-2X Functional	12
1.4 Non-Covalent Interactions	12
1.4.1 AIM Analysis	13
1.4.2 RDG Analysis	14
1.5 Electric Field Effects	16
1.5.1 Molecular Response to Electric Field	19
1.5.2 Geometry Optimization in Field	20
1.5.3 Vibrational Stark Effect	22
1.5.4 Water in Electric Field	24
1.6 Water in Confinement	25
1.6.1 Confinement by Hydrophobic Surfaces	26
1.6.2 Confinement in Molecular Cages	27
1.6.3 Nanoscale Water Bridge	29
1.7 Photolysis of water	30
1.8 Thesis Outline	31
References	33

2	Water Nano-Chains in Electric Fields	43
2.1	Background	44
2.2	Scope of the Work	46
2.3	Computational Methodology	48
2.4	Computed Results and Discussion	49
2.4.1	Single-file Water Chain	50
2.4.2	Tetramer Structured Water Chain	51
2.4.3	Pentamer Structured Water Chain	52
2.4.4	Hexamer Structured Water Chain	54
2.4.5	Average Hydrogen Bond Length and Dipole Moment	55
2.4.6	Energetics, HL Gaps and Stability	59
2.5	Summary and Concluding Remarks	63
	References	65
3	Water Nano-Rings in Electric Fields	75
3.1	Background	76
3.2	Scope of the Work	78
3.3	Methodology and Computational Details	80
3.4	Computed Results and Discussion	82
3.4.1	Structure, Stability and Dipole Moment	82
3.4.2	Noncovalent Interaction (NCI) Analysis	88
3.4.3	Frontier MOs and HL Gap	90
3.4.4	Infrared Spectra	92
3.4.5	Bending mode	94
3.4.6	Stretching mode	95
3.4.7	Raman Spectra	98
3.5	Technological Implications	99
3.6	Summary and Concluding Remarks	101
	References	103
4	Electric Field Response of a Molecule Nanoconfined in Molecular Cages	112
4.1	Background	113
4.2	Scope of the Work	118
4.3	Methodology and Computational Details	120
4.4	Computed Results and Discussion	122
4.4.1	H ₂ O@(C ₂₈ , C ₃₀ , C ₃₂) cages	122
4.4.2	Dipole Screening	124
4.4.3	Dipole Moment and HL Gap	125
4.4.4	Vibrational Response to Applied Field	126
4.4.5	Local Field and Penetration Factor	129
4.4.6	CO@(5 ¹² , 5 ¹² 6 ² , 5 ¹² 6 ⁴) cages	132
4.4.7	Energetics and Reactivity Indices	134

Contents

4.4.8	NCI Analysis	136
4.4.9	Electric Field Response of Confined CO	137
4.4.10	Field-Induced Structural Evolution	139
4.5	Summary and Concluding Remarks	141
	References	143
5	Future Prospects	151
	References	156
	Index	157

Abbreviations

a.u.	a tomic u nits
AIM	A toms I n M olecules
BSSE	B asis S et S uperposition E rror
CNT	C arbon N ano T ube
DFT	D ensity F unctional T heory
DA	D onor- A cceptor
DDAA	D onor- D onor A cceptor- A cceptor
GGA	G eneralized G radient A pproximation
GAUSSIAN	G aussian 16 P ackage
HOMO	H ighest O ccupied M olecular O rbital
H-bond	H ydrogen-bond
HF	H artree- F ock
HK	H ohenberg- K ohn
HL	H OMO- L UMO
LUMO	L owest U noccupied M olecular O rbital
LDA	L ocal D ensity A pproximation
MESP	M olecular E lectrostatic P otential
MD	M olecular D ynamics
MOF	M etal- O rganic F ramework
NCI	N on- C ovalent I nteraction
PES	P otential E nergy S urface
PV	P hotovoltaic
RDG	R educed D ensity G radient
STR	S tark T uning R ate
STM	S canning T unneling M icroscopy
TF	T homas- F ermi

Abbreviations

TMD	T ransition- M etal D ichalcogenide
vdW	v an d er W aals
VSE	V ibrational S tark E ffect
XC	E Xchange- C orrelation

Symbols

Symbol	Quantity	Unit	Value
\vec{F}	Electric Field	a.u.	51.42 Volt/Å
\vec{d}	Electric Dipole Moment	Debye	3.34×10^{-30} Coulomb-meter
ρ	Electron Density	a.u.	1.0812×10^{12} Coulomb/meter ³
α	Polarizability	a.u.	0.1481 Å ³
E	Energy	Hartree	27.2113 eV

List of Figures

1.1	Kohn-Sham ansatz: The exact ground state density $\rho_0(\vec{r})$ of a real physical system is equal to Kohn-Sham density $\rho_{KS}(\vec{r})$ of a noninteracting fictitious system calculated from the KS orbitals $\{\phi_i^{KS}\}$.	8
1.2	Representative RDG scatter plot (left) and NCIs mapping (right) for 3-bromo-2-hydroxypyridine dimer showing all three interactions. Figure adapted from Ref. [70].	15
1.3	An illustrative potential energy surface of a water tetramer depending on the generalized coordinates $(\vec{q}_1, \vec{q}_2, \dots, \vec{q}_N)$ with maxima, minima and saddle points. The generalized coordinates include the applied electric field, \vec{F} .	21
1.4	Conductance measurement in a $\text{H}_2\text{O}@\text{C}_{60}$ junction setup revealing spin isomer state of a water molecule confined in C_{60} fullerene. Figure adapted from Ref. [138].	27
1.5	Field-induced nanoscale water pillar in MD simulations resembling water bridge observed in AFM experiments with snapshots at (a) $t = 0$, (b) $t = 35$ ps, (c) $t = 75$ ps, for field 2.0 V nm^{-1} , and (d) height evolution for field increased in step of 0.25 V nm^{-1} starting at 1.0 V nm^{-1} . Figure adapted from Ref. [149].	29
2.1	Representative single-file (a) helical and (b) zigzag water chain consisting of 10 water molecules each, optimized at the B3LYP/6-311++G(d,p) level of theory.	50
2.2	Water tetramer chain consisting of 3-8 units of corner-sharing water tetramer rings in the presence of an electric field in the range of $0.0005\text{-}0.020 \text{ a.u.}$. The arrow indicates the direction of field \vec{F} applied along the length of the chains. The length of the chains (extreme O-O distance) for a minimum applied field is in the range of $1.28\text{-}3.32 \text{ nm}$.	51

List of Figures

2.3	Water pentamer chain consisting of 3-8 units of edge-sharing water pentamer rings in the presence of a field in the range 0.0005-0.022 a.u. The arrow depicts the direction along which the field is applied. The length of the chains (extreme O-O distance) for a minimum applied field is in the range of 1.21-2.86 nm.	53
2.4	Water hexamer chains consisting of 3-8 units of the corner-sharing water hexamer rings in the presence of a field in the range 0.0002-0.014 a.u. applied along the length of the chains. The length of the chains (extreme O-O distance) for a minimum applied field is in the range of 1.87-4.63 nm.	55
2.5	Field variation of dipole moment for (a) tetramer, (b) pentamer, and (c) hexamer structured water chain. The numerals 3–8 represent the number of constituent units in each chain.	57
2.6	Variation of average dipole moment per water monomer as a function of structures' size at a field strength of 0.005 a.u. for tetramer, pentamer and hexamer chains.	58
2.7	Binding energy per molecule (E_B) as a function of field for pentamer chains. E_B as a function of structures' size for field values, (a) 0.002, (b) 0.004 and (c) 0.006 a.u. are shown in the inset figure.	59
2.8	Variation of HL energy gap (E_g) as a function of electric field in the (a) tetramer, (b) pentamer, and (c) hexamer chains.	61
2.9	Threshold field (F_{th}) as a function of structures' size for the (a) tetramer, (b) pentamer and (c) hexamer chains.	61
2.10	Evolution of the HOMO and LUMO energies in the 5-units of pentamer chain for field applied in the range (0.010–0.100 a.u.). Shown are the HOMO and LUMO for field strengths, (a) 0.010, (b) 0.030, (c) 0.052, (d) 0.070, and (e) 0.100 a.u. Molecular orbitals are drawn at the contour value ± 0.02 . The arrow indicates the direction of the applied field.	62

List of Figures

3.1	Nanoscopic H-bonded ring formed by 72 water molecules organized in a twisted ribbon-like network. The arrows indicate the directions along which an electric field (\vec{F}) is applied, i.e., parallel and perpendicular to the ring.	79
3.2	(a) A structural unit consisting of 2- and 4-coordinated water molecules, labeled as DA and DDAA respectively, which on successive repetition by sharing water molecules generate the nano-sized ring water structures. (b) MESP topology in a.u. mapped on electron number density iso-surface value set at ± 0.004 a.u.	83
3.3	(a) T4(1)-6R, (b) T4(1)-12R and (c) T4(1)-18R nano-sized rings consisting of 36, 72 and 108 water molecules with an average diameter ($O \cdots O$ distance between the diametrically opposite DDAA molecules) of 1.54, 3.10, and 4.56 nm and possessing a permanent dipole moment ($ \vec{p} $) of 13.4, 0 and 15.2 Debye (D), respectively, oriented perpendicular to the ring geometry.	83
3.4	Variation of (a) dipole moment and (b) average H-bond length with the field applied perpendicular to the plane of the ring structures. The field free dipole moment for T4(1)-6R, T4(1)-12R and T4(1)-18R are 13.4, 0 and 15.2 Debye, respectively.	86
3.5	RGB (red-green-blue) colour scatter plots illustrating the variation of RDG against $\text{sign}(\lambda_2)\rho(r)$ in (a) structural unit, (b) T4(1)-6R, (c) T4(1)-12R and (d) T4(1)-18R nano-rings, and the isosurfaces depicting NCI regions in the respective nano-rings at RDG value of 0.5 computed at the B3LYP/6-31+G(d,p) level of theory.	89
3.6	(a) Frontier molecular orbital (MO) energies in T4(1)-6R as a function of the electric field in the range of 0 to 0.019 a.u. applied perpendicular to the ring plane. The HOMO and LUMO for field values, (a) 0, (b) 0.0050, (c) 0.0100, and (d) 0.0150 a.u. shown are drawn at the contour value ± 0.02 . The inset depicts the field variation of frontier MO energies for T4(1)-18R. (b) Evolution of the HL gap for the T4(1)-6R, T4(1)-12R and T4(1)-18R rings with field.	90

List of Figures

3.7	(a) Full IR spectra of the three nano-rings for field-free case, along with the experimental profile for bulk liquid water (dotted spectral profile) redrawn from [94]. (b) Evolution of the IR spectra of the T4(1)-6R nano-ring under the influence of field in the range 0-0.018 a.u.	93
3.8	Field-induced variation of H-O-H bending modes in the T4(1)-6R nano-ring, while the detailed description is presented in the text. . .	94
3.9	Field-induced evolution of O-H stretching modes in the T4(1)-6R nano-ring. Detailed descriptions of the vibrational modes and the associated peaks are presented in the text.	96
3.10	Field evolution of O-H stretching modes in the (a) T4(1)-12R and (b) T4(1)-18R nano-ring structures, wherein the labelling for vibrational modes is identical to that in Fig. 3.9.	97
3.11	Field-induced variation of Raman signals in the O-H stretching region for the T4(1)-6R nano-ring. The labelling for vibrational modes is identical to that in Fig. 3.9.	98
4.1	Five building block cages (5^{12} , $5^{12}6^2$, $5^{12}6^4$, $5^{12}6^8$, and $4^35^66^3$) that make up the three common clathrate structures, sI, sII and sH [46].	117
4.2	Optimized structures of $H_2O@C_{28}$, C_{30} , C_{32} , C_{60}) on which electric field \vec{F} is applied along their dipole moment.	123
4.3	(a) Dipole moment and (b) HL gap of the $H_2O@C_{28}$, C_{30} , C_{32}) cages as a function of the applied electric field in the range (0-0.02 a.u.).	125
4.4	Comparative field evolution of O-H symmetric stretch (SS) and asymmetric stretch (AS) vibrational peaks of the H_2O molecule in (a) C_{28} , (b) C_{30} , and (c) C_{32} cages. The inset figure depicts the evolution of the bending mode.	127

List of Figures

4.5	Onsager's reaction field model consisting of a spherical cavity of radius ' a ' in a dielectric continuum of relative permittivity ϵ_r subjected to external field \vec{F} , corresponding to which local field at dipole's position is \vec{F}_{local}	129
4.6	Local field $ \vec{F}_{local} $ as a function of external field $ \vec{F} $	131
4.7	Energy minimum structure of (a) 5^{12} , (b) $5^{12}6^2$, and (c) $5^{12}6^4$ H-bonded building block cages of the cubic sI and sII lattice structures of the clathrate hydrates.	133
4.8	Energy minimum structure of (a) $\text{CO}@5^{12}$, (b) $\text{CO}@5^{12}6^2$, and (c) $\text{CO}@5^{12}6^4$ H-bonded building block cages of the CO clathrate hydrates.	134
4.9	RDG scatter plot (a)-(c) for $\text{CO}@5^{12}$, $\text{CO}@5^{12}6^2$, $\text{CO}@5^{12}6^4$, respectively, and the corresponding RDG isosurface (d)-(f) illustrating NCI regions drawn at the RDG value of 0.5.	137
4.10	CO bond length (\AA) and CO stretching frequency peak position (cm^{-1}) as a function of applied field in (a) $\text{CO}@5^{12}$, (b) $\text{CO}@5^{12}6^2$, and (c) $\text{CO}@5^{12}6^4$ cages.	138
4.11	Field evolution of IR spectra of (a) $\text{CO}@5^{12}$, (b) $\text{CO}@5^{12}6^2$, and (c) $\text{CO}@5^{12}6^4$ cages, showing three characteristic vibrational modes; liberation ($\lesssim 1000 \text{ cm}^{-1}$), H-O-H bending ($\sim 1740 \text{ cm}^{-1}$) and O-H stretching ($> 3000 \text{ cm}^{-1}$).	138
4.12	(a) Dipole moment and (b) average H-bond length in $\text{CO}@5^{12}$, $5^{12}6^2$, $5^{12}6^4$ cages.	139
4.13	Field-induced structural evolution of (a) $\text{CO}@5^{12}$, (b) $\text{CO}@5^{12}6^2$, and (c) $\text{CO}@5^{12}6^4$ structures. The applied field \vec{F} is indicated by an arrow, whose length proportionally represents its magnitude.. . .	140

List of Tables

3.1	Zero-point energy (ZPE) corrected stabilisation energy of the T4(1)-6R, T4(1)-12R and T4(1)-18R nano-rings evaluated at the B3LYP/6-31+G(d,p) level of theory.	84
4.1	Geometrical parameters calculated at the M06-2X/6-311++G(d,p) level of theory.	123
4.2	Dipole moment (Debye) in absence of field calculated using different functionals with the 6-311++G(d,p) basis set.	124
4.3	HL gap (eV) in absence of field calculated using different functionals with the 6-311++G(d,p) basis set.	126
4.4	Calculated zero-field parameters for a water molecule and small-sized fullerenes relevant for the estimation of local field and penetration factor.	131
4.5	Geometrical parameters (\AA) calculated at the ω B97X-D/6-311++G(d,p) level.	133
4.6	Interaction energies (kcal/mol) (BSSE uncorrected) in empty and guest-host complexes. The values in parentheses are the deformation energies.	135
4.7	Reactivity indices (eV), chemical hardness (η), electronegativity (χ) and electrophilicity (ω), for empty and CO encapsulated cages evaluated at the ω B97X-D/6-311++G(d,p) level of theory. The values in the parentheses are reported to be calculated at the MP2/6-31+G(d) level [99].	135

Chapter1

Introduction: The Background

Abstract

An overview of the most relevant and trending topics concerning the work undertaken in this thesis is provided in this chapter. Theoretical background, essential computational techniques and tools and the relevant literature are presented along with the strategy of the work undertaken, while the details are covered in the respective chapters.

1.1 Preamble

The study of the structure and properties of clusters composed of a variety of atoms or molecules bridges different disciplines of physics and chemistry [1], as well as many sub-disciplines of nanoscience and nanotechnology [2–4]. In particular, the study of molecular clusters is a promising research field that provides insights into the underlying bulk properties from the finite-cluster calculations [5–8]. Additionally, the molecular clusters are rich in a diverse range of exciting physical properties that can be suitably tuned through the application of external electric or magnetic fields. Precise control over the structure and properties of molecular clusters is key in the development of next-generation functional materials for nanoscale device applications. Moreover, designing nanoscale building blocks from the bottom-up assembly of molecule clusters, which can be programmed, manipulated, and self-assembled into well-defined new functional bulk materials, is an appealing method for creating new kinds of materials for a variety of applications [9].

Another exciting and rapidly evolving field with enormous technological implications is molecular confinement and manipulation [10]. Through confinement, the molecules can be effectively isolated from the outside world, thereby revealing their intrinsic characteristics that would otherwise be hidden in bulk conditions. Also, the properties of the molecules can be altered by molecular confinement effects, which makes molecular confinement a powerful setup to explore hitherto undiscovered features of the molecules [11, 12]. The discovery of new physical and chemical properties as well as novel phenomena demonstrate the immense potential of the confinement effect [13]. By modeling confinement effects, some characteristics of the molecular systems become accessible that would otherwise be exceedingly challenging to explore experimentally [14].

With a rapidly evolving field of water-based devices and electronics [15–20], we have taken into consideration water in our study as it is ubiquitous and

because its unique properties make it special for technological applications [21]. While bulk water has complex hydrogen-bonding (H-bonding) networks, water at the molecular and nanoscale levels exhibits distinct structures. Moreover, the behavior of water at a given length scale is mostly attributed to the intermolecular interactions associated with H-bonding at that scale. Additionally, in extreme or constrained conditions, such as in spatial confinement in nano cavities, pores or channels, the arrangement of water molecules deviates significantly from condensed phases, resulting in properties markedly different from bulk water and ice [22, 23]. Moreover, the water clusters in metal-organic frameworks (MOFs) that are nano-confined have topologies resembling linear chains, rings, or helices and the framework prevents the molecules from grouping together to form arbitrary configurations [24–26]. Both the theory and experimental studies have revealed numerous unusual properties of nanoconfined water, such as abnormally low dielectric constant [27–29] and high proton conductivity [30–34]. Given the significant differences in the properties of nanoconfined and bulk water, it is worthwhile to investigate how such nanoconfined water responds to an external electric field, thereby revealing features that could be exploited in technological applications, such as energy-dissipation devices [35]. In particular, understanding how a nanoconfined water molecule, with a sub-1nm confinement dimension approaching the molecular size responds to external field could add novel features to the single-molecule junction devices, such as $\text{H}_2\text{O}@\text{C}_{60}$ junction [36–38], resulting in enhanced functionalities for various applications in molecular electronics. In this thesis, an attempt has been made to study some aspects of a water molecule contained in small carbon nanocages under an electric field.

Furthermore, it is also possible that the electric field, rather than nanoconfinement provide the necessary coordination for water molecules in the nano-size clusters to form distinct H-bonding networks that resemble structured chains and rings. Such structures may provide not only novel features relevant for device applications but also serve as test-beds to probe the fundamental properties of water in nanoconfinement. The study of energetics, electronic properties, and

the manipulation of the characteristic properties of such structured water nano-chains and rings by an external electric field could open up potential applications in nanotechnology. Moreover, given that the water molecules in the structured chains and rings are prearranged in a distinct network by cooperative water-water H-bonding, how do they adapt to the applied field? Specifically, how might one explore the manifestation of these structured water geometries that are so prominent in the theoretical computations? Do the structured water chains or rings possess any features that facilitate the proton transport mechanism? These are the subjects explored and discussed in the thesis.

Water also adopts crystalline solid cage structures at high pressure and low temperature called clathrate hydrate, which are different from hexagonal ice in that they contain small gas molecules trapped inside the cages [39, 40]. The frozen polyhedral water cages are stabilized by H-bonding interaction between the water molecules that hold the cages together and the van der Waals (vdW) interaction between the enclosed gas and the water molecules, resulting in a crystalline structure that is more stable than hexagonal ice. Clathrate hydrates provide valuable insights into guest-water interactions and have been extensively investigated for a range of industrial applications, including gas capture, storage, and release [41, 42]. Generally, the basic parameters such as temperature and pressure are suitably tuned to provide the clathrate hydrates with the desired properties for any useful applications. While an electric field may potentially modulate the properties of clathrate hydrates for relevant technological applications, the molecular-level study of field effects is crucial in the description of the bulk characteristics as well as in understanding the underlying mechanisms of confinement, storage, and stability. This is among the subjects covered in the thesis.

In what follows, we provide a quick overview of the relevant theory, computational techniques and current issues that essentially serve the background of the research work presented in this thesis.

1.2 Density Functional Approach

Different from the wave function-based theories like the Hartree-Fock (HF) theory and the post-Hartree-Fock methods (e.g., configuration interaction, perturbation theory, and coupled-cluster theory), the density functional theory (DFT) is formulated in terms of the electronic density alone as a fundamental quantity in describing many-electron systems [43, 44]. The DFT is now widely recognized as the most efficient, powerful, and economical method for electronic structure computations and determining material properties at the molecular, nano and bulk scales [45–48].

The significance of the density-based approach was recognized in the early days of quantum physics in 1927, even before the development of the HF theory, when Thomas and Fermi independently proposed a density-based technique to describe many-electron atomic systems [49, 50]. The primary idea in the Thomas-Fermi (TF) theory was to express the kinetic energy of electrons in an atom as a functional of the one-particle electron density, appropriate for a uniform non-interacting electron gas that would be employed locally at a given point, which is commonly referred to as the local density approximation. Thus, within the TF theory, adding the electrostatic energies of electron-nuclear attraction and classical electron-electron repulsion would result in the total energy as an explicit functional of electron density $\rho(\vec{r})$ [43]. The density is then varied to minimize the energy functional $E[\rho(\vec{r})]$ subject to the constraint, $\int \rho(\vec{r})d^3r = N$, that expresses the conservation of the total number of electrons in the atom. This facilitates the determination of ground state density and energy of the atom within the premise of the variational principle.

Evidently, the advantage of the wave function-based approach is clear and appealing since the N electron wave function $\psi(\vec{r}_1, \dots, \vec{r}_N)$ is a complex function that depends on $3N$ spatial coordinates, while the density $\rho(\vec{r})$ is a real function

that depends only on 3 spatial coordinates (x, y and z), which makes it computationally feasible even for large systems such as molecular clusters and solids. However, despite offering a satisfactory qualitative determination for the total atomic energies, the quantitative predictions are dreadfully inaccurate. Moreover, the fact that the TF theory does not lead to atoms bonding, which makes it impossible to describe molecules and solids, is arguably the most fundamental limitation of the TF theory [43]. Subsequent development by adding non-classical energy ingredients such as exchange energy, and accounting for density variation through gradient correction, however, does not lead to the formation of stable negative ions or molecules, nor does it result in the electronic shell structure of atoms. Nevertheless, the TF theory served as a precursor to the modern DFT formulated more than three decades after it was first proposed.

The theoretical foundation of the modern DFT is a set of theorems due to Hohenberg and Kohn formulated in 1964 [51]. For a nondegenerate many-electron system in the ground state, the first Hohenberg-Kohn (HK) theorem establishes one-to-one correspondence between the external potential $v_{ext}(\vec{r})$ resulting from the background nuclei and the electron density $\rho(\vec{r})$ that move in the external potential, which is expressed symbolically as $v_{ext}(\vec{r}) \Longleftrightarrow \rho(\vec{r})$, thereby the potential uniquely determines the density (up to an additive constant) and vice versa. The second HK theorem ensures the existence of an energy functional that reaches its minimum for the exact density, and thus, establishes a variational principle with the density as a variable, i.e., $E_0 = E[\rho_0] \leq E[\tilde{\rho}]$, where E_0 is the ground state energy and ρ_0 is the exact ground state density, while $\tilde{\rho}$ is the “trial” density. Although, the energy function $E[\rho]$ is expressible as

$$E[\rho] = F_{HK}[\rho] + \int \rho(\vec{r})v_{ext}(\vec{r})d^3r, \quad (1.1)$$

where the HK functional is the sum of the kinetic and electron-electron interaction energy functionals, i.e., $F_{HK}[\rho] = T[\rho] + V_{ee}[\rho]$, the HK theorems tell us nothing about how to construct this functional. As a result, the HK formulation of DFT

lacks the practical implementation. However, a workable version was developed by Kohn and Sham the following year, which introduced DFT into mainstream electronic structure calculations for a wide range of systems.

1.2.1 The Kohn-Sham DFT

With its proposal in 1965 [52], the Kohn-Sham (KS) DFT has grown in prominence as the most versatile theory for many-electron systems, primarily due to its cost-effective performance in large-scale systems. Its distinct ability to incorporate essentially all interactions within the mean-field description is a clear advantage, with the HF-like equations known as the KS equations, which must be solved numerically and iteratively until self-consistency in the calculations is reached. The most novel aspect of the KS formalism is that it treats a real interacting electron system by establishing a correspondence between the real physical system and a fictitious non-interacting KS system that has exactly the same ground state density as the real system, i.e., $\rho_0(\vec{r}) = \rho_{KS}(\vec{r}) = \sum_{i=1}^N |\phi_i^{KS}(\vec{r})|^2$ (spin sum implied). An illustration representing the correspondence is shown in Fig. 1.1. The KS orbitals $\{\phi_i^{KS}\}$ are the solutions of the HF-like KS equations,

$$\left[-\frac{1}{2}\nabla^2 + v_{KS}(\vec{r}) \right] \phi_i^{KS} = \epsilon_i \phi_i^{KS} \quad (i = 1, 2, \dots, N). \quad (1.2)$$

The electrons in the KS system are subjected to a local one-particle effective mean potential $v_{KS}(\vec{r})$. The advantage of fictitious non-interacting KS system is that the kinetic energy $T_s[\rho]$ of the non-interacting electrons can be explicitly constructed from the KS orbitals $\{\phi_i^{KS}\}$, while the difference $T[\rho] - T_s[\rho]$ is relegated to the exchange-correlation term, such that the HK functional can now be expressed as

$$F_{HK}[\rho] = T_s[\rho] + J[\rho] + E_{XC}[\rho], \quad (1.3)$$

where $E_{XC}[\rho] = (T[\rho] - T_s[\rho]) + (V_{ee}[\rho] - J[\rho])$ is the KS exchange-correlation (XC) energy functional, which is constructed out of the non-classical components

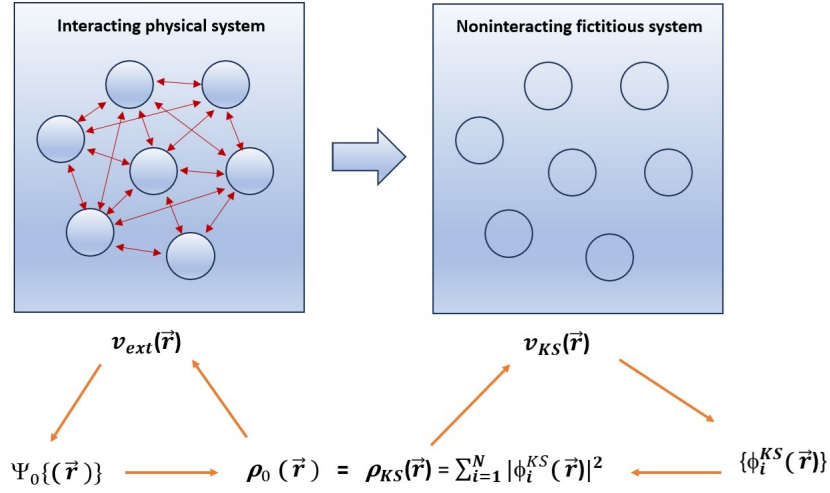


FIGURE 1.1: Kohn-Sham ansatz: The exact ground state density $\rho_0(\vec{r})$ of a real physical system is equal to Kohn-Sham density $\rho_{KS}(\vec{r})$ of a noninteracting fictitious system calculated from the KS orbitals $\{\phi_i^{KS}\}$.

of the kinetic and electron-electron interaction energies. The effective one-particle potential in the KS equations is evaluated from the electron density as

$$\begin{aligned}
 v_{KS}(\vec{r}) &= v_{ext}(\vec{r}) + \frac{\delta J[\rho]}{\delta \rho(\vec{r})} + \frac{\delta E_{XC}[\rho]}{\delta \rho(\vec{r})}, \\
 &= v_{ext}(\vec{r}) + \int \frac{\rho(\vec{r}')}{|\vec{r} - \vec{r}'|} d^3 r' + V_{XC}[\rho],
 \end{aligned} \tag{1.4}$$

where $V_{XC}[\rho] = \delta E_{XC}[\rho] / \delta \rho(\vec{r})$ is the exchange-correlation potential. Equations (1.2) and (1.4) are to be solved self-consistently for the KS orbitals $\{\phi_i^{KS}\}$ to yield the desired density, $\rho_0(\vec{r}) = \rho_{KS}(\vec{r}) = \sum_{i=1}^N |\phi_i^{KS}(\vec{r})|^2$. It is important to note that neither the exact KS orbitals ϕ_i^{KS} , nor the orbital energies ϵ_i have any known direct physical significance, other than constructing the physical ground state density and relating the highest ϵ_i associated with the occupied state to the ionization energy. Furthermore, solving the KS equations requires an explicit supply of the XC energy functional, while the DFT itself does not offer any prescription for its construction.

1.2.2 XC Energy Functional

The central idea in the KS-DFT is to construct the XC energy functional, which in principle has all the non-classical many-electron effects hidden in it. Unfortunately, this needs to be approximated because its exact form is unknown and there isn't a unique and systematic strategy for its determination. Consequently, numerous efforts to create suitable XC energy functionals have resulted in the development of hundreds of XC energy functionals [48].

Starting with the local density approximation (LDA) that substitutes the XC energy at each point with that of a homogeneous electron gas, a variety of versatile XC energy functionals have been developed. Particularly, in our work, three-semiempirical parameters-based hybrid XC functional obtained by combining Becke's exchange functional with the Lee-Yang-Parr correlation functional (abbreviated as B3LYP) is extensively employed, and thus merits a special note in relation to its ingredient components. The B3LYP functional is similar to the three parameters hybrid functional $E_{XC}^{B3PW91}[\rho]$ proposed by Becke in 1993 [53], and is constructed out of the constituent energy ingredients as follows [54]

$$\begin{aligned} E_{XC}^{B3LYP}[\rho] = & (E_X^{LDA}[\rho] + E_C^{VWN3}[\rho]) + a_0 (E_X^{Exact}[\rho] - E_X^{LDA}[\rho]) \\ & + a_X \Delta E_X^{B88}[\rho] + a_C (E_C^{LYP}[\rho] - E_C^{VWN3}[\rho]). \end{aligned} \quad (1.5)$$

Clearly, this is an admixture of the HF exchange and the DFT exchange-correlation with explicit ingredients, viz., (i) LDA exchange energy $E_X^{LDA}[\rho] \simeq \int \rho(\vec{r})^{4/3} d^3r$, (ii) Vosko-Wilk-Nusair (VWN functional III) LDA correlation energy $E_C^{VWN3}[\rho]$ [55], (iii) the exact HF exchange energy $E_X^{Exact}[\rho]$, (iv) Becke's 1988 gradient-corrected exchange energy functional $\Delta E_X^{B88}[\rho]$ [56], and (v) the correlation functional due to Lee, Yang and Parr, $E_C^{LYP}[\rho]$ [57], while a_0, a_X, a_C are the three semiempirically determined fitting parameters. It must be mentioned that the empirical functionals like B3LYP provide superior accuracy for systems they are parametrized for, but perform poorly in other systems. Amid such uncertainties

stemming from empirical fittings, Perdew, Burke and Ernzerhof (PBE) in 1996 introduced a non-empirical and general applicable functional, the so-called PBE functional that provides reasonable accuracy for a wide range of systems [58].

Although the DFT calculations are not truly *ab initio* first-principle computations due to inherent semiempirical fitting parameters, the benefits of DFT theory far outweigh any known drawbacks. In particular, the immense popularity of the DFT is due to the exceptional performance of the B3LYP functional in a wide range of molecular systems dominated by covalent bonding and/or non-covalent H-bonding interactions [59, 60]. Unfortunately, the B3LYP and the other similar hybrid XC functionals provide a poor description of weak interactions, such as the vdW dispersion interactions [61], with the exception that PBE and PBE0 (the hybrid variant of PBE) functionals sometimes outweigh the performance of their vdW inclusive counterparts [62]. We now briefly review the description of weak interactions in the DFT formalism and the functionals developed to handle them.

1.3 Weak Interactions in DFT

The importance of weak interactions, like vdW interactions, cannot be undermined given the roles they play, such as in structure formation, energetic stability and understanding various physical processes in the diverse fields of chemistry, biology, molecular physics, and material science. Weak interactions can arise from a variety of physical processes, including fluctuations in electron density, dipole-induced fluctuations, long-range dispersion interactions between atoms or molecules, etc. However, their inadequate description constitutes a serious obstacle to the otherwise universal adoption of the KS-DFT methodology. For instance, the generalized gradient approximation (GGA) and the hybrid GGA functionals (e.g., B3LYP, PBE) do not capture induced dipoles and the resulting dispersion interactions, and also the long-range correlation occurring between fluctuations in

electron density, thereby preventing modeling of the vast majority of molecular complexes, molecular packing and adsorption processes. Several routes have been explored to take into account the weak interactions within the DFT formalism. In the remainder of this section, we review special functionals developed to handle the weak interactions, and that are used in our work.

1.3.1 B97D Functional

Since the common GGA functionals, including hybrids, cannot describe the long-range electron correlations that are responsible for vdW interaction, Grimme in 2006 [63] proposed a GGA type functional based on Becke’s 1997 (B97) functional such that the short electron correlation in the conventional GGA is left unaltered, while the medium to long-range correlation effects are considered empirically. The total energy is then the sum of KS-DFT energy and dispersion correction, i.e.,

$$E_{DFT-D}[\rho] = E_{KS-DFT}[\rho] + E_{disp}, \quad (1.6)$$

where the dispersion energy component E_{disp} is the empirical, medium to long-range, atom-pairwise (R_{ij}) dispersion correction of the form $C_6 \cdot R^{-6}$, modulated by a damping function $f_{dmp}(R_{ij})$.

1.3.2 ω B97X-D Functional

The weak interactions resulting from the interaction between the induced fluctuating dipoles are long-range and have a significant influence on many material properties. However, the conventionally developed DFT functionals are unable to account for long-range correlations. In particular, the non-Coulomb part of the exchange functionals typically dies off very rapidly, making them highly erroneous at large distances. As a result, the conventional functionals are unsuitable for modeling processes like electron excitations to high orbitals. Chai and Head-Gordon in

2008 [64] proposed a long-range corrected dispersion interaction functional called ω B97X-D, where ω denotes a parameter controlling the partitioning of the inter-electronic distance r . The range of interaction is defined employing the partition of unity method with error function $\text{erf}(\omega r)/r$ for long-range (treated by 100% HF exchange), while complementary error function $\text{erfc}(\omega r)/r$ for short-range (treated by exchange functional). Calculations reveal that this new functional shows noticeably better improvement over other empirical dispersion-corrected functionals when applied to the non-bonded interactions, while providing similar results for the bonded interactions.

1.3.3 M06-2X Functional

This is a hybrid meta exchange-correlation functional (Minnesota functional) with 54% HF exchange developed at the University of Minnesota by Zhao and Truhlar in 2006 [65]. It uses double the amount of nonlocal exchange (2X) and 32 empirically optimized parameters for nonmetal atoms. It is an improvement over its predecessor M05-2X and is reported to perform the best among the M06-class functionals for kinetics and non-covalent interactions, offering significant improvements over the conventional density functionals. Remarkably, this functional accounts for the medium-range electron correlation implicitly, which is adequate to capture dispersion interactions in a wide variety of complexes, however, it does not capture the long-range dispersion interaction present in the H-bonded systems. Therefore, we do not use this functional in the H-bonded systems we studied in our work for other than comparison purposes.

1.4 Non-Covalent Interactions

Non-covalent interactions (NCIs) are ubiquitous in nature and contribute to the cohesion of chemical species leading to structural stabilization forming molecular

crystals, supra-molecular complexes, nanomaterials etc. In contrast to strong covalent interactions that result from the sharing of electrons between the atoms, non-covalent interactions are far weaker and have significantly lower energy and directionality. Nevertheless, they constitute a robust mechanism that allows molecules to assemble into stable structures. NCIs include hydrogen and halogen bonds, weak H-bonds ($\text{C-H}\cdots\text{O}$ and $\text{O-H}\cdots\pi$) and $\pi\cdots\pi$ interactions as well as weak interactions like vdW dispersion interaction.

Since the electron density $\rho(\vec{r})$ naturally contains a wealth of information about the interaction between the atoms or molecules, and can be obtained from *ab initio* calculations or X-ray diffraction experiments, studying the topology of the electron density is an important investigative tool for probing and understanding the weak and non-covalent interactions. Here, we provide a brief overview of the two popular methodological techniques for analyzing NCIs in a variety of systems.

1.4.1 AIM Analysis

The theory of Atoms in Molecules (AIM) [66] pioneered by R. W. F. Bader in the 1990s is now a well-established tool for the description of various bonding interactions, including the conventional and non-conventional H-bondings, such as $\text{C-H}\cdots\text{O}$ and $\text{O-H}\cdots\pi$ interactions. The key elements in AIM are electron density $\rho(\vec{r})$, its gradient $\nabla\rho(\vec{r})$ and Laplacian $\nabla^2\rho(\vec{r})$. They determine the topographical features of the electron density that facilitate the definition of a chemical bond on the basis of the existence of a bond critical point (bcp), linking the nuclei of neighboring atoms through a special path called bond path and the characterization of the bond on the basis of the magnitude of $\rho(\vec{r})$ and the sign of $\nabla^2\rho(\vec{r})$. A critical point \vec{r}_c , at which $\nabla\rho(\vec{r})$ vanish, is characterized by a pair indices (ω, σ) , where ω is the number of non-zero eigenvalues associated with the principal curvatures of $\rho(\vec{r})$, i.e., Hessian of electron density, $(H_{ij})_{3\times 3} = \partial^2\rho(\vec{r})/\partial x_i\partial x_j$ ($i, j = x, y, z$) and σ is the sum of the signs of the eigenvalues $(\lambda_1, \lambda_2, \lambda_3)$ of the Hessian matrix at

the critical points. The two atoms are said to be bonded for if they are linked by a bcp characterized by (3,-1) criticality.

It is established that for the covalent bonding interactions, $\nabla^2\rho(\vec{r}_c) < 0$, and its magnitude and $\rho(\vec{r}_c)$ both have appreciable values. In contrast, for NCIs, $\nabla^2\rho(\vec{r}_c) > 0$ and $\rho(\vec{r}_c)$ is relatively low, while (3,-1) bond criticality is common to both interactions. The AIM-based criteria for the existence of H-bonds (including weak H-bonds) have been proposed to be (0.002 to 0.035 a.u.) for $\rho(\vec{r}_c)$ while (+0.024 to +0.139 a.u) for $\nabla^2\rho(\vec{r}_c) < 0$. The Gaussian 16 package [67] we employed in our work (hereafter GAUSSIAN) provides AIM analysis with keywords AIM=All and Density=Current. However, the AIM calculations implemented in the GAUSSIAN often terminate prior to the calculation of density Laplacians $\nabla^2\rho(\vec{r}_c)$, which is more common with an increase in the topological complexity resulting from the increase of number of the atoms and their bonding networks. In particular, the AIM analysis does not have particular standards for weak interactions such as vdW, and hence, is unable to describe their repulsive and attractive components as well as the steric interactions between the molecules' constituent parts that impact their shape and conformation.

1.4.2 RDG Analysis

In 2010, Johnson et al. [68] introduced a novel technique, based on a dimensionless quantity called reduced electron density gradient (RDG), that allows real-space imaging of the various kinds of NCIs in the molecular systems. Additionally, with the map of RDG for the sign of the second principal local density curvature (second largest eigenvalue of electron density Hessian matrix) multiplied by electron density, one can visually rank the relative strengths of NCIs and distinguish their repulsive and attractive components. Specifically, this technique was extensively

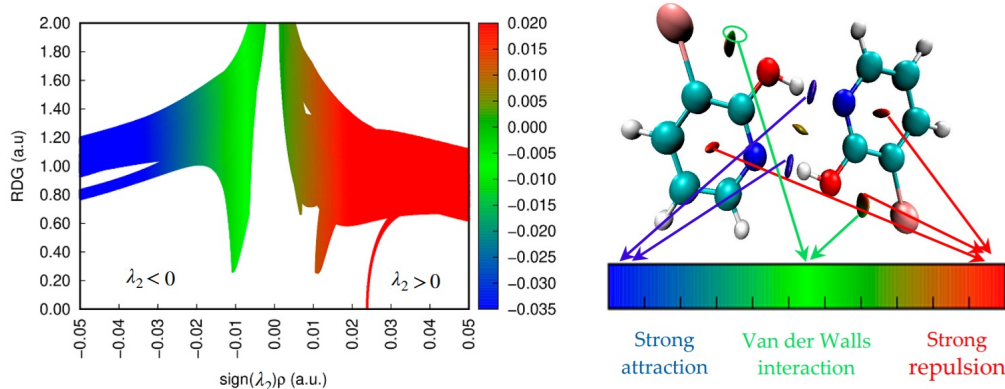


FIGURE 1.2: Representative RDG scatter plot (left) and NCIs mapping (right) for 3-bromo-2-hydroxypyridine dimer showing all three interactions. Figure adapted from Ref. [70].

examined to demonstrate its ability to differentiate between H-bonds, vdW interactions, and steric effects. The RDG is determined as [69]

$$s[\rho(\vec{r})] = \frac{1}{2(3\pi^2)^{1/3}} \frac{|\rho(\vec{r})|}{\rho(\vec{r})^{4/3}}. \quad (1.7)$$

The NCI analysis through RDG relies on the examination of the low-density gradient responsible for weak interactions, while the high-density gradient corresponds to strong interactions. When accompanied by the sign of the second largest eigenvalue λ_2 of the electron density Hessian matrix, the map of s versus $\text{sign}(\lambda_2) \times \rho(\vec{r})$ identifies the three different interaction types. A low-density, low-gradient inverted spike (trough) lying on the left side of the RDG map for $\lambda_2 < 0$ is indicative of non-covalent stabilizing interaction like H-bonding, while the spike lying on the right side for $\lambda_2 > 0$ represents non-covalent repulsive steric interactions. For both, the electron density values would lie in the range $(0.005 < \rho < 0.05 \text{ a.u.})$. Additionally, either side spikes around $\text{sign}(\lambda_2) \times \rho(\vec{r}) \simeq 0$ in the RDG map corresponds to weak interactions, like the vdW dispersion interactions with the electron density value $\rho < 0.005 \text{ a.u.}$ When the signs and magnitudes are color-coded and mapped to the system in real space, different types of interaction between the atoms, groups, or molecules can be directly visualized as illustrated in Fig. 1.2 for a bromo-hydroxypyridine dimer. The RDG calculations can be performed using a versatile

program called Multiwfn [71], and the RDG map plotting and visualization can be done using VMD software [72]. However, we note in passing that the RDG approach is not exclusive to NCI and can also be applied to strong interactions such as covalent bonds, ionic bonds, and charge-shift bonds [73]. We have carried out NCI analysis through RDG calculations in a variety of systems undertaken in our work where weak interactions are potentially important in stabilizing the structures. The electric field response of such systems constitutes one of the major themes of the work undertaken.

We now shift our attention to the electric field effects within the DFT computations, which constitute the primary focus of the work in the thesis.

1.5 Electric Field Effects

In DFT formalism, the effects of electric fields are investigated radially by examining modifications in the electron density caused by the field. This is because all physical quantities can be derived from the electron density $\rho(\vec{r})$ or the energy density functional $E[\rho(\vec{r})]$ and its derivatives. The energy, geometry, and electronic structure of the system are then influenced, which in turn affects the molecular orbitals, their energies and electrical properties like electric dipole and higher multipole moments. Moreover, the multipole expansion shows the characteristic way the various multipole moments couple with the external field $F_{i=x,y,z}$ and field gradients $F'_{ij=x,y,z} = \partial F_i / \partial x_j$, expressed as [74, 75]

$$E(\vec{F}) = E(0) - \mu_i^T F_i - \frac{1}{3} \Theta_{ij}^T F'_{ij} - \frac{1}{15} \Omega_{ijk}^T F''_{ijk} - \frac{1}{105} \Phi_{ijkl}^T F'''_{ijkl} - \dots, \quad (1.8)$$

where repeated pair indices are implicitly summed over and the superscript “ T ” denotes total (permanent plus induced) moments. This is known as Buckingham expansion, wherein the higher order multipoles (quadrupole, octopole, hexadecapole and so on) are expressed in traceless form, i.e., $\Theta_{ii}^T = \Omega_{ijj}^T = \Phi_{ijkk}^T = \dots = 0$.

In general, quadrupole (and higher) moments are of significance only when the dipole moment is zero. Moreover, it should be stressed that only the first non-vanishing moment is independent of the choice of origin of the coordinate system employed for its calculation. Thus, in a neutral and polar molecule or cluster, dipole moment $\vec{\mu}$ is the lowest non-vanishing moment that remains invariant under the translation of the origin of the coordinate system. The dipole moment is a measure of the asymmetry in the molecular charge distribution and is evaluated as the first derivative of the energy with respect to an applied electric field, i.e.,

$$\mu_i^T = -\frac{\partial E}{\partial F_i}. \quad (1.9)$$

Also that,

$$\begin{aligned} \mu_i^T &= \int \rho(\vec{r}) r_i d^3r, \\ &= \mu_i^0 + \mu_i^{induced}, \end{aligned} \quad (1.10)$$

where $\mu_i^0 = \int \rho^0(\vec{r}) r_i d^3r$ is the permanent dipole moment corresponding to the unperturbed electron density $\rho^0(\vec{r})$ in the absence of field, while the induced dipole moment is expressed as

$$\mu_i^{induced} = \alpha_{ij} F_j + \frac{1}{2} \beta_{ijk} F_j F_k + \frac{1}{6} \gamma_{ijkl} F_j F_k F_l + \dots \quad (1.11)$$

It is evident that the linear response of the system to the applied field is governed by the dipole-dipole polarizability α_{ij} , while the other properties, viz., the first dipole hyperpolarizability β_{ijk} , second dipole hyperpolarizability γ_{ijkl} , etc., describe the non-linear response.

Yet, another way of obtaining information about electron density distribution is by computing the polarizability, which can be obtained as the second derivative of the energy with the electric field components, i.e., $\alpha_{ij} = \partial \mu_i^T / \partial F_j =$

$-\partial^2 E / \partial F_i \partial F_j$. Likewise, the quadrupole moments

$$\begin{aligned}\Theta_{ij}^T &= \int \rho(\vec{r}) r_i r_j d^3 r_i d^3 r_j, \\ &= -3 \frac{\partial E}{\partial F_{ij}'},\end{aligned}\tag{1.12}$$

which is a second-order approximation (second moment) of the electron density distribution that provides an approximate understanding of its shape. Equal Θ_{ii}^T components, for instance, signify a spherical density distribution, whereas elongation along an axis would be indicated by a corresponding component significantly larger than the rest.

Additionally, within the framework of DFT, it is appealing to characterize the reactivity of molecular systems through parameters called reactivity indices [76, 77]. For instance, chemical hardness is an index that quantifies molecular systems' ability to withstand electron density polarization, expressed as the energy difference between the highest occupied molecular orbital (HOMO) and the lowest unoccupied molecular orbital (LUMO), i.e., $\eta = E_{LUMO} - E_{HOMO}$. Thus, low polarizable species are termed as "hard" and highly polarizable species as "soft". Similarly, electronegativity, $\chi = -(E_{LUMO} + E_{HOMO})/2$, is an indicator of species' ability to attract electron density toward itself, while electrophilicity, $\omega = -\eta^2/2\chi$, quantifies systems' ability to add electron density. It is interesting to investigate how field affects reactivity indices because it provides insight into how molecular systems adapt to the applied external fields.

In GAUSSIAN, the electric field is effected though a keyword `Field=X-10`, which denotes a uniform dipolar field (as in a parallel plate capacitor) of magnitude 0.0010 a.u. applied along the +X direction. The non uniform field can be applied with keywords like `Field=XXYZ-10`, which indicates a hexadecapole field with magnitude 0.0010 a.u., however, the geometry optimization process often terminates abruptly and the computations rather notoriously expensive.

1.5.1 Molecular Response to Electric Field

Depending on the strength and gradients of the external electric field \vec{F} , the electron density $\rho(\vec{r})$ will be redistributed, thereby affecting the electric dipole moment and other higher moments. An immediate consequence of the redistribution of electron density in a molecule is the strengthening or weakening of bonds in response to the applied field. Within the linear response, the dipole-field interaction mostly dictates the orientation of the molecule in order to minimize the interaction energy, $U = -\vec{\mu} \cdot \vec{F} = -\mu_i^T F_i$, by increasing dipole alignment along the field direction when field intensity is increased. The linear increase of the dipole moment of a molecule with field strength is typical of the linear response of the molecule to the applied field. Moreover, the dipole-field interaction is particularly important in the H-bonding networks, such as those found in water clusters, wherein the dipole orientation of each molecule along the field direction becomes so important that the H-bonding networks break up in an enhanced field, causing structural breakdown and configurational transition marked by a significant increase in the dipole moment.

Molecular response to the applied field can be gauged in terms of modulation of the frontier orbitals and their energies. In general, the delocalized orbitals are susceptible to polarization by the applied electric field, resulting in migration and localization of the orbitals with enhanced energy, while delocalization yields a decrease in orbital energy. As a consequence, the energy difference between the HOMO and LUMO gets modulated. The field modulation of the HOMO-LUMO (HL) gap is particularly appealing when the energy gap is in the relevant operational range (0.5 to 3 eV) for optoelectronic device applications.

Additionally, studying the field evolution of the vibrational spectra provides a detailed perspective on the molecular response to the applied field. As the electric fields also perturb the potential v_{ext} resulting from the atomic nuclei, which has a direct bearing on the electron density $\rho(\vec{r})$ in accordance with the

HK first theorem, and hence the nuclear motion and the vibrational levels that consequently alter the vibrational spectrum. A typical shift of stretching vibrational peak towards a lower wavenumber $\bar{\nu}$ (red shift) indicates the lengthening or weakening of the bond, while a shift towards a higher wavenumber (blue shift) is indicative of the shortening or strengthening of the bond. Quantitative analysis of the observed field effects on the vibrational frequencies has interesting applications in the characterization of various NCIs through the vibrational Stark effect, which provides a direct mapping between the observed vibrational frequencies and the local electric fields that have characteristic range for various NCIs [78]. All these make electric field effect on vibrational spectra a rich field for exploration from both experimental and theoretical perspectives. Theoretical background on vibrational frequency shift due to applied field is presented in the next section.

1.5.2 Geometry Optimization in Field

Geometry optimization is a systematic process of repositioning the atoms in a molecular system to obtain the most stable structural configuration characterized by the lowest energy within the variational principle and the self-consistent field calculations with predefined thresholds [79]. This is more involved in the DFT computation on account of various energy density functionals, resulting in a detailed topology of the multi-dimensional potential energy surface (PES) of the molecular system, while the applied electric field acts an additional dimension. Each point on the PES represents a particular structure with energy corresponding to its position on the PES [79, 80]. Locating a local minimum on the PES, thereby achieving its equilibrium configuration, is the ultimate goal of all optimization methods. The schematic displayed in Fig. 1.3 provides an overview of the fundamental elements of the PES. In order to find a local minimum on the PES, it is desirable to simultaneously optimize all parameters affecting the energy of the system, resulting in a minimum energy structure. A good “guess” geometry

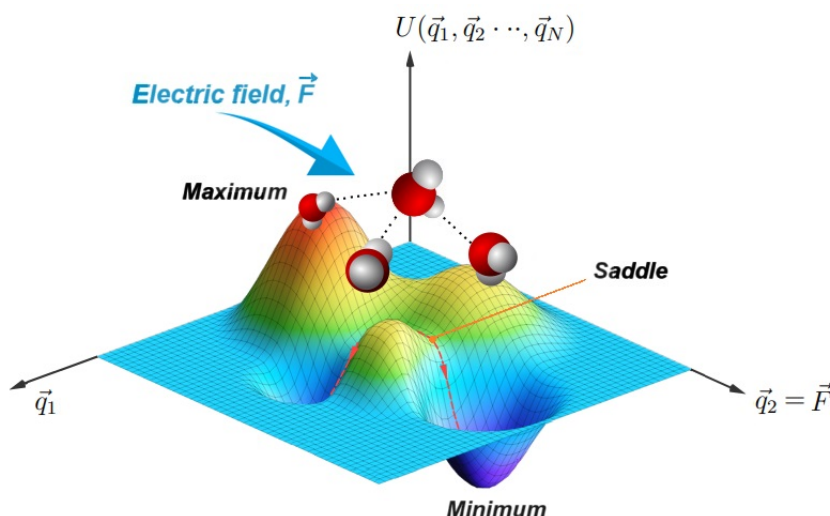


FIGURE 1.3: An illustrative potential energy surface of a water tetramer depending on the generalized coordinates $(\vec{q}_1, \vec{q}_2, \dots, \vec{q}_N)$ with maxima, minima and saddle points. The generalized coordinates include the applied electric field, \vec{F} .

for the input, usually obtained from semi-empirical computation helps to quickly locate the local minimum.

It is usual for systems having weak interactions to exhibit essentially a flat PES with indiscernible features (local maximum, local minimum and saddle point) on their PES. However, the externally applied field modifies the PES, thereby forcing the system into the local minimum on the PES. Geometry optimization in the external field determines not only the structural characteristics like bond lengths and angles but also defines the preferred orientation of the molecule with respect to the field. However, extreme geometric distortion at large field strengths would often force the geometry into a transition state (first-order saddle point) characterized by one imaginary vibrational frequency. The characteristic vibrational frequencies of a molecular system are routinely calculated from the Hessian matrix at a stationary point (a zero gradient point on the PES) by evaluating the eigenvalues of the mass-weighted Hessian matrix. The Hessian matrix describing the local curvature on the PES is composed of the second-order derivatives of the potential energy function $U(\vec{q}_1, \vec{q}_2, \dots, \vec{q}_N)$ of the molecular system with respect to the nuclear coordinates $(\vec{q}_1, \vec{q}_2, \dots, \vec{q}_N)$, i.e., $H_{ij} = \partial^2 U / \partial q_i \partial q_j$. When there are both

positive and negative Hessian matrix eigenvalues, the stationary point is called a saddle point, while when there are just positive or negative eigenvalues, a local minimum or maximum on the PES is attained. The stationary point is therefore a local minimum if all vibrational frequencies are real, but first-order or higher-order saddle points if one or more vibrational frequencies are imaginary. Field effects can be examined by calculating derivative properties such as polarizabilities and hyperpolarizabilities, which depend on the second and higher derivative of the energy function with respect to electric fields.

Geometry determination and computation of characteristics in the presence of an electric field strongly depend on the quality of the basis set employed to simulate changes in the orbitals' size and shape in the field. The polarization and diffuse functions provide the necessary flexibility and adaptability to the orbitals in the field, which makes an extended basis set highly essential for calculations in the presence of field. Hundreds of basis sets suitable for calculations in field are available in the database [81, 82]. While it is possible to import basis sets from the database using the keyword "Gen", basis sets that are internally stored in the GAUSSIAN, like Pople's basis set (e.g., 6-311++G(d,p)) [83, 84] or Dunning's basis set (e.g., aug-cc-pVDZ) [85], are adequate for reasonable description in the field. In our work, we have employed Pople's split-valence basis sets.

1.5.3 Vibrational Stark Effect

The primary effect of an electric field \vec{F} on a molecular vibration is the interaction of the field with the dipole moment of vibrational modes, resulting in a difference in the dipole moment $\Delta\vec{\mu}$ between the molecule in the ground state vibrational mode, ν_0 and the corresponding excited state vibrational mode, ν . For a relatively low field strength, the change in the frequency is a linear function of the applied

field \vec{F} , i.e. [86–88],

$$\Delta\bar{\nu} = \bar{\nu} - \bar{\nu}_0 = -\frac{1}{hc}\Delta\vec{\mu} \cdot \vec{F} \quad (1.13)$$

This phenomenon is termed as the vibrational Stark effect (VSE) [89–91]. The difference dipole moment of the vibrational modes $|\Delta\vec{\mu}|$ is known as Stark tuning rate and is usually expressed in units of $\text{cm}^{-1}/(\text{MV}/\text{cm})$. An interesting application of VSE is in the determination of the component of the local electric field along $\Delta\vec{\mu}$ at the site of vibrational probes, e.g., stretching of $-\text{C}=\text{O}$ (carbonyl), $-\text{C}\equiv\text{N}$ (nitrile) and $-\text{N}=\text{O}$ (nitrosyl) groups, or stretching of diatomic molecules, such as carbon monoxide (CO) and nitric oxide (NO) adsorbed on a surface [92]. With the frequency shift $\Delta\bar{\nu}_{probe}$ of a matrix isolated chemisorbed or physisorbed vibrational probe calibrated in the known field values $\{\vec{F}\}$, $|\Delta\vec{\mu}_{probe}|$ is determined. This is then used in determining the local field \vec{F}_{local} at a specific probe site of interest by recording the observed change in the frequency $\Delta\bar{\nu}_{obs}$ of the probe in accordance to the relation,

$$\Delta\bar{\nu}_{obs} = -\frac{1}{hc}\Delta\vec{\mu}_{probe} \cdot \vec{F}_{local}. \quad (1.14)$$

For the diatomic vibrational probes, the orientation of $\Delta\vec{\mu}_{probe}$ is known to be along the bond axis. In practice, the determination of $|\Delta\vec{\mu}_{probe}|$ of a matrix-isolated vibrational probe is complicated by the local field effect. What one actually determines is $|\Delta\vec{\mu}_{probe}|/f$, not $|\Delta\vec{\mu}_{probe}|$, where f is the local field correction factor that relates the actual local field \vec{F}_{local}^{matrix} that the matrix-isolated vibrational probe experiences to the external applied field \vec{F} as, $\vec{F}_{local}^{matrix} = f\vec{F}$. Accordingly, the effective local field at the probe site is \vec{F}_{local}/f . The value of f is estimated to lie between 1 and 2 [93, 94]. Thus, accuracy in the determination of field through VSE is limited by an unreliable estimate for f .

The other appealing application of VSE is the characterization of various NCIs on account of characteristic field strength associated with the interaction.

Significant advancements have been made in this direction [78, 94].

1.5.4 Water in Electric Field

Water being polar is very sensitive to an electric field. Stark effect measurement yields the dipole moment of a water molecule to be 1.84 Debye [95], while that in the condensed phases (ice, liquid) typically range from 2.4 to 3.0 Debye [96], which is greater than that for an isolated water molecule due to electric field effects of the neighboring molecules resulting in mutual polarization and dipole enhancement. In many technological device setups, interfaces, and physical and biological systems, water is routinely exposed to external electric fields of a few tens of V/Å. This is something we scarcely notice, however, the deflection of a thin stream of water when it comes into close contact with a charged object is the most classic demonstration of how an electric field affects water [97]. A more fascinating effect is the formation of a floating water bridge, which is a watery thread formed between two water reservoirs with electrodes immersed and maintained at a potential difference ~ 15 KV or more [98, 99]. Electrofreezing [100–102], i.e., the electric field-induced crystallization is another effect that would result from the preferential ordering of the H-bond network in the field necessary for crystallization to occur against the detrimental forces originating from thermal disruption, cooperativity of H-bonding, etc.

It has always been a goal to fully comprehend the behaviors of the bulk water from the molecular level studies considering the rich behavior of water structure related to the extraordinary adaptability of water's H-bonding networks to external electric fields, but in many situations, this has been accomplished only partially and often with uncertain outcomes or mixed results [103]. A very recent molecular dynamics (MD) simulations study of liquid water in electric fields has revealed a field-induced reduction of entropy of bulk water, however, small compared to that in the usual freezing phenomenon [104]. Another important aspect

influencing the characteristics of water is spatial confinement, which has tremendous technological implications. Thus, we will quickly go over the characteristics of water in confinement.

1.6 Water in Confinement

Water in confinement forms tightly-bonded H-bonding networks resulting from strong interaction between the water molecules, while weak interaction with the confining walls, gives confined water its unusual properties not present in liquid water [22, 105]. Spatial confinement substantially modifies the physical, thermodynamic, and dynamic properties of water in the account of changes in the structure of the H-bonding networks. Examples of confinement include water between hydrophobic graphene sheets [106–110], in molecular cavities [111–113] and carbon nanotubes (CNTs) [106, 114–116], and in nanoporous materials [117–119]. Furthermore, confined water is common in biological systems like proteins and membranes, in geological confined pores found in rocks and minerals, and in the vascular bundles of living plants [120].

Understanding the properties of confined water is important for numerous potential applications such as nanofluidic devices [15], hydrovoltaic power generation [121], water treatment technologies [122], and more [123]. Numerous studies have demonstrated that the behaviors of confined water depend strongly on the confinement size and elegant balance between intermolecular interactions and its interaction with the surface that encloses it. The properties of confined water that hold great significance in technological applications include unusually low dielectric constant [27–29], high proton conductivity [30–34], and increased thermal conductivity that may be regulated by an external electric field. These diverse properties of confined water might open up new avenues in nanoscience and could be crucial for the development of water-based device technologies in the near future.

1.6.1 Confinement by Hydrophobic Surfaces

The behavior of water in hydrophobic confinement has been the focus of intense experimental and computational studies for numerous reasons, including its implications for nanoscience and nanotechnology. Its flow dynamics and other properties when confined between hydrophobic surfaces change significantly from those of bulk water. With the advent of experimental techniques and computational methodologies, significant progress has been made in elucidating unusual characteristic properties of water confined in CNTs and graphene layers that are often regarded as 1D and 2D hydrophobic confinements providing extensive, albeit weak π -electron interactions between the confining surface and water.

Dielectric measurement has shown that the water confined in nano-slit in graphene layers has a surprisingly low dielectric constant in the direction perpendicular to the surface, i.e., $\epsilon_r \approx 2$ against $\epsilon_r \approx 80$ for bulk water [27]. Classical MD simulations indicate that the anomalously low dielectric constant is due to long-ranged anisotropic dipole correlations, rather than due to structural features of interfacial water molecules [124], while a very recent *ab initio* MD simulations study asserts that it is due to ferroelectric ordering of interfacial water molecules [125]. The high proton conductivity of confined water in the CNTs or hydrophobic nanochannels is particularly important due to its technological relevance in energy applications, such as fuel cells, batteries, and photocatalytic water splitting for hydrogen production [126]. The fast proton conduction mechanism is attributed to the Grotthuss relay mechanism involving structural diffusion of excess protons (topological defects) in the H-bonded network [127]. However, several computational and experimental studies have demonstrated that the proton conductivity is extremely sensitive to confinement sizes, and as confinement size is enlarged, the proton transport rate becomes comparable to that of bulk water [128, 129]. Furthermore, even at temperatures as high as 300K or somewhat higher, the electric field applied along the CNTs' tube axis can trigger phase transitions of water, resulting in the formation of solid ice-like polygonal (pentagonal, hexagonal and

heptagonal) and spiral structures inside the CNTs [130–133]. Applications in nanotechnology may benefit from this phase behavior of water in carbon nanotubes.

The confinement of one or few water molecules within molecular cages or nanocavities, represents a special confinement that facilitates the study of fundamental characteristics of water molecules in isolation or extreme confinement. This type of confinement reveals the quantum properties of a water molecule [134–136], confinement-induced bonding [137], and other features that are crucial for the design of water-based molecular junction devices [36–38]. Therefore, we briefly review some of the key features of such confinement.

1.6.2 Confinement in Molecular Cages

When a water molecule is confined inside a molecular cage, like fullerene C_{60} or C_{70} , it reveals its fundamental characteristics including quantum features, which are normally obscured by strong interactions with the surrounding molecules. Thus, in the account of negligible or relatively weak interaction between the water molecule and the confining wall, the fullerene can be thought of as a nano lab for studying the fundamental characteristics of a water molecule. As observed, cf. Fig. 1.4, the encaged water molecule displays its spin isomers, ortho and para [134, 136, 138]. Also, the electrostatic shielding behavior of fullerene cages has been extensively

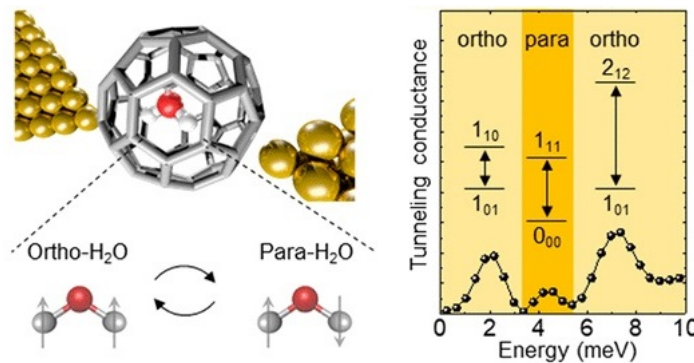


FIGURE 1.4: Conductance measurement in a $H_2O@C_{60}$ junction setup revealing spin isomer state of a water molecule confined in C_{60} fullerene. Figure adapted from Ref. [138].

investigated [37, 139–141] and it would be fascinating to find out if an electric field can be effectively shielded by a covalently bonded cage or a H-bonded cage.

One peculiarity of the encaged water molecule is its reduced dipole moment, which is significantly less than its gas phase value of 1.84 Debye [142]. Nevertheless, an external electric field may be able to modify the net polarization and ferroelectricity that arise from water dipoles being trapped in C₆₀ crystal resulting in H₂O@C₆₀ crystal [143]. Also, an electric field can be used to force fullerene containing a water molecule through a carbon nanotube (CNT), thereby opening up new opportunities for applications in nanotechnology. Furthermore, the extreme nanoscale confinement provided by the smaller fullerenes (<C₆₀) may facilitate some exceptional reactions to undergo which otherwise is not possible, such as synthesis of hyper-hydrogenated water H₄O [144]. Also, such confinement may induce unconventional chemical bonding, such as O–O covalent bond between two water molecules inside C₃₆ due to charge transfer between water dimer and fullerene [137].

Our work, as presented in this thesis, focuses on the response of a water molecule imprisoned in small fullerenes. Also, the structured water-chains with specific geometric patterns extended in one direction, typically found in MOFs that provide the necessary coordination in maintaining their unusual elongated linear or helical structures, are studied. Although such structured water-chains are not stable in isolation, however, the electrostatic environment provided by an applied field would enable the formation of such structures. In practice, an opportunity to explore such structured water-chains may arise from water bridging the nanoscale gap between the probe tip and substrate in an atomic force microscopy (AFM) setup. Thus, we briefly summarize research on a nanoscale water bridge.

1.6.3 Nanoscale Water Bridge

The water channel between the tip and substrate held within a nanometric distance is often formed by a nanometric cluster of water molecules in an AFM setup working in a humid environment [145, 146]. A force-distance plot analysis in such a setup can be used to analyze the structural evolution of water confined between a probe and substrate in air, such as the coil-to-bridge transition of self-assembled water chain [147]. An in-depth analysis of the structures and properties of such confined water in an ambient environment is crucial in water-based nanoscience and technology [121–123], including energy dissipation management [35] and the development of structurally flexible nanodevices. Furthermore, an electric field

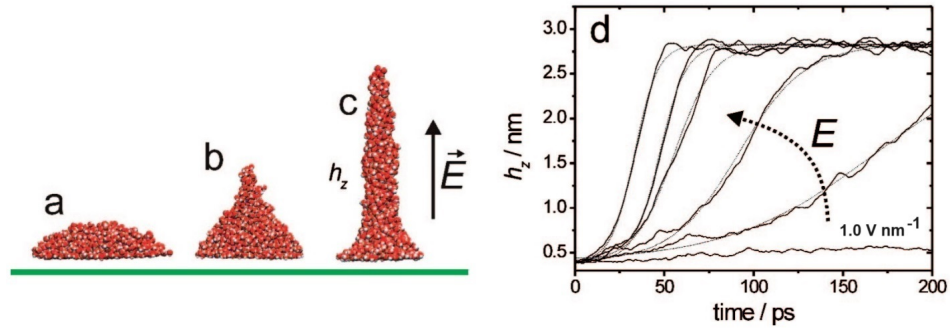
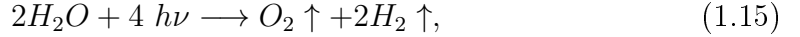


FIGURE 1.5: Field-induced nanoscale water pillar in MD simulations resembling water bridge observed in AFM experiments with snapshots at (a) $t = 0$, (b) $t = 35$ ps, (c) $t = 75$ ps, for field 2.0 V nm^{-1} , and (d) height evolution for field increased in step of 0.25 V nm^{-1} starting at 1.0 V nm^{-1} . Figure adapted from Ref. [149].

can be used to control a droplet of water to create a water pillar that resembles the water bridge observed in AFM experiments [148, 149]. As shown in Fig. 1.5, this type of field-induced water bridge occurs above a few V nm^{-1} threshold field, which is caused by the orientational confinement of water dipoles winning out, due to their increased polarizability in the field, over the competitive effects from surface energy and water condensation from the humid air. Manipulation of the properties of such water bridges by an external field could be useful in nanoscience and nanotechnology [150, 151].

1.7 Photolysis of water

In this section, we briefly review the photolysis of water for hydrogen production following the initial report by Fujishima and Honda in 1972 [152]. As demonstrated, a semiconductor material like TiO_2 with an appropriate energy band gap immersed in water can absorb photons and split water when exposed to solar radiation. An oxidation reaction occurs at the TiO_2 electrode, while a reduction reaction occurs at the counter electrode (Pt), which is externally coupled to the TiO_2 electrode, resulting in an overall reaction,



with solar-to-hydrogen conversion efficiency, $\eta_{STH} < 1$. Though significant attempts have been made to increase the conversion efficiency, it is still far from being commercially viable. Nevertheless, the Fujishima-Honda experiment has been instrumental in the advancement of direct solar-to-hydrogen conversion techniques, which also includes the photocatalytic methods [153]. Unlike the photovoltaic (PV) cell-driven electrolysis of water [154], which is an indirect method of water splitting, the direct method can be miniaturized into nano- or molecular-level devices.

As is known and discussed in the preceding sections, nanoconfined water has properties different from bulk water. A few characteristics of nanoconfined water, such as an abnormally low dielectric constant [27–29] and high proton conductivity [30–34], can be exploited in designing efficient nanodevices for photolysis. The majority of photocatalytic techniques suffer energy loss due to electron-hole recombination, however, this can be avoided by using 2D-hetero-junction bilayer transition-metal dichalcogenide (TMD) materials, which have an incredibly low rate of electron-hole recombination due to the formation of interlayer excitons upon photoexcitation [155, 156]. In particular, the screw dislocation-driven crystal growth results in spiral pyramid-shaped TMDs [157, 158], while suitable gaps

between the successive bilayer spirals can be used to nano-confine water such that photolysis can occur when exposed to sunlight.

The final chapter delves more into this subject and examines the implications of our work on the photolysis of water in this kind of setup. Herewith, we present the thesis outline.

1.8 Thesis Outline

The purpose of this thesis is to study some exotic nano-water structures, such as the structured water nano-chains and nano-rings, their energetics, electronic properties and response to the external electric field. They are usually present in nano-confined environments in MOFs that provide the necessary coordination to maintain their structures extended against otherwise clustering up to form arbitrary closed configurations. The work also includes the response of a water molecule in extreme confinement, such as inside a small fullerene, to an external field. Clathrate hydrate structures are also examined for any modification caused by an applied electric field for potential applications for gas capture, storage, or release.

Each chapter begins with an abstract of the work presented in the chapter. The background materials relevant to the works carried out in the thesis are provided in Chapter 1. In subsequent chapters, the background information that serves as a literature review for the specific work is presented after the chapter abstract. Relevant computational methodology, strategy and computed results are presented, and the conclusions and implications are provided at the end. In Chapter 2, we investigate within the DFT computational framework, the structural, energetic and electronic properties of the structured water chains, which are the elongated network of 4-, 5- or 6-membered ring water clusters that have overall appearances of the tape- or ribbon-like structures. Such structures manifest naturally in the nano-confined environment present in the MOFs. Their response

to applied uniform and static electric field is explored for potential device applications that exploit their in-field structural behaviors and the associated properties. In order to investigate the electric field response of ring-shaped structured water, we take into consideration water nano-rings, which are H-bonded rings of a few nm-diameter twisted ribbon-like network of water molecules. Their potential implications for device applications are analyzed in light of their structural features and field evolution, and other attributes of relevance. These are presented in Chapter 3. In Chapter 4, we explore the response of a water molecule confined in small fullerenes, like C_n ($n = 28, 30, 32$), to the external electric fields. Stability and field evolution of the building blocks of CO clathrate hydrate structures, viz., $CO@5^{12}$, $CO@5^{12}6^2$, and $CO@5^{12}6^4$ are also examined in light of possible field-induced gas capture, storage, or release applications. Finally, Chapter 5 summarizes the key findings of the work presented in the thesis and discusses potential opportunities and possible directions for future research that are worthy of systematic exploration.

References

- [1] P. Jena and A. W. Castleman, Jr. *Proc. Natl. Acad. Sci. U.S.A.* **103**, 10560 (2006).
- [2] G. Schmid and D. Fenske, *Phil. Trans. R. Soc. A* **368**, 1207 (2010).
- [3] B. Ni, Y. Shi, and X. Wang, *Adv. Mater.* **30**, 1802031 (2018).
- [4] H. Park, D. J. Shin, and J. Yu, *J. Chem. Educ.* **98**, 703 (2021).
- [5] R. Ludwig *Angew. Chem. Int. Ed.* **40**, 1808 (2001).
- [6] F. N. Keutsch and R. J. Saykally, *Proc. Natl. Acad. Sci. U.S.A.* **98**, 10533 (2001).
- [7] D. T. Gomez, L. R. Pratt, D. N. Asthagiri, and S. B. Rempe, *Acc. Chem. Res.* **55**, 2201 (2022).
- [8] V. Zaverkin, D. Holzmüller, R. Schuldt, and J. Kästner, *J. Chem. Phys.* **156**, 114103 (2022).
- [9] A. Pinkard, A. M. Champsaur, and X. Roy, *Acc. Chem. Res.* **51**, 919 (2018).
- [10] A. Braschinsky and J. W. Steed, *Coord. Chem. Rev.* **473**, 214840 (2022).
- [11] A. Borgoo, D. J. Tozer, P. Geerlings, and F. De Proft, *Phys. Chem. Chem. Phys.* **10**, 1406 (2008).
- [12] H. Takezawa and M. Fujita, *Bull. Chem. Soc. Jpn.* **94**, 2351 (2021).
- [13] S. H. Petrosko, R. Johnson, H. White, and C. A. Mirkin, *J. Am. Chem. Soc.* **138**, 7443 (2016).
- [14] K. E. Gubbins, Y. -C. Liu, J. D. Morrewa, and J. C. Palmer, *Phys. Chem. Chem. Phys.* **13**, 58 (2011).

- [15] Z. G. Chiragwandi, O. Nur, M. Willander, and N. Calander, *App. Phys. Lett.* **85**, 5310 (2003).
- [16] H. Sabzyan and M. Kowsar, *Phys. Chem. Chem. Phys.* **19**, 12384 (2017).
- [17] R. E. Jacobsen, S. Arslanagic and A. V. Lavrinenko, *Appl. Phys. Rev.* **8**, 041304 (2021).
- [18] Y. Lu, et al., *Research (Wash DC)* 7505638 (2021).
- [19] A. Buchmann, C. Hoberg, and F. Novelli, *APL Photonics*, **7**, 121302 (2022).
- [20] S. Melnik, A. Ryzhov, A. Kiselev, A. Radenovic, T. Weil, K. J. Stevenson, and V. G. Artemov, *J. Phys. Chem. Lett.* **14**, 6572 (2023).
- [21] F. Leoni, C. Calero, and G. Franzese, *ACS Nano*, **15**, 19864 (2021).
- [22] A. W. Knight, N. G. Kalugin, E. Coker, and A. G. Ilgen, *Sci. Rep.* **9**, 8246 (2019).
- [23] R. Mezzenga, *Front. Soft Matter*, **3**, 1324589 (2023).
- [24] L. Cheng, J. -B. Lin, J. -Z. Gong, A. -P. Sun, B. -H. Ye, and X. -M. Chen, *Cryst. Growth Des.* **6**, 2739 (2006).
- [25] J. -F. Song, J. Lu, Y. Chen, Y. -B. Liu, R. -S. Zhou, X. -Y. Xu, and J. -Q. Xu *Inorg. Chem. Commun.* **9**, 1079 (2006).
- [26] Q. Huang, L. Diao, C. Zhang, and F. Lei, *Molecules*, **16**, 2871 (2011).
- [27] L. Fumagalli, A. Esfandiar, R. Fabregas, S. Hu, P. Ares, A. Janardanan, Q. Yang, B. Radha, T. Taniguchi, K. Watanabe, G. Gomila, K. Novoselov and A. Geim, *Science*, **360**, 1339 (2018).
- [28] C. Zhang, *J. Chem. Phys.* **148**, 156101 (2018).
- [29] H. Zhu, F. Yang, Y. Zhu, A. Li, W. He, J. Huang, and G. Li, *RCS Adv.* **10**, 8628 (2020).

- [30] C. Dellago, M.M. Naor, and G. Hummer, *Phys. Rev. Lett.* **90**, 105902 (2003).
- [31] Z. Cao, Y. Peng, T. Yan, S. Li, A. Li, and G.A. Voth, *J. Am. Chem. Soc.* **132**, 11395 (2010).
- [32] I. A. Ryzhkin, M. I. Ryzhkin, A. M. Kashin, E. A. Galitskaya, and V. V. Sinitsyn, *EPL*, **126**, 36003 (2019).
- [33] K. -ichi Otake, et al., *Nat. Commun.* **11**, 843 (2020).
- [34] S. Kang, et al., *Chem. Mater.* **34**, 3967 (2022).
- [35] Y. Gao, M. Li, C. Zhan, H. Zhang, M. Yin, W. Lu, and B. Xu, *Adv. Mater.* **35**, 2303759 (2023).
- [36] C. Zhu and X. Wang, *Sci. Rep.* **5**, 17932 (2016).
- [37] S. Kaneko, Y. Hashikawa, S. Fujii, Y. Murata, and M. Kiguchi, *Chem. Phys. Chem.* **18**, 1229 (2017).
- [38] B. Liu, J. Chen, Y. Ouyang, M. Zhang, Y. -Z. Tan, and F. Song, *Chin. Phys. B* **32**, 063601 (2023).
- [39] E. D. Sloan, *Ind. Eng. Chem. Res.* **39**, 3123 (2000).
- [40] C. I. Ratcliffe, *Energy Fuels*, **36**, 10412 (2022).
- [41] H. P. Veluswamy, R. Kumar, and P. Linga, *Appl. Energy*, **122**, 112 (2014).
- [42] A. Hassanpouryouzband, et al., *Chem. Soc. Rev.* **49**, 5225 (2020).
- [43] R. G. Parr and W. Yang, *Density-Functional Theory of Atoms and Molecules*, Oxford University Press, New York (1989).
- [44] *Density Functional Theory: Modeling, Mathematical Analysis, Computational Methods, and Applications*, edited by E. Cancès and G. Friesecke, Springer Cham (2023).

- [45] A. D. Becke, *J. Chem. Phys.* **140**, 18A301 (2014).
- [46] T. van Mourik, M. Bühl and M. -P. Gaigeot, *Philos. Trans. A Math. Phys. Eng. Sci.* **13**, 20120488 (2014).
- [47] R. O. Jones, *Rev. Mod. Phys.* **87**, 897 (2015).
- [48] N. Mardirossian and M. H. -Gordon, *Mol. Phys.* **115**, 2315 (2017).
- [49] L. H. Thomas, *Math. Proc. Camb. Philos. Soc.* **23**, 542 (1927).
- [50] E. Fermi, *Rend. Accad. Naz. Lincei.* **6**, 602 (1927).
- [51] P. Hohenberg and W. Kohn, *Phys. Rev.* **136**, B864 (1964).
- [52] W. Kohn and L. J. Sham, *Phys. Rev.* **140**, A1133 (1965).
- [53] A. D. Becke, *J. Phys. Chem.* **98**, 5648 (1993).
- [54] J. B. Foresman and Æ. Frisch, *Exploring Chemistry with Electronic Structure Methods*, 2nd ed., Gaussian, Inc. Pittsburgh, PA (1996).
- [55] S. H. Vosko, L. Wilk, and M. Nusair, *Can. J. Phys.* **58**, 1200 (1980).
- [56] A. D. Becke, *Phys. Rev. A* **38**, 3098 (1988).
- [57] C. Lee, W. Yang, and R. G. Parr, *Phys. Rev. B* **37**, 785 (1988).
- [58] J. P. Perdew, K. Burke, and M. Ernzerhof, *Phys. Rev. Lett.*, **77**, 3865 (1996).
- [59] S. F. Sousa, P. A. Fernandes, and M. J. Ramos, *J. Phys. Chem. A* **111**, 10439 (2007).
- [60] J. T. -Rives and W. L. Jorgensen, *J. Chem. Theory Comput.* **4**, 297 (2008).
- [61] Y. Zhao and D. G. Truhlar, *Acc. Chem. Res.* **41**, 157 (2008).
- [62] B. Santra, et al., *Chem. Phys.* **139**, 154702 (2013).

- [63] S. Grimme, *J. Comput. Chem.* **27**, 1787 (2006).
- [64] J. -D. Chai and M. H. -Gordon, *Phys. Chem. Chem. Phys.* **18**, 6615 (2008).
- [65] Y. Zhao and D. G. Truhlar, *Theor. Chem. Acc.* **120**, 215 (2008).
- [66] F. W. R. Bader, *Atoms in Molecules: A Quantum Theory*, Oxford University Press, Oxford (1990).
- [67] M.J. Frisch, et al., Gaussian 16, Revision C.01 (Gaussian, Inc., Wallingford, CT, 2016).
- [68] E.R. Johnson, S. Keinan, P.M. -Sánchez, J.C. -García, A. J. Cohen and W. Yang, *J. Am. Chem. Soc.* **132**, 6498 (2010).
- [69] G. Saleh, C. Gatti, and L. Lo Presti, *Comput. Theor. Chem.* **998**, 148 (2012).
- [70] N. Lefi, A. S. Kazachenko, M. Raja, N. Issaoui, and A.S. Kazachenko, *Molecules* **28**, 2669 (2023).
- [71] T. Lu and F. Chen, *J. Comput. Chem.* **33**, 580 (2012).
- [72] W. Humphrey, A. Dalke and K. Schulten, *J. Mol. Graph.* **14**, 33 (1996).
- [73] R. A. Boto, J. -P. Piquemal, J. C. -Garcia, *Theor. Chem. Acc.* **136**, 139 (2017).
- [74] A. D. Buckingham, *J. Chem. Phys.* **30**, 1581 (1959).
- [75] A. D. Mclean and M. Yoshimine, *J. Chem. Phys.* **47**, 1927 (1967).
- [76] R. G. Pearson, *J. Chem. Sci.* **117**, 369 (2005).
- [77] R. Pal and P. K. Chattaraj, *J. Indian Chem. Soc.* **98**, 100008 (2021).
- [78] S. D. Fried and S. G. Boxer, *Acc. Chem. Res* **48**, 998 (2015).
- [79] E. G. Lewars, *Computational Chemistry*, Ch. 2, Springer Cham (2017).

- [80] D. G. Truhlar, in The Encyclopedia of Physical Science and Technology, 3rd ed., edited by R. A. Meyers, Academic Press, New, York (2001).
- [81] K. L. Schuchardt, B. T. Didier, T. Elsethagen, L. Sun, V. Gurumoorthi, J. Chase, J. Li, and T. L. Windus, *J. Chem. Inf. Model.* **47**, 1045 (2007).
- [82] B. P. Pritchard, D. Altarawy, B. Didier, T. D. Gibson, and T. L. Windus, *J. Chem. Inf. Model.* **59**, 4814 (2019).
- [83] W. J. Hehre, R. Ditchfield, and J. A. Pople, *J. Chem. Phys.* **56**, 2257 (1972).
- [84] V. A. Rassolov, J. A. Pople, M. A. Ratner, T. L. Windus, *J. Chem. Phys.* **109**, 1223 (1998).
- [85] T. H. Dunning, Jr. *J. Chem. Phys.* **90**, 1007 (1989).
- [86] E. S. Park, S. S. Andrews, R. B. Hu, and S. G. Boxer, *J. Phys. Chem. B* **103**, 9813 (1999).
- [87] I. T. Suydam and S. G. Boxer, *Biochem.* **42**, 12050 (2003).
- [88] S. H. Schneider and S. G. Boxer, *J. Phys. Chem. B* **120**, 9672 (2016).
- [89] A. Chattopadhyay and S. G. Boxer, *J. Am. Chem. Soc.* **117**, 1449 (1995).
- [90] J. R. Reimers and N. S. Hush, *J. Phys. Chem. A* **103**, 10580 (1999).
- [91] S. H. Brewer and S. Franzen, *J. Chem. Phys.* **119**, 851 (2003).
- [92] S. D. Dalosto, J. M. Vanderkooi, and K. A. Sharp, *J. Phys. Chem. B* **108**, 6450 (2004).
- [93] N. S. Hush, and J. R. Reimers, *J. Phys. Chem.* **99**, 15798 (1995).
- [94] M. Saggiu, N. M. Levinson, and S. G. Boxer, *J. Am. Chem. Soc.* **133**, 17414 (2011).

- [95] S. A. Clough, Y. Beers, G. P. Klein, and L. S. Rothman, *J. Chem. Phys.* **59**, 2254 (1973).
- [96] A V. Gubskaya and P. G. Kusalik, *J. Chem. Phys.* **117**, 5290 (2002).
- [97] G. K. Vemulapalli and S. G. Kukolich, *J. Chem. Edu.* **73**, 887 (1996).
- [98] E. C. Fuchs, J. Woisetschlager, K. Gatterer, E. Maier, R. Pecnik, G. Holler, and H. Eisenkobl, *J. Phys. D: Appl. Phys.* **40**, 6112 (2007).
- [99] R.M. Namin, S.A. Lindi, A. Amjadi, N, Jafari, and P. Irajizad, *Phys. Rev. E* **88**, 033019 (2013).
- [100] R. Zangi and A. E. Mark, *J. Chem. Phys.* **120**, 7123 (2004).
- [101] W. Zhu, et al., *Nat. Commu.* **10**, 1925 (2019).
- [102] G. Cassone and F. Martelli, *Nat. Commu.* **15**, 185 (2024).
- [103] M. P. Andersson, *J. Mol. Liq.* **383**, 122169 (2023).
- [104] V.C. Nibali, S. Maiti, F. Saija, M. Heyden and G. Cassone, *J. Chem. Phys.* **58**, 184501 (2023).
- [105] H. R. Corti, et al., *Eur. Phys. J. E*, **44**, 136 (2021).
- [106] G. Cicero, J. C. Grossman, E. Schwegler, F. Gygi, and G. Galli, *J. Am. Chem. Soc.* **130**, 1871 (2008).
- [107] M. S. Fernandez, F. M. Peeters, and M. N. -Amal, *Phys. Rev. B* **94**, 045436 (2016).
- [108] Z. Gao, N. Giovambattista, and O. Sahin, *Sci. Rep.* **8**, 6228 (2018).
- [109] X. Cai, W. J. Xie, Y. Yang, Z. Long, J. Zhang, Z. Qiao, L. Yang, and Y. Q. Gao, *J. Chem. Phys.* **150**, 124703 (2019).
- [110] M. -L. Tseng, A. Adesiyani, A. Gassoumi, and N. E. Gorji, *J. Nanoparticle Res.* **25**, 51 (2023).

- [111] S. Vaitheeswaran, H. Yin, J. C. Rasaiah, and G. Hummer, *Proc. Natl. Acad. Sci. U.S.A.* **101**, 17002 (2004).
- [112] L. Wang, J. Zhao, and H. Fang, *J. Phys. Chem. C* **112**, 11779 (2008).
- [113] H. Yin, G. Feng, G. M. Clore, G. Hummer, and J. C. Rasaiah, *J. Phys. Chem. B* **114**, 16290 (2010).
- [114] J. Hassan, G. Diamantopoulos, D. Homouz, and G. Papavassiliou, *Nanotechnol. Rev.* **5**, 341 (2016).
- [115] Z. Wan, Y. Gao, X. Chen, X. C. Zeng, J. S. Francisco, and C. Zhu, *Proc. Natl. Acad. Sci. U.S.A.* **119**, e2211348119 (2022).
- [116] A. Srivastava, J. Hassan, and D. Homouz, *Nanomater.* **13**, 284 (2023).
- [117] F. -X. Coudert, F. Cailliez, R. Vuilleumier, A. H. Fuchs, and A. Boutin, *Faraday Discuss.* **141**, 377 (2009).
- [118] B. Zhou, A. Kobayashi, and H. Kobayashi, *Chem. Lett.* **42**, 1131 (2013).
- [119] F. -X. Coudert, A. Boutin, and A. H. Fuchs, *Commun. Chem.* **4**, 106 (2021).
- [120] E. S. A. Nouh, T. Liu, Z. L. Croft, and G. Liu, *ACS Mater. Lett.* **6**, 602 (2024).
- [121] Z. Zhang, X. Li, J. Yin, Y. Xu, W. Fei, M. Xue, Q. Wang, J. Zhou, and W. Guo, *Nat. Nanotechnol.* **13**, 1109 (2018).
- [122] J. Qian, X. Gao, and B. Pan, *Environ. Sci. Technol.* **54**, 8509 (2020).
- [123] Q. Lu, W. Shi, H. Yang, and X. Wang, *Adv. Mater.* 2001544 (2020).
- [124] J. -F. Olivieri, J. T. Hynes, and D. Laage, *J. Phys. Chem. Lett.* **12**, 4319 (2021).
- [125] T. Dufils, C. Schran, J. Chen, A. K. Geim, L. Fumagalli, and A. Michaelides, *Chem. Sci.* **15**, 516 (2024).

- [126] J. Chen, et al., *J. Am. Chem. Soc.* **145**, 19225 (2023).
- [127] I. Popov, et al., *Commun. Chem.* **6**, 77 (2023).
- [128] M. T. McDonnell and D. J. Keffer, *Micropor. Mesopor. Mat.* **177**, 17 (2013).
- [129] L. Zhang, et al., *Inorg. Chem. Front.* **10**, 7359 (2023).
- [130] Z. Fu, Y. Luo, J. Ma, and G. Wei, *J. Chem. Phys.* **134**, 154507 (2011).
- [131] Z. Qian, Z. Fu, and G. Wei, *J. Chem. Phys.* **140**, 154508 (2014).
- [132] Winarto, D. Takaiwa, E. Yamamoto, and K. Yasuoka, *J. Chem. Phys.* **142**, 124701 (2015).
- [133] M. Abbaspour, H. Akbarzadeh, S. Salemi, and L. Bahamanipour, *RCS Adv.* **11**, 10532 (2021).
- [134] C. Beduz, et al., *Proc. Natl. Acad. Sci. U.S.A.*, **109**, 12894 (2012).
- [135] B. P. Gorshunov, et al., *J. Phys. Chem. Lett.* **4**, 2015 (2013).
- [136] B. Meier, et al., *Nat. Commn.* **6**, 8112 (2015).
- [137] A. Kumar and P. Kumar, *Comput. Theor. Chem.* **1206**, 113493 (2021).
- [138] S. Du, Y. Hashikawa, H. Ito, K. Hashimoto, Y. Murata, Y. Hirayama, and K. Hirakawa, *Nano Lett.* **21**, 10346 (2021).
- [139] P. Delaney and J. C. Greer, *Appl. Phys. Lett.* **84**, 431 (2004).
- [140] M. Ya. Amusia and A. S. Baltenkov, *Phys. Lett. A* **360**, 294 (2006).
- [141] S. Jarvis, et al., *Commun. Chem.* **4**, 135 (2021).
- [142] B. Ensing, F. Costanzo, and P. L. Silvestrelli, *J. Phys. Chem. A* **116**, 12184 (2012).
- [143] S. Aoyagi, et al., *Meet. Abstr.* MA2014-01 1224 (2014).

-
- [144] E. Wang and Y. Gao, *J. Phys. Chem. A* **127**, 1190 (2023).
- [145] G.M. Sacha, A. Verdaguer, and M. Salmeron, *J. Phys. Chem. B* **110**, 14870 (2006).
- [146] M. Bartosik, et al., *J. Phys. Chem. B* **121**, 610 (2017).
- [147] B. I. Kim, R. D. Boehm, and H. Agrusa, *Langmuir*, **38**, 4538 (2022).
- [148] S.G. -Moñivas and J.J. Sáenz, *Phy. Rev. Lett.* **91**, 056101 (2003).
- [149] T. Cramer, F. Zerbetto, and R. Garcia, *Langmuir*, **24**, 6116 (2008).
- [150] M. Tokman, J. H. Lee, Z. A. Levine, M. -C. Ho, M. E. Colvin, and P. T. Vernier, *PLOS ONE*, **8**, e6111 (2013).
- [151] Z. Xie, S. Hao, W. Wang, J. Kou, and J. Fan, *J. Mol. Liq.* **363**, 119852 (2022).
- [152] A. Fujishima and K. Honda, *Nature*, **238**, 37 (1972).
- [153] T. Takata, et al., *Nature*, **581**, 411 (2020).
- [154] J. Luo, et al., *Science*, **345**, 1593 (2014).
- [155] Y. Jiang, S. Chen, W. Zheng, B. Zheng, and A. Pan, *Light sci. appl.* **10**, 72 (2021).
- [156] W. Li, Z. Yang, M. Sun, and J. Dong, *Rev. Phys.* **9**, 100077 (2022).
- [157] T. H. Ly, J. Zhao, H. Kim, G. H. Han, H. Nam, and Y. H. Lee, *Adv. Mater.* **28**, 7723 (2016).
- [158] Y. Zhao, et al., *Science*, **370**, 442 (2020).

Chapter2

Water Nano-Chains in Electric Fields[†]

Abstract

We examine structured water chains that have lengths in the sub-nanoscale range of 1.28-4.65 nm. We refer the structured water chains as those hydrogen-bonded networks of water molecules that have specific geometric patterns like ribbons or tapes stretched in a certain direction. An electric field is applied along the length of the chains to maintain the extended structures and prevent the water molecules from grouping together to form closed structures. Our calculations underscore the potential existence of such structured water nano-chains in the electrostatic environment, which we simulate in its simplicity by employing a dipolar, uniform and static electric field. Detailed analysis reveals that the most stable structured chains across a wide range of electric fields are those consisting of pentamer rings.

[†]Work presented in this chapter is based on a research article:
Structured Water Chains in External Electric Fields.
Smita Rai, Nayan Sharma, and Dhurba Rai, *Molecular Physics*, e1662957 (2019).

2.1 Background

Manipulating the fundamental properties of individual water molecules and clusters in the condensed phase is one of the most significant advances in recent molecular and nanoscale research on water [1]. Typically, water clusters manifest in closed structure forms with a distinct hydrogen bonding (H-bonding) network that arranges the water dipoles to have a net minimal electric dipole moment, not exceeding ~ 8 Debye even for those containing more than 40 water molecules [2, 3]. However, those that are restricted to nanochannels and those that are typically found in molecular frameworks, have elongated structures [4–9], and they play an important role in the stability of molecular frameworks [10]. Viewed from an alternative perspective, the water cluster adjusts its structure inside the channel or cavity environment while retaining the dominance of water-water interactions over confining wall-water interactions, which results in the formation of H-bonded structures spanning the nanoscopic length scales. Thus, it can be inferred that a cluster of water molecules adapts its structure defined by the geometry of the host channel or cavity.

Numerous experimental [11, 12] and computational studies [13] have shown that water confined in carbon nanotubes (CNTs) exhibit helical structures or chains of water-rings of various configurations (pentagonal, hexagonal, etc.). Furthermore, a number of investigations have found the presence of helical, linear, and stable water chains in metal-organic frameworks (MOFs) [14, 15]. Some exhibit highly structured networks that consist of cyclic tetramer [16, 17], pentamer [18–20], and hexamer chains [21–23], or combinations thereof [24, 25], giving rise to structures that resemble ribbons or tapes [16, 18–20, 23, 24, 26]. Additionally, there has been a clear and direct observation of water molecules self-assembling in a nanoscopic meniscus between the two hydrophilic surfaces in the air to form structures resembling chains [27]. This clearly suggests that the structures that

are normally unstable become energetically stable when they are contained in a nanoscopic environment.

In the hope of understanding and exploiting some of the peculiar characteristics of water in confinement for technological applications, confined water has been the subject of extensive experimental and theoretical studies [28–30]. These include, among others, fast proton transfer through the water chain inside carbon nanotubes (CNTs) [31–35], low diffusivity while high viscosity for flow through hydrophobic nanopores [36], high permeability [37] and unusually low dielectric constant [38–40]. Studies using molecular dynamics simulations reveal that the confined water exhibits a variety of ice phases [41–44], including the ferroelectric phase (all water dipoles oriented in one direction) [45, 46] and crystalline ice at room temperature [47], both of which are not known to exist in the bulk. It would be crucial to comprehend the behavioral characteristics of confined water in relation to the various phase structures for nanofluidic devices where manipulation of characteristic features may be advantageous.

Water behavior changes significantly at the molecular or nanoscopic scale due to the distinct and characteristic configurations of the H-bondings. It would be interesting to investigate how H-bondings in nanoconfined water are disrupted by the rearrangement of water dipoles under the influence of an electric field. Studies based on molecular dynamics simulations have shown that water within a carbon nanotube (CNT) undergoes structural change from liquid to solid (ice) phase and from a solid to another solid phase when exposed to external electric field [48–52]. It is also found that at increasing field strengths, reorientation of water dipoles in the confined H-bonded network causes a phase shift from a low-density to a high-density phase [53]. Furthermore, it is demonstrated that the applied field accelerates the translational diffusion of water molecules through nanopores due to the breaking up of H-bondings [54]. One crucial aspect to take into account is how the arrangement of water molecules in a field influences the flow of water in nanochannels or CNTs. This holds great significance for future nanofluidic devices,

including molecular cyclotrons based on electric field-induced water flow inside a carbon nanotorus [55].

It is known that confinement renders the H-bonded networks to lengthen along the channel lengths, resulting in elongated water structures that often manifest as tape- or ribbon-like structures [16, 18–20, 23, 24, 26]. Also, the confined water is shown to influence the transport properties of guest molecules in narrow pores [56]. In general, the confined water may also affect the thermal and electrical conductivity of the host systems. Thus, it would be crucial to investigate how the structured and elongated H-bonded network of water molecules evolves in an electric field since this could provide some insights into how the electric field controls water transport through the nano-channels [57, 58] and CNTs [59, 60], which may be useful in the design of nanofluidic devices [61] and nanowater pumps [62–65]. Also, in a molecular junction setup, it is found that H-bonds offer stronger electron conduction than covalent bonds [66]. This has attracted significant attention in understanding electron conduction through water chains due to its potential implications in molecular electronics [67, 68].

2.2 Scope of the Work

In this chapter, we will explore the characteristic way the structured water chains respond to the applied electric field within the density functional theory description using various exchange-correlation functionals, including those deemed suitable for systems with non-covalent interactions and medium or long-range dispersion interactions. The structured water chains are apparently periodic, with basic repeating units consisting of 4-, 5-, or 6-membered ring water clusters that share water molecules at the corners or those on the edges. They form elongated structures with a twisted tape- or ribbon-like appearance, however, they are unstable when left alone or in the absence of an electric field. Such structures manifest naturally in the supramolecular metal-organic frameworks.

In recent years, a great deal of research work has been devoted to the field-induced structural transition of small water clusters [69–74], particularly those contained inside carbon nanotubes (CNTs) [49, 51, 75]. However, there hasn't been much focus on using the observed field effects practically, and there aren't many studies in this area. This is where we aim to stimulate more interest in light of the recent advances in water-based devices and electronics [55, 76–80]. An important characteristic of extended structures is their significant electric dipole moment, which can be further increased by field application due to enhanced mutual polarization and water dipoles' alignment along the field direction. The large electric dipole moment of the structured water chains could be exploited in the dipole-based functionalized devices as its strength and orientation can easily be manipulated by a suitable bias voltage in the device setup. Furthermore, field variation of the energy difference between the highest occupied molecular orbital (HOMO) and lowest unoccupied molecular orbital (LUMO), i.e., the HOMO-LUMO (HL) gap and the way the frontier orbitals are filled, adapted or evolved in the field determine not only the stability of the structures but also their properties for specific applications. Specifically, field tuning of the HL gap in the relevant operational range (0.5 to 3 eV) would be particularly appealing for optoelectronic device applications.

We examine how the electric fields affect the structured water nano-chains and how their characteristic features evolve in the field. This could offer new functionalities to the emerging water-based devices [55, 76–80]. Also, the study potentially offers a good opportunity to understand the formation and stability of floating water-bridge between the water reservoirs maintained at a high potential difference ~ 15 kV or more [81, 82]. One may conceptualize this type of water bridge as the bulk equivalent of field-induced nano-size water bridges [83–87]. Furthermore, the study may provide valuable insights into a number of key topics, including understanding electric field control of bulk water permeation through materials [88], biological systems [89], and elucidating bulk behavior of water in the presence of fields.

In an effort to provide important insights into some of the appealing objectives, we perform herein the density functional calculations to examine the structure, energetics and stability of the structured H-bonded networks in the external electric field. Any attributes of significance for device applications will be analyzed and discussed. However, our results are limited to the given situations where such calculations in the presence of the external field can be justified. We now present the computational details of the works presented in this chapter.

2.3 Computational Methodology

We investigate the existence and characteristic evolution of the structured water chains in a field by using uniform and static fields, such as those found between parallel metallic plates that are oppositely charged. In practice, ice-film nanocapacitor setup is an effective and suitable means of applying uniform and static electric field in the molecular systems [90, 91]. To begin with, we first optimize the chain structures within the Gaussian 16 suite of programs (GAUSSIAN) [92] in the presence of relatively small electric fields, just sufficient to maintain their structures elongated, as the water molecules in the chain would otherwise cluster up to form arbitrary closed structures. For this purpose, we use the widely implemented B3LYP exchange-correlation functional [93, 94] with a decent Pople-type split valence and polarized basis set [95, 96], viz., 6-311++G(d,p) for both geometry optimization and geometry calculations. This basis set adds one *d*-function to oxygen atoms and one *p*-function to hydrogen atoms, which is necessary when the orbitals potentially change their shape in response to the applied electric field [94]. Additionally, since the chain structures are extended on the nanoscopic scale, we use two other functionals, viz., ω B97X-D [97] and M06-2X [98], which are appropriate for characterizing non-covalent and medium and/or long-range dispersion interactions. The calculated results are compared with the results obtained with the B3LYP functional for the pentamer chain structures.

The applied electric field is increased gradually in steps of 0.0001 a.u. (i.e., 5.14 mV/Å) along the permanent electric dipole moment of the structures in the lower field range (< 0.0020 a.u.). The field step size is then increased to 0.0005 a.u. Each chain structure under consideration is examined in terms of its structural evolution and other characteristics by carrying out full optimization of the geometry in the presence of the applied field and guaranteeing local-minimum stationary-state structure on its potential energy surface (PES) [99, 100]. In order to achieve this latter objective, and to examine the effect of the field on the vibrational spectrum, vibrational frequencies are calculated for each optimized structure in the field. The local minimum configurations were confirmed by the fact that all of the computed vibrational frequencies in the presence of the applied field unless otherwise stated, were real. Crucially, when it comes to the maximum field application, the field is applied until the water dipoles' preferential reorientation along the applied field direction results in considerable H-bond breaking and the geometry optimization fails repeatedly.

Our analysis focuses on fields in the range (0.0005-0.0220 a.u.), or roughly (26 mV/Å-1.13 V/Å), thus avoiding numerically large fields that otherwise could potentially break the chain structures. However, the chain structures are not feasible at fields lower than ~ 0.0005 a.u. In practice, fields in this range are typically present in the vicinity of nanotips [101], or at the apex of nanotips in scanning tunnelling microscopy (STM) [102, 103], and atomic force microscopy (AFM) [104–106].

2.4 Computed Results and Discussion

We now present results on the structural evolution of the nano-chain structures under consideration, as determined by full geometry optimization and frequency calculations in the presence of electric fields. Wherever feasible, the results that are compatible, or at the very least have similarities, with those found in the

literature will be compared or contrasted, while the results that are indicative of potential device applications will be discussed.

2.4.1 Single-file Water Chain

Numerous studies have considered single-file of water molecules forming a linear water chain as stable structures [107–109], nevertheless, the putative global minimum-energy structures are rather cyclic ring or closed structures, most of which are the fused-ring structures [110, 111]. The single-file water chain with water molecules arranged in zigzag and helical H-bonding structure is shown in Fig. 2.1. Such water chains are mostly studied in relation to proton conduction as

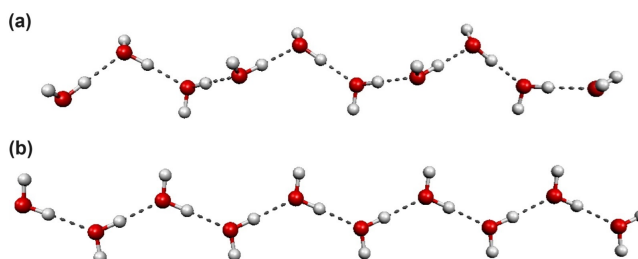


FIGURE 2.1: Representative single-file (a) helical and (b) zigzag water chain consisting of 10 water molecules each, optimized at the B3LYP/6-311++G(d,p) level of theory.

a fundamental proton wire in a free-form [112, 113] or inside CNTs or nanochannels [31, 114–118]. Calculations show that the helical structure is only marginally lower in energy than the zigzag structure, which becomes isoenergetic to within 1 kcal/mol on field application. Comparably, the helical structure exhibits a somewhat smaller dipole moment than the zigzag structure that is aligned along the length of the chain, yet when a field is present, they appear to be equivalent. Both of these structures have characteristics that are similar to the structured chains taken into consideration in this work when examined in the presence of a field. We now present such structured water chains in external fields and examine their evolution and in-field properties.

2.4.2 Tetramer Structured Water Chain

We consider tetramer water chains with a 4-membered tetramer water ring as its fundamental building unit. A notable feature of the tetramer structured water chains is that the basic building units, i.e. the tetramer rings, are alternately oriented perpendicular to each other giving them a twisted ribbon-like appearance. The smallest chain consisting of 3 units of corner-sharing water tetramer rings is composed of 10 water molecules, while the longest chain obtained by successive addition of five more such tetramer units has 25 water molecules. A collage of

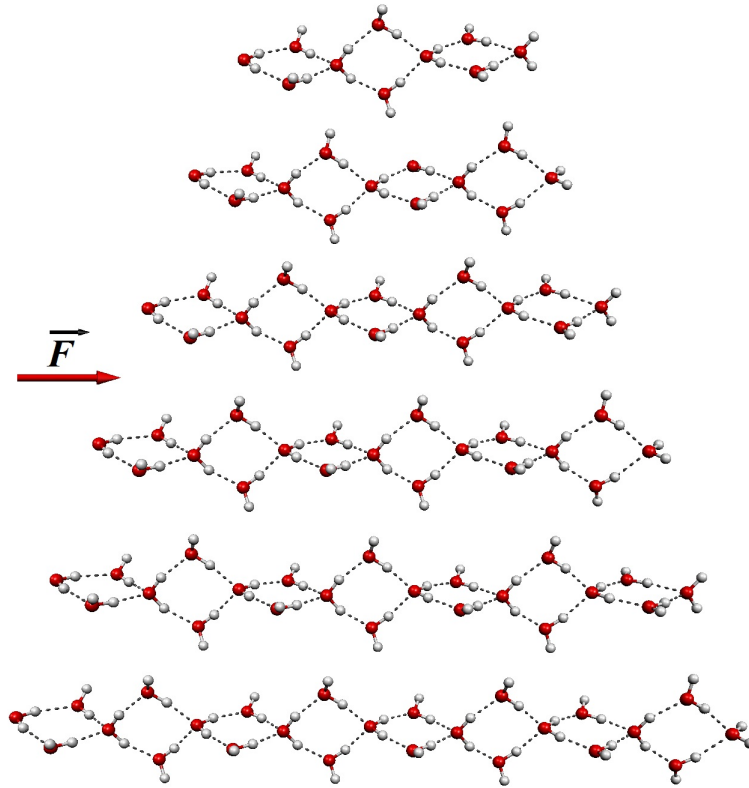


FIGURE 2.2: Water tetramer chain consisting of 3-8 units of corner-sharing water tetramer rings in the presence of an electric field in the range of 0.0005-0.020 a.u. The arrow indicates the direction of field \vec{F} applied along the length of the chains. The length of the chains (extreme O-O distance) for a minimum applied field is in the range of 1.28-3.32 nm.

such chain structures with 3-8 units of tetramer water chains having lengths in the range 1.28-3.32 nm, respectively, is shown in Fig. 2.2. Such structured water chains prefer to form closed structures in the absence of the field, therefore a small

minimum electric field must be applied along the length of the chain to support the extended structures as shown in the figure. It is noted that the required minimum field in question is marginally higher for shorter chains than for larger chains. Specifically, the shorter 3-4 unit chains require a minimum field of around 0.001 a.u. for maintaining elongated structures, while it is 0.0005 a.u., for the longer 5-8 unit chains. Furthermore, shorter chains are found to sustain a relatively stronger field than longer chains. It is observed that the 3-units tetramer structure can sustain an electric field as high as 0.020 a.u., whereas the 8-units structure sustains a field only up to 0.007 a.u. Beyond these characteristic maximum field strengths, the dipole-field interactions ($-\vec{\mu}_i \cdot \vec{F}$) become dominant over the inter-molecular interactions leading to the distortion of the chain structures due to the rupturing of already weakened H-bonds. For longer chains composed of several dipoles, the orientation of individual water dipoles along the field direction becomes so important that the dipole-field interactions overcome intermolecular interactions at a much lower field strength. As a result, the longer chains exist only in a limited range of electric fields, while shorter chains can exist in a larger range. For instance, 8-units chain exists in a narrow field range (0.005–0.070 a.u.), while 3-units chain exists in a wide range (0.001–0.020 a.u.). Thus, the shorter tetramer chains are more robust to the electric field influence.

2.4.3 Pentamer Structured Water Chain

The basic building units in the pentamer structured water chains are the 5-membered water pentamer rings, which when connected through shared edges form elongated structures that, as shown in Fig. 2.3, resemble a 1D array of open books or zigzag tape-like chain structures. In comparison to the respective tetramer units chain, each pentamer chain has an excess of one water molecule resulting in a minimum of 11 water molecules for 3 units and a maximum of 26 water molecules for 8 units chain. Similar to tetramer chains, the minimum field necessary to maintain the elongated chain structure is applied along the length of

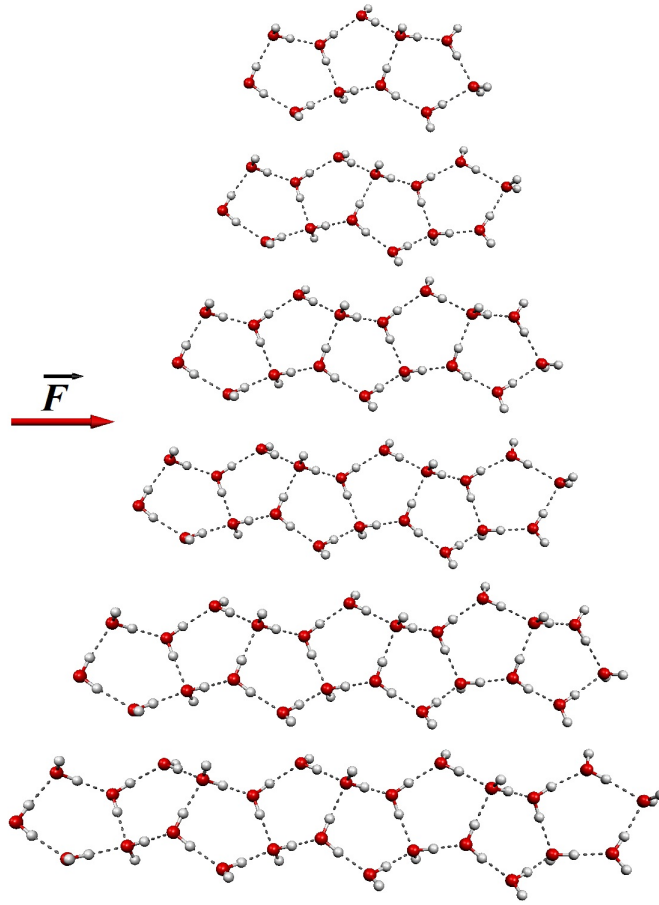


FIGURE 2.3: Water pentamer chain consisting of 3-8 units of edge-sharing water pentamer rings in the presence of a field in the range 0.0005-0.022 a.u. The arrow depicts the direction along which the field is applied. The length of the chains (extreme O-O distance) for a minimum applied field is in the range of 1.21-2.86 nm.

the chains, which is found to be higher for shorter chains (0.002 a.u. for 3 units) than for the longer chains (0.0005 a.u. for 8 units). For a minimum applied field, the chain lengths range from 1.21-2.86 nm for 3-8 units of chains, respectively. The shorter pentamer chain structures are more robust to external field influence as calculations reveal that the 3-unit pentamer chain structure can withstand an electric field as high as 0.022 a.u., while the longer 8-unit structure can sustain a field only up to 0.009 a.u. As discussed in the preceding section, when the field strength exceeds these characteristic maximum field strengths, the water dipoles compel themselves to get reoriented along the field direction, thereby rupturing

the H-bonds and resulting in the transformation of the chain structures into arbitrary net-like structures stretched along the field direction. Likewise, in the present instance as well, the longer chains are found to be susceptible to electric field influence with 8-units pentamer chain existing only in the narrow field range (0.0005–0.009 a.u.), whereas the 3-units pentamer chain exists in a wide range (0.002–0.022 a.u.). Furthermore, computations employing the dispersion corrected functionals, viz., ω B97X-D and M06-2X, reveal the same trend concerning the requirement of the minimum field to support the elongated structures and their characteristic field sustainability.

2.4.4 Hexamer Structured Water Chain

We now consider the hexamer water chains that are formed by the corner-sharing 6-membered water hexamer rings. Similar to tetramer chains, these 6-membered rings in the hexamer structured chains are oriented mutually perpendicular to each other resulting in a wrinkled ribbon-like appearance, as shown in Fig. 2.4. The 3-units of hexamer rings comprise of 16 water molecules, while the longest chain with 8 such units consists of 41 water molecules. The water hexamer chains exhibit characteristics similar to those of tetramer and pentamer chains. As before, the minimum field needed to maintain the open chain structure is higher for shorter chains than for longer ones, i.e. 0.003 a.u. for the shorter chains and 0.002 a.u. for the longer ones. In comparison to the tetramer and pentamer chains, due to the increased number of water molecules in the hexamer structured chains, they sustain a very narrow field range. It is observed that the maximum field strength that a 3-unit structure can withstand is just 0.014 a.u., whereas the corresponding pentamer and tetramer chains can withstand far larger field strengths. Due to the preferred reorientation of dipoles along the field direction, longer hexamer chains with a higher number of water dipoles are more susceptible to field-induced disruption. Consequently, a maximum field strength of 0.005 a.u. is found to be sustained by the 8-unit structure, which is significantly smaller

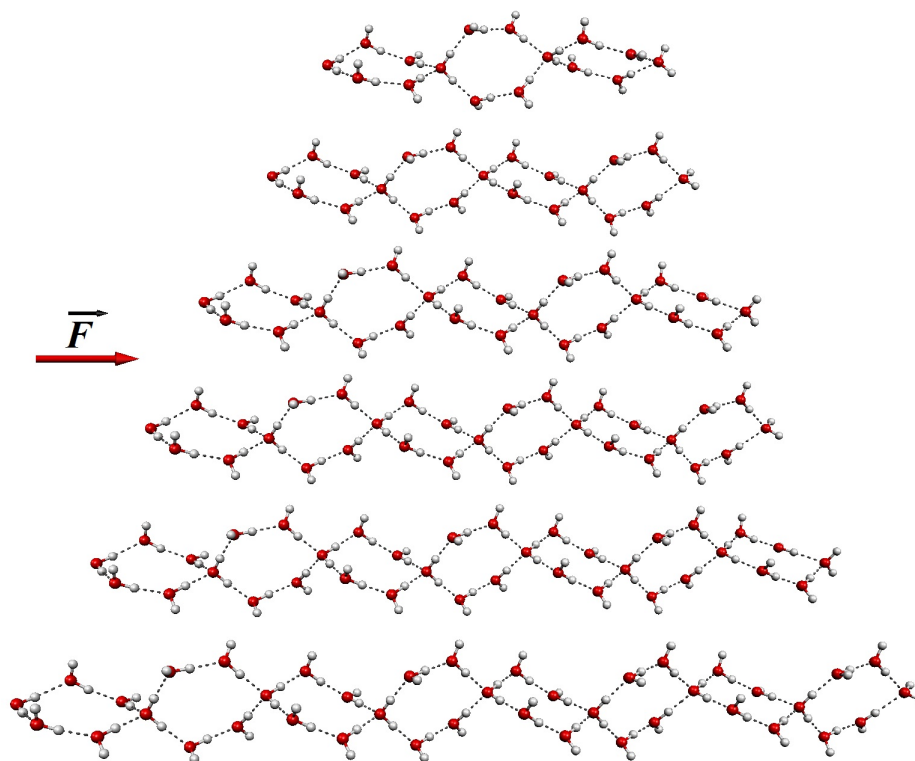


FIGURE 2.4: Water hexamer chains consisting of 3-8 units of the corner-sharing water hexamer rings in the presence of a field in the range 0.0002-0.014 a.u. applied along the length of the chains. The length of the chains (extreme O-O distance) for a minimum applied field is in the range of 1.87-4.63 nm.

than the corresponding maximum field strengths for 8-unit tetramer and pentamer chain structures. This shows that the shorter chains exist in a wide range of electric fields, such as (0.003–0.0140 a.u.) for a 3-unit structure, which suggests that they are more robust to the external field influence. The longer chains, which are susceptible to the field influence, manifest in a relatively small field range, i.e., (0.002–0.005 a.u.) for a 8-unit structure.

2.4.5 Average Hydrogen Bond Length and Dipole Moment

In a molecular assembly or cluster, such as those formed by water molecules, inter-molecular H-bonding plays a vital role in structural stability and energetics. Within such molecular systems, H-bonds are strengthened collectively due to the cooperativity effect, a crucial feature of the H-bonded systems. The associated

mutually influencing effects on each other can alter the physical and chemical properties of the system, including its stability, structure, and chemical activities. For the structures under study, this effect is reflected as the shortening of average H-bond length with an increase in chain length. Furthermore, it is found that the average H-bond length of the structures decreases almost linearly with the increase in the field strength. In a tetramer chain, the average H-bond length at a field strength of 0.001 a.u. range from 1.906 Å for 3-units to 1.836 Å for 8-units, which correspondingly reduces to 1.881 Å and 1.802 Å, respectively, for a field strength of 0.005 a.u. Also, upon closer examination, it is noted that the longer chains exhibit a higher rate of decrease in the average H-bond length with the field, which is 0.816 Å/a.u. in 8-units against 0.710 Å/a.u. in 3-units. This increment in the rate can be attributed to the enhanced cooperativity in the structures as they grow larger.

In the case of pentamer chains with an additional water molecule compared to the corresponding units of tetramer chains, the average H-bond length is slightly shorter than that for the tetramer chains for a given field strength. For instance, the average H-bond length for 3–8 units of pentamer chain lies in the range (1.873–1.797 Å) for a field strength of 0.0050 a.u., which is smaller than that for tetramer chains at the similar field value. However, the longer pentamer chains exhibit a faster rate of decrease of average H-bond length with the field, which is 0.833 Å/a.u. for 8-units, while 0.616 Å/a.u. for 3-units. The hexamer chains have shorter average H-bond lengths than tetramer and pentamer chains, which range from 1.813 to 1.750 Å for a field strength of 0.005 a.u. The average H-bond length in the hexamer chains decreases with the field at a rate of 0.700 Å/a.u. to 0.770 Å/a.u. for 3 to 8 units, respectively. As can be seen, all of the structures under investigation have average H-bond lengths that fall between 1.5 and 2.2 Å. This range is typical for H-bonds that are noticeably stronger than the van der Waals interactions [119].

The structural arrangement of H-bonded water molecules plays a critical

role in determining the overall dipole moment of structures. The structured water chains, as described, have a high dipole moment primarily because of the orderly arrangement of water dipoles. As a result, the structure's total dipole moment is strengthened to a considerable value over ~ 20 –40 Debye. Furthermore, as shown in Fig. 2.5, the dipole moment of the structures increases almost linearly with an increase in the applied field strength. This distinctive feature of the structured water chains finds use in dipole-based molecular device applications [120]. It must

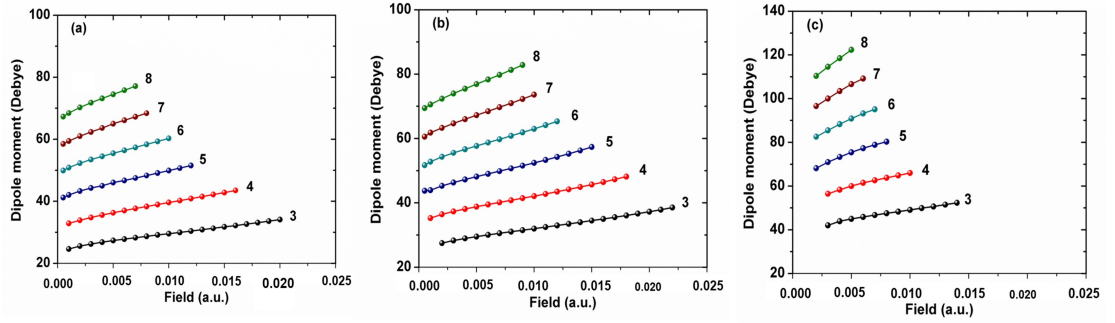


FIGURE 2.5: Field variation of dipole moment for (a) tetramer, (b) pentamer, and (c) hexamer structured water chain. The numerals 3–8 represent the number of constituent units in each chain.

be mentioned, however, that the observed linear variation breaks down when a strong electric field is applied. The system experiences a structural breakdown when the field intensity increases to the point where all of the dipoles are forced to align parallel to the field. Such a situation is marked by an abrupt increase in the total dipole moment of the system [69, 70, 121]. In conformity to an affirmative end, it is found that the dipole moment value, as determined from the dispersion interaction corrected ω B97X-D and M06-2X functionals for a given field, is within 0.5 Debye of the B3LYP value for each pentamer chain.

Another important aspect that is often examined in the molecular structures is the local dipole moment, which refers to the dipole moment for each constituent molecule within the structure. This is particularly important for understanding the molecular-scale distribution of charge and polarity inside the structure. The local dipole moment $\vec{\mu}_M$ is expressed as a sum of atomic charge displacements and atomic dipole moments, i.e., $\vec{\mu}_M = \sum_A (q_A \vec{R}_A + \vec{\mu}_A)$, where

\vec{R}_A denotes the position vector of each atomic centre from an arbitrary origin [122]. Here, the first term $q_A\vec{R}_A$ is origin dependent while the atomic dipole moment $\vec{\mu}_A$ is not, and the total dipole moment of the structure is precisely reproduced by the vector sum of the local dipole moment $\vec{\mu}_M$ of each water dipole. We determine the atomic charges (q_A) and dipole moments ($\vec{\mu}_A$) by employing the “Pop=AtomDipole” keyword available in the GAUSSIAN package. Using the least square fit approximation, this calculation scheme determines the atomic point charges and dipoles by the requirement to reproduce the molecular electrostatic potential at various points around the molecule. The calculated local dipole moments range from 1.65–3.22 Debye for the tetramer chains, 1.45–2.40 Debye for the pentamer chains, and 1.63–4.02 Debye for the hexamer chains. The observed variation of local dipole moment from the experimental value of 1.8 Debye for an isolated water molecule in the gas phase [123] is indicative of diverse local electric fields within the structures under consideration. As the structures grow in size,

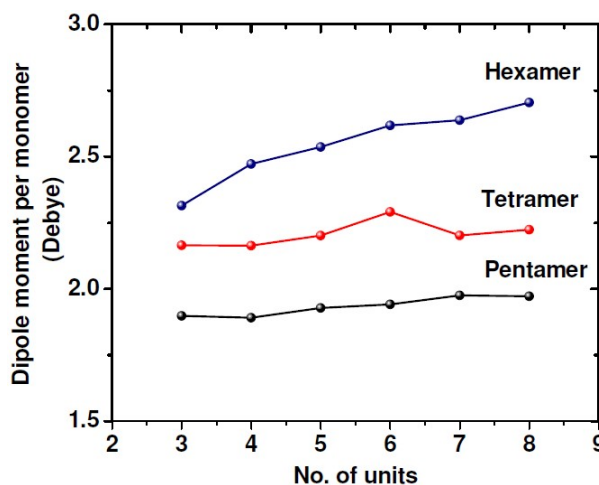


FIGURE 2.6: Variation of average dipole moment per water monomer as a function of structures’ size at a field strength of 0.005 a.u. for tetramer, pentamer and hexamer chains.

the interactions between water molecules cause them to become increasingly polarized, leading to a gradual increase in the average dipole moment per water molecule within the structure as illustrated in Fig. 2.6 for a field value of 0.005 a.u. Interestingly, it must be noticed that the average dipole moment per water molecule for each pentamer unit is minimal in comparison to its corresponding tetramer

and hexamer units, even though their net dipole moment values lie between that of tetramer and hexamer structures as shown in Fig. 2.5. This observation holds for other field values as well.

2.4.6 Energetics, HL Gaps and Stability

The energetic stability of the structured water chains is examined on the basis of binding energy per molecule as a function of field strength and structures' size. It is observed that when structures grow in size and the field strength is increased, the total energy of the structures consistently becomes more negative, suggesting that the increased polarization in the structures is responsible for the enhancement of intermolecular interactions. We quantify the gain in energetic stability of the structures in terms of binding energy per molecule, which can be expressed as $E_B = (N_S E_M - E_S)/N_S$, where N_S is the total number of water molecules in the structure, while E_M is the energy of an isolated water monomer and E_S is the energy of the structure in a field. The binding energy per molecule is found to

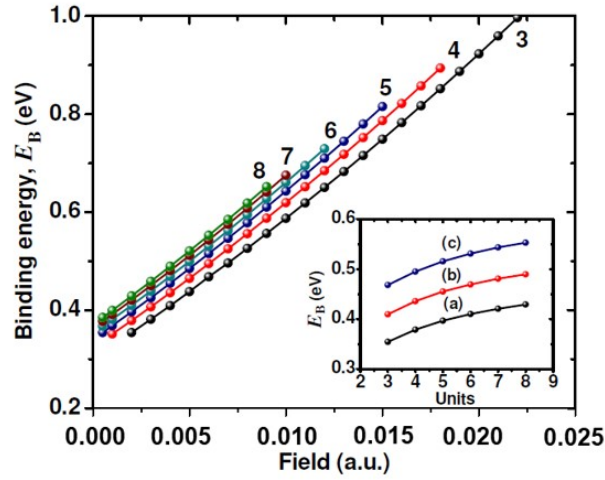


FIGURE 2.7: Binding energy per molecule (E_B) as a function of field for pentamer chains. E_B as a function of structures' size for field values, (a) 0.002, (b) 0.004 and (c) 0.006 a.u. are shown in the inset figure.

increase with the field strength for all structures under consideration. In Fig. 2.7, we show the rise in E_B with the increase in field strength for the pentamer chains,

while similar results hold for tetramer and hexamer chains. Additionally, for a given field value, the average binding energy rises with the structures' size and gradually saturates. This is shown in the inset figure for field strengths of 0.002, 0.004 and 0.006 a.u. for the pentamer chains. Also, we note that the binding energies computed employing the ω B97X-D and M06-2X functionals are within 0.1 eV of the B3LYP value, while the increase in structures' binding energy with the field is reproduced by both the functionals.

Furthermore, as the structures grow larger, the mutual polarization among the water molecules becomes more pronounced thereby strengthening the overall inter molecular interactions within the structure. The structures, thus, continuously gain energy during the growth process. Furthermore, in addition to the inherent mutual polarization within the structure, the field-induced polarization of the molecules further enhances the inter-molecular interactions, leading to structures that are energetically more favorable at higher field strengths. At this juncture, it is important to note that while the structures grow more energetically favorable as the field strength increases, their structural stability is not always correlated with their energetic stability. As previously mentioned, although having relatively lower energy values, at large field values the dipole-field interactions override the intermolecular interactions that lead to the structural breakdown of the chain structures.

Next, to examine the chemical stability of the linear chain structures under consideration, we compute the HL energy gap, E_g . Since E_g gives a measure of the energy required for an electronic excitation from HOMO to LUMO, a large E_g is typically associated with high electronic stability, thereby allowing the structures to survive in a wide range of chemical environments. The structures optimized at minimal field values previously specified to sustain their elongated structures have E_g values in the range (4.74-4.27 eV), (4.98-3.69 eV), and (6.12-6.20 eV) for 3 to 8 units of the tetramer, pentamer and hexamer chains, respectively. On further increase in the field strength, the E_g value is found to increase and

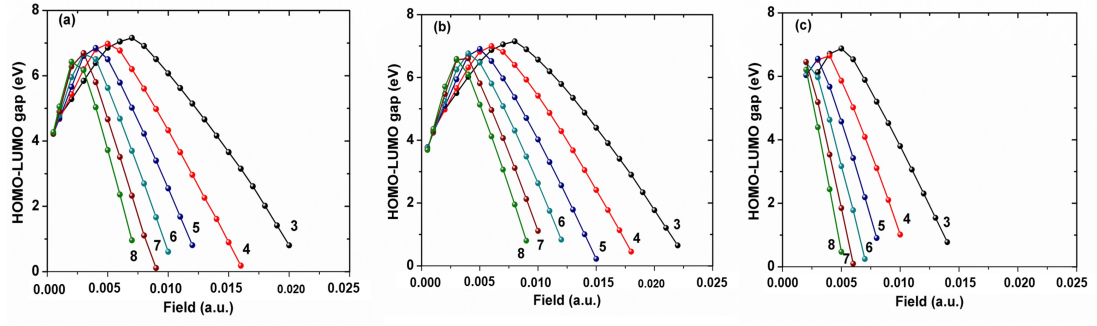


FIGURE 2.8: Variation of HL energy gap (E_g) as a function of electric field in the (a) tetramer, (b) pentamer, and (c) hexamer chains.

reaches its maximum value at a threshold field F_{th} , beyond which it decreases. This is shown in Fig. 2.8 for 3-8 units of the tetramer, pentamer and hexamer chains. Specifically, the optoelectronic device applications would benefit greatly from the structured water chains considering the ability to tailor the HL gap by an applied field to the necessary operating range (0.5 to 3 eV).

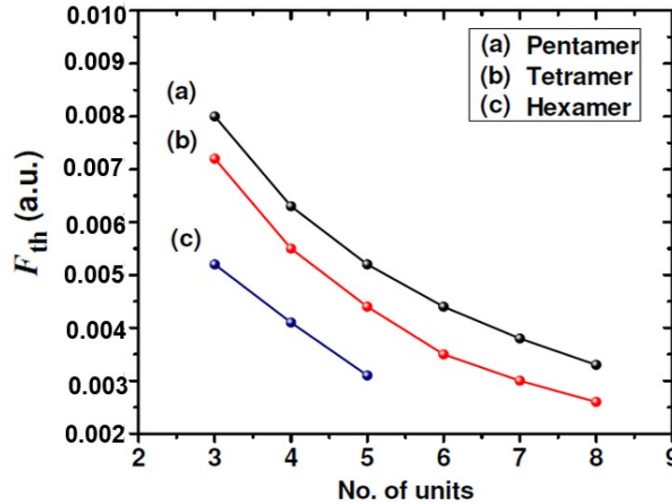


FIGURE 2.9: Threshold field (F_{th}) as a function of structures' size for the (a) tetramer, (b) pentamer and (c) hexamer chains.

We also examine the threshold field values for the structures considered in the work, since higher threshold field values are indicative of the chemical inertness of structures over a wide range of field strengths. As can be seen in Fig. 2.9, each unit of the pentamer chain under consideration has a higher threshold field value

than its corresponding tetramer and hexamer counterparts. Calculations using the ω B97X-D and M06-2X functionals have likewise shown the initial increase in E_g value with field and its subsequent fall beyond the threshold field value, however, the calculated energy gap value is marginally larger than the B3LYP values.

Taking into account the evolutionary trend of the energy gap in the field, we examined the field-induced redistribution of the frontier molecular orbitals [124] for the 5-units of pentamer chain at field values ranging from 0.001 to 0.010 a.u. As illustrated in Fig. 2.10, on field application, the LUMO swiftly migrates in the direction of the field, leading to its prompt localization towards one end of the structure, and thus the LUMO energy increases. When the LUMO gets closer

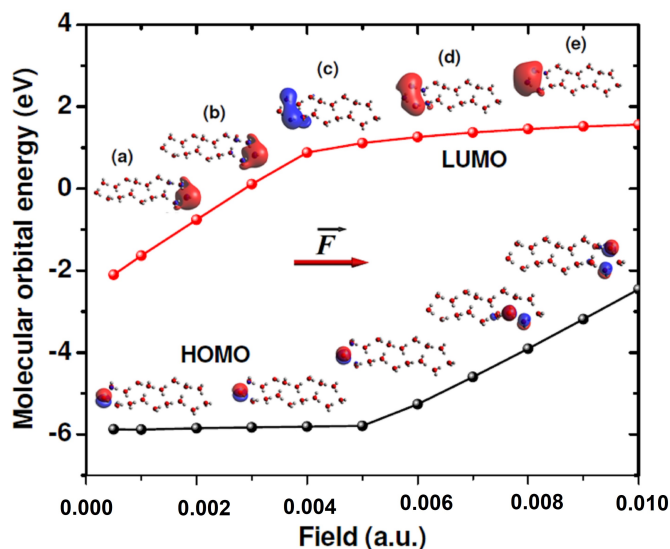


FIGURE 2.10: Evolution of the HOMO and LUMO energies in the 5-units of pentamer chain for field applied in the range (0.010–0.100 a.u.). Shown are the HOMO and LUMO for field strengths, (a) 0.010, (b) 0.030, (c) 0.052, (d) 0.070, and (e) 0.100 a.u. Molecular orbitals are drawn at the contour value ± 0.02 . The arrow indicates the direction of the applied field.

to the other end, where it is slowly localized, the localization causes the LUMO energy to gradually grow at high field strengths. On the other hand, the HOMO is relatively unaffected until a field value of 0.0052 a.u. (threshold field), at which point it migrates away from the field towards the other end of the structure and becomes localized, which leads to an increase in the HOMO energy. This field-induced variation of the molecular orbital energies results in a generally observed

trend for the HL gap, i.e., the initial increase followed by an eventual decrease beyond the threshold field value. For the structures under consideration, this observed modulation of the HL gap by an applied electric field may be useful for regulating electrical properties, particularly the electronic conductivity.

We note in passing that the overall evolutionary trends of the average binding energy (cf. Fig. 2.7) and the HL energy gap (cf. Fig. 2.8) with the electric field do not suggest any strong correlation between the energetic and chemical stabilities of the structures considered in this work. We observe a monotonic increase in the average binding energy of the structures, whereas the HL energy gap exhibits a decrease after reaching its maximum value at the threshold field value. A closer look, however, reveals an inverse relation between the average dipole moment per monomer and the HL energy gap of the structures. Each unit of pentamer chain structures has the lowest average dipole moment per water molecule (cf. Fig. 2.6), however, the threshold field is the highest (cf. Fig. 2.9), followed by that for the tetramer and hexamer structures. This suggests that the pentamer chains are the most favorable structures over others, thereby further supporting the experimental observation of nucleation of water pentagon chains on the Cu substrate [125].

2.5 Summary and Concluding Remarks

In summary, the ribbon- or tape-like nano-chain structures of water molecules, otherwise unstable in isolation can manifest in an electrostatic environment, which we simulate employing a small static and uniform electric field. The minimum field in the range of (0.0005-0.0030 a.u.) is applied along the chain's length to support the extended chain formations over a nanoscopic length. The geometry optimization along with subsequent vibrational frequencies calculations at each applied field value for all vibrational frequencies that are real suggests that the structures are local minima on their potential energy surface.

On examining the chain structures with increasing field strength, the shorter chain structures are found to sustain relatively stronger electric fields than the longer chains. The longer chains, consisting of multiple dipoles tending to align along the field direction are more susceptible to field influence due to enhanced dipole-field interactions that quickly overcome the intermolecular interactions, resulting in the weakening of H-bonds that lead to potential disruption of the chain structures. Calculations reveal the average dipole moment per water molecule to be minimum for the pentamer chain structures. Also, the threshold field marking the onset of the field-induced closure of the HL energy gap is found to be the highest in the case of pentamer chains, followed by the tetramer and hexamer chains. With the least average dipole moment and large threshold field value, the pentamer chains can be considered to be the most stable structures. When the electric field is increased, the average binding energy increases monotonically, but the HL energy gap shows an initial increase and then a possible closure after reaching a maximum opening at the threshold field value. The average binding energy and the HL energy gap as a function of the field show that there is no apparent correlation between the energetic and chemical stabilities of the structures that are being studied in this work.

The results presented in this chapter can have significant implications for device applications that exploit the structural behaviors and the associated properties of the structured water clusters [126]. An important property that can be exploited in the dipole-based functionalised devices [120, 127, 128] is the large electric dipole moment value (~ 20 -130) Debye for the structured water nano-chains within the field range considered in the work. The strength of the dipole moment and its orientation can be suitably manipulated by a bias voltage in a setup for device applications [129, 130]. We hope that this work will stimulate experimental studies on the structured water nano-chains.

References

- [1] J. Hu and Z. Cao, *Natl. Sci. Rev.* **1**, 180 (2014).
- [2] J. G. -Constantin, M. A. Carignano, I. Szleifer, E. J. Marceca, and H. R. Corti, *J. Chem. Phys.* **133**, 024506 (2010).
- [3] I. Bako and I. Mayer, *J. Phys Chem. A* **120**, 4408 (2016).
- [4] S. Zhang, Y. Su, C. Duan, Y. Li, H. Zhu, and Q. Meng, *Chem. Commun.* **2006**, 4997 (2006).
- [5] Y. -G. Huang, Y. -Q. Gong, F. -L. Jiang, D. -Q. Yuan, M.-Y. Wu, Q. Gao, W. Wei, and M. -C. Hong, *Cryst. Growth. Des.* **7**, 1385 (2007).
- [6] R. Natarajan, J. P. H. Charmant, A. G. Orpen, and A. P Davis, *Angew. Chem. Int. Ed.* **49**, 5125 (2010).
- [7] H. -X. Zhao, X. -J. Kong, H. Li, Y. -C. Jin, L. -S. Long, X. C. Zeng, R. -B. Huang, and L. -S. Zheng, *Proc. Natl. Acad. Sci. U.S.A.* **108**, 3481 (2011).
- [8] K. H. Wang, M. C. Zhu, L. Liu, E. J. Gao, D. Y. Hou, G. Xin, and T. C. Li, *Russ. J. Coord. Chem.* **38**, 29 (2012).
- [9] B. Zhou, A. Kobayashi, and H. Kobayashi, *Chem. Lett.* **42**, 1131 (2013).
- [10] Y. Jin, Y. X. Che, and J. M. Zheng, *Inorganica Chim. Acta* **361**, 2799 (2008).
- [11] O. Byl, J. -C. Liu, Y. Wang, W. -L. Yim, J. K. Johnson, and J. T. Yates, Jr. *J. Am. Chem. Soc.* **128**, 12090 (2006).
- [12] S. D. Bernandina, E. Paineau, J. -B. Brubach, P. Judeinstein, S. Rouzière, P. Launois, and P. Roy, *J. Am. Chem. Soc.* **138**, 10437 (2016).
- [13] A. Chatzichristos and J. Hassan, *Nanomater.* **12**, 174 (2022).

- [14] C. Biswas, M.G.B. Drew, and A. Ghosh, *Inorg. Chem.* **47**, 4513 (2008).
- [15] F. Yu and B. Li, *Mol. Cryst. Liq. Cryst.* **625**, 253 (2016).
- [16] B.-H. Ye, A.-P. Sun, T.-F. Wu, Y.-Q. Weng, and X.-M. Chen, *Eur. J. Inorg. Chem.* **2005**, 1230 (2005).
- [17] S.R. Choudhury, A.D. Jana, E. Colacio, H.M. Lee, G. Mostafa, and S. Mukhopadhyay, *Cryst. Growth Des.* **7**, 212 (2007).
- [18] B.-Q. Ma, H.-L. Sun and S. Gao, *Chem. Commun.* **2220** (2004).
- [19] J. P. Naskar, M. G. B. Drew, A. Hulme, D.A. Tocher, and D. Datta, *Cryst. Eng. Comm.* **7**, 67 (2005).
- [20] D. Sun, H.-R. Xu, C.-F. Yang, Z.-H. Wei, N. Zhang, R.-B. Huang, and L.-S. Zheng, *Cryst. Growth Des.* **10**, 4642 (2010).
- [21] S.K. Ghosh and P.K. Bharadwaj, *Eur. J. Inorg. Chem.* **2005**, 4880 (2005).
- [22] R.L. García, B.M.D. Murillo, V. Barba, H. Höpfl, H.I. Beltrán, and L.S.Z. Rivera, *Chem. Commun.* **5527** (2005).
- [23] X.-M. Zhang, R.-Q. Fang, and H.-S. Wu, *Cryst. Growth Des.* **5**, 1335 (2005).
- [24] L. Cheng, J.-B. Lin, J.-Z. Gong, A.-P. Sun, B.-H. Ye, and X.-M. Chen, *Cryst. Growth Des.* **6**, 2739 (2006).
- [25] R. P. Sharma, A. Singh, P. Venugopalan, P. Brandão, and V. Félix, *Polyhedron* **40**, 175 (2015).
- [26] L. Infantes and S. Motherwell, *Cryst. Eng. Comm.* **4**, 454 (2002).
- [27] B. I. Kim, R. D. Boehm, and J. R. Bonander, *J. Chem. Phys.* **139**, 054701 (2013).

- [28] S. Chakraborty, H. Kumar, C. Dasgupta, and P. K. Maiti, *Acc. Chem. Res.* **50**, 2139 (2017).
- [29] D. Wang, Y. Tian, and L. Jiang, *Small*, **17**, 2100788 (2021).
- [30] H. R. Corti, et al., *Eur. Phys. J. E* **44**, 136 (2021).
- [31] C. Dellago, M.M. Naor, and G. Hummer, *Phys. Rev. Lett.* **90**, 105902 (2003).
- [32] Z. Cao, Y. Peng, T. Yan, S. Li, A. Li, and G.A. Voth, *J. Am. Chem. Soc.* **132**, 11395 (2010).
- [33] I. A. Ryzhkin, M. I. Ryzhkin, A. M. Kashin, E. A. Galitskaya, and V. V. Sinitsyn, *EPL*, **126**, 36003 (2019).
- [34] K. -ichi Otake, et al., *Nat. Commun.* **11**, 843 (2020).
- [35] S. Kang, et al., *Chem. Mater.* **34**, 3967 (2022).
- [36] Y. Liu, Q. Wang, and L. Lu, *Langmuir*, **20**, 6921 (2004).
- [37] R.H. Tunuguntla, R.Y. Henley, Y.-C. Yao, T.A. Pham, M. Wanunu, and A. Noy, *Science*, **357**, 792 (2017).
- [38] L. Fumagalli, A. Esfandiar, R. Fabregas, S. Hu, P. Ares, A. Janardanan, Q. Yang, B. Radha, T. Taniguchi, K. Watanabe, G. Gomila, K. Novoselov and A. Geim, *Science*, **360**, 1339 (2018).
- [39] C. Zhang, *J. Chem. Phys.* **148**, 156101 (2018).
- [40] H. Zhu, F. Yang, Y. Zhu, A. Li, W. He, J. Huang, and G. Li, *RCS Adv.* **10**, 8628 (2020).
- [41] K. Koga, G.T. Gao, H. Tanaka, and X.C. Zeng, *Nature*, **412**, 802 (2001).
- [42] J. Bai, J. Wang, and X.C. Zeng, *Proc. Natl. Acad. Sci. U.S.A.* **103**, 19664 (2006).

- [43] D. Takaiwa, I. Hatano, K. Koga, and H. Tanaka, *Proc. Natl. Acad. Sci. U.S.A.* **105**, 39 (2008).
- [44] S. Li and B. Schmidt, *Phys. Chem. Chem. Phys.* **17**, 7303 (2015).
- [45] C. Luo, W. Fa, J. Zhou, J. Dong, and X.C. Zeng, *Nano Lett.* **8**, 2607 (2008).
- [46] W.-H. Zhao, J. Bai, L.-F. Yuan, J. Yang, and X.C. Zeng, *Chem. Sci.* **5**, 1757 (2014).
- [47] K. B. Jinesh and J. W. M. Frenken, *Phys. Rev. Lett.* **101**, 036101 (2008).
- [48] Z. Fu, Y. Luo, J. Ma, and G. Wei, *J. Chem. Phys.* **134**, 154507 (2011).
- [49] Z. Qian, Z. Fu, and G. Wei, *J. Chem. Phys.* **140**, 154508 (2014).
- [50] Y. He, G. Sun, K. Koga, and L. Xu, *Sci. Rep.* **4**, 6596 (2014).
- [51] Winarto, D. Takaiwa, E. Yamamoto, and K. Yasuoka, *J. Chem. Phys.* **142**, 124701 (2015).
- [52] Winarto, E. Yamamoto, and K. Yasuoka, *Water*, **9**, 473 (2017).
- [53] J.L. England, S. Park, and V.S. Pande, *J. Chem. Phys.* **128**, 044503 (2008).
- [54] S.O. Diallo, E. Mamontov, W. Nobuo, S. Inagaki, and Y. Fukushima, *Phys. Rev. E* **86**, 021506 (2012).
- [55] H. Sabzyan and M. Kowsar, *Phys. Chem. Chem. Phys.* **19**, 12384 (2017).
- [56] A. Phan, D. R. Cole, R. G. Weiß, J. Dzubiella, and A. Striolo, *ACS Nano* **10**, 7646 (2016).
- [57] K. Xiao, Y. Zhou, X. -Y. Kong, G. Xie, P. Li, Z. Zhang, L. Wen, and L. Jiang, *ACS Nano*, **10**, 9703 (2016).
- [58] A. T. Celebi, M. Barisik, and A. Beskok, *J. Chem. Phys.* **147**, 164311 (2017).

- [59] J. Su, and H. Guo, *ACS Nano* **5**, 351 (2011).
- [60] K. Ritos, M. K. Borg, N. J. Mottram, and J. M. Reese, *Phil. Trans. R. Soc. A* **374**, 2060 (2016).
- [61] D. Cao, P. Pang, J. He, T. Luo, J. H. Park, P. Krstic, C. Nuckolls, J. Tang, and S. Lindsay, *ACS Nano* **5**, 3113 (2011).
- [62] X. -P. Li, G. -P. Kong, X. Zhang, and G. -W. He, *Appl. Phys. Lett.* **103**, 143117 (2013).
- [63] S.D. Luca, B. D. Todd, J. S. Hansen, and P. J. Daivis, *J. Chem. Phys.* **138**, 154712 (2013).
- [64] A. B. Farimani, M. Heiranian, and N. R. Aluru, *Sci. Rep.* **6**, 26211 (2016).
- [65] Y. Xu, J. Xu, H. Liu, and C. Yang, *Chem. Eng. Sci.* **267**, 118325 (2023).
- [66] T. Nishino, N. Hayashi, and P.T. Bui, *J. Am. Chem. Soc.* **135**, 4592 (2013).
- [67] R. Fukuzumi, S. Kaneko, S. Fujii, T. Nishino, and M. Kiguchi, *J. Am. Chem. Soc.* **122**, 4698 (2018).
- [68] L. Xiang, et al., *Matter*, **3**, 166 (2020).
- [69] D. Rai, A. D. Kulkarni, S.P. Gejji, and R. K. Pathak, *J. Chem. Phys.* **135**, 024307 (2011).
- [70] D. Rai, A. D. Kulkarni, S.P. Gejji, L. J. Bartolotti, and R. K. Pathak, *J. Chem. Phys.* **138**, 044304 (2013).
- [71] L. J. Bartolotti, D. Rai, A. D. Kulkarni, S. P. Gejji, and R. K. Pathak, *Compt. Theor. Chem.* **1044**, 66 (2014).
- [72] Y. Bai, et al., *J. Phys. A* **119**, 2083 (2015).
- [73] N. D. Gurav, A. D. Kulkarni, S. P. Gejji, and R. K. Pathak, *J. Chem. Phys.* **142**, 214309 (2015).

- [74] N.D. Gurav, S. P. Gejji, L. J. Bartolotti, and R. K. Pathak, *J. Chem. Phys.* **145**, 074302 (2016).
- [75] P. Cao, D. Han, and C. Luo, *Mater. Res. Express*, **6**, 1250a1 (2019).
- [76] Z. G. Chiragwandi, O. Nur, M. Willander, and N. Calander, *App. Phys. Lett.* **85**, 5310 (2003).
- [77] R. E. Jacobsen, S. Arslanagic and A. V. Lavrinenko, *Appl. Phys. Rev.* **8**, 041304 (2021).
- [78] Y. Lu, et al., *Research (Wash DC)* 7505638 (2021).
- [79] A. Buchmann, C. Hoberg, and F. Novelli, *APL Photonics*, **7**, 121302 (2022).
- [80] S. Melnik, A. Ryzhov, A. Kiselev, A. Radenovic, T. Weil, K. J. Stevenson, and V. G. Artemov, *J. Phys. Chem. Lett.* **14**, 6572 (2023).
- [81] E. C. Fuchs, J. Woisetschlager, K. Gatterer, E. Maier, R. Pecnik, G. Holler, and H. Eisenkobl, *J. Phys. D: Appl. Phys.* **40**, 6112 (2007).
- [82] R.M. Namin, S.A. Lindi, A. Amjadi, N. Jafari, and P. Irajizad, *Phys. Rev. E* **88**, 033019 (2013).
- [83] S. G. -Moivas and J. J. Saenz, *Phy. Rev. Lett.* **91**, 056101 (2003).
- [84] H. Choe, M.-H. Hong, Y. Seo, K. Lee, G. Kim, Y. Cho, *J. Ihm, and W. Jhe*, *Phys. Rev. Lett.* **95**, 187801 (2005).
- [85] G. M. Sacha, A. Verdaguer, and M. Salmeron, *J. Phys. Chem. B* **110**, 14870 (2006).
- [86] T. Cramer, F. Zerbetto, and R. Garca, *Langmuir* **24**, 6116 (2008).
- [87] M. Lee, B. Sung, N. Hashemi, and W. Jhe, *Faraday Discuss.* **141**, 415 (2009).

- [88] C. Dai, M. Liao, X. Li, S. Chen, P. Gao, P. Sheng, *Phys. Rev. Research*, **4**, 033164 (2022).
- [89] M. Tokman, J. H. Lee, Z. A. Levine, M. -C. Ho, M. E. Colvin, and P. T. Vernier, *PLOS ONE*, **8**, e61111 (2013).
- [90] S. Shin, Y. Kim, E. -seong Moon, D. H. Lee, H. Kang, and H. Kang, *J. Chem. Phys.* **139**, 074201 (2013).
- [91] Y. Park, H. Kang, and H. Kang, *J. Phys. Chem. C* **124**, 1129 (2020).
- [92] M.J. Frisch, et al., Gaussian 16, Revision C.01 (Gaussian, Inc., Wallingford, CT, 2016).
- [93] A. D. Becke, *J. Phys. Chem.* **98**, 5648 (1993).
- [94] J. B. Foresman and Æ. Frisch, *Exploring Chemistry with Electronic Structure Methods*, 2nd ed., Gaussian, Inc. Pittsburgh, PA (1996).
- [95] W. J. Hehra, R. Ditchfield, and J. A. Pople, *J. Chem. Phys.* **56**, 2257 (1972).
- [96] V. A. Rassolov, J. A. Pople, M. A. Ratner, T. L. Windus, *J. Chem. Phys.* **109**, 1223 (1998).
- [97] J. -D. Chai and M. H. -Gordon, *Phys. Chem. Chem. Phys.* **18**, 6615 (2008).
- [98] Y. Zhao and D. G. Truhlar, *Theor. Chem. Acc.* **120**, 215 (2008).
- [99] D. G. Truhlar, in *The Encyclopedia of Physical Science and Technology*, 3rd ed., edited by R. A. Meyers, Academic Press, New York (2001).
- [100] E. G. Lewars, *Computational Chemistry*, Ch. 2, Springer Cham (2017).
- [101] S. -W. Cheng and H.-F. Cheung, *J. Appl. Phys.* **94**, 1190 (2003).
- [102] G. M. Shedd and P. E. Russell, *Nanotechnology*, **1**, 67 (1990).

- [103] S. Kondo, S. Heike, M. Lutwyche, and Y. Wada, *J. Appl. Phys.* **78**, 155 (1995).
- [104] Ph. Avouris, R. Martel, T. Hertel, and R. Sandstrom, *Appl. Phys. A* **66**, S659 (1998).
- [105] R. Nemutudi, N. J. Curson, N. J. Appleyard, D. A. Ritchie, and G. A. C. Jones, *Microelectron. Eng.* **57**, 967 (2001).
- [106] X. N. Xie, H. J. Chung, C. H. Sow, and A. T. S. Wee, *Mater. Sci. Eng. R* **54**, 1 (2006).
- [107] K. Hermansson and M. Alfredsson, *J. Chem. Phys.* **111**, 1993 (1999).
- [108] R. Parthasarathi, M. Elango, V. Subramanian, and N. Sathyamurthy, *J. Phys. Chem. A* **113**, 3744 (2009).
- [109] Y. I. Neela, A. S. Mahadevi, and G. N. Sastry, *J. Phys. Chem. B* **114**, 17162 (2010).
- [110] S. Maheshwary, N. Patel, N. Sathyamurthy, A. D. Kulkarni, and S. G. Gadre, *J. Phys. Chem. A* **105**, 10525 (2001).
- [111] A. Malloum, J. J. Fifen, Z. Dhaouadi, S. G. N. Engo, and J. Conradie, *New J. Chem.* **43**, 13020 (2019).
- [112] K. Drukker, S. W. de Leeuw, and S. H. -Schiffer, *J. Chem. Phys.* **108**, 6799 (1998).
- [113] M. L. Karahka and H. J. Kreuzer, *Biointerphases*, **8**, 13 (2013).
- [114] R. Pomès and B. Roux, *Biophys. J.*, **82**, 2304 (2002).
- [115] J. Köfinger, G. Hummera and C. Dellago, *Phys. Chem. Chem. Phys.* **13**, 15403 (2011).
- [116] S. Bera, S. Maity, and D. Haldar, *CrysEngComm.* **17**, 1569 (2015).

- [117] A. Horner and P. Pohl, *Faraday Discuss.* **209**, 9 (2018).
- [118] M. Druchok, V. Krasnov, T. Krokhmalskii, T. C. e Bufalo, S. M. de Souza, O. Rojas, and O. Derzhko, *J. Chem. Phys.* **158**, 104304 (2023).
- [119] G. R. Desiraju and T. Steiner, *The Weak Hydrogen Bond in Structural Chemistry and Biology* Oxford, New York (1999).
- [120] S. Tanimoto, M. Tsutsui, K. Yokota, and M. Taniguchi, *Nanoscale Horiz.* **1**, 399 (2016).
- [121] D. Rai, A. D. Kulkarni, S. P. Gejji, and R. K. Pathak, *J. Chem. Phys.* **128**, 034310 (2008).
- [122] R. F. W. Bader, A. Larouche, C. Gatti, M. T. Carroll, P. J. MacDougall, and K. B. Wilberg, *J. Chem. Phys.* **87**, 1142 (1987).
- [123] S. A. Clough, Y. Beers, G. P. Klein, P. Gerald and L.S. Rothman, *J. Chem. Phys.* **59**, 2254 (1973).
- [124] L. R. C. Wang, H. J. Kreuzer, and O. Nishikawa, *Org. Electron.* **7**, 99 (2006).
- [125] J. Carroasco, A. Michaelides, M. Forster, S. Haq, R. Raval, and A. Hodgson, *Nat. Mater.* **8**, 427 (2009).
- [126] J. Pan, K. -N. Zhu, M. Zhou, and Z. Y. Wang, *Systems, Man and Cybernetics* (IEEE International Conference, Washington, DC, 2003), pp. 5034-5039.
- [127] S. Kimura, *Org. Biomol. Chem.* **6**, 1143 (2008).
- [128] E. Velichko, T. Zezina, A. Cheremiskina, and O. Tsybin, *Nano Communication Device with Embedded Molecular Films: Effect of Electromagnetic Field and Dipole Moment Dynamics* (Springer, Cham, 2015), pp. 765-771.

- [129] Y. Chung, E. Verploegen, A. Vailionis, Y. Sun, Y. Nishi, B. Murmann, and Z. Bao, *Nano Lett.* **11**, 1161 (2011).
- [130] L. J. Martin, B. Akhavan, and M. M. M. Bilek, *Nat. Commun.* **9**, 357 (2018).

Chapter3

Water Nano-Rings in Electric Fields[†]

Abstract

We examine the structural evolution of nano-size water rings in an electric field, as well as their energetics and stability. The rings consist of 36, 72, and 108 water molecules that are formed out of a hydrogen-bonded network resembling a twisted ribbon with diameters of 1.54, 3.10, and 4.56 nm, respectively. The larger rings exhibit more sensitivity to the field influence, yet the ring structures are robust against the field applied perpendicular to the ring structures. Conversely, fields applied parallel to the ring quickly transform the ring structures into arbitrary ones, regardless of the size of the ring. The characteristic local modes of vibrational response of a ring to the applied fields are analyzed and identified in the infrared and Raman spectra. This provides a spectroscopic signature that may be used to determine the manifestation of such hydrogen-bonded ring networks. Our study highlights the significance of the nanoscale ring water structures, which have potential device applications.

[†]Work presented in this chapter is based on a research article:

Water Nano-Rings in Electric Fields.

Smita Rai, Dhurba Rai, and Vivekanand V. Gobrei, *Molecular Physics*, e2273977 (2023).

3.1 Background

As outlined in Chapter 2, confined water in nano space exhibits characteristics different from bulk water. The confining framework and the water molecules interact through van der Waals and other non-bonding interactions, while the hydrogen-bonding (H-bonding) interactions between the water molecules render the structure distinct and stable [1, 2]. The confining frameworks include hydrophobic nanocages, nanochannels, or metal-organic frameworks (MOFs). Within such confinement, the water structure exhibits planar [3], helical [4–6] and tape or ribbon-like topologies that either show uniformity in their structures [7–11] or coexist as a combination of different forms [12–14]. In addition to the helical, tape or ribbon-like water structures, the formation of nano-size ring structures out of water molecules is also investigated, where the structure is stabilized not only by H-bonds but also by coordination interactions with metal atoms [15]. The H-bonded macrocycles form another class of ring structures that can be self-assembled into organic materials by rationally ordering molecules at the nanoscale, thereby creating molecular nanostructured systems with potential uses ranging from nanoporous and nanochannel molecular networks to functional devices for optoelectronic applications [16].

In molecular- or nano-electronics, the study of ring structures is especially crucial for the potential control of electron conduction through the ring structures by the application of a magnetic field [17, 18], which also has the benefit of directed electron transport [19]. Understanding how the external magnetic fields affect the relevant properties of the ring structures, including electronic structure and stability, is crucial [20]. This is where the investigation at the molecular level is useful for the design and functionality of the ring junction devices. Significant theoretical studies have been carried out to understand how the applied electric field influences the geometry, spectra, frontier orbitals and energies of ring structures [21–25], which are responsible for a number of properties, including the

current conduction behavior [26] and other relevant properties for device applications [27]. However, only limited studies are available concerning field influence on the H-bonded ring structures formed out of a few number of water or methanol molecules [28–30].

The most prominent interaction in the case of an H-bonded network of water molecules subjected to an external field is the dipole-field interaction, which determines how the H-bonded networks are adapted in response to the field since each water molecule has a preferred orientation along the field direction. Therefore, understanding how robust or flexible the H-bonded networks of water molecules are to the applied electric fields is very crucial for designing or adding functionalities to the water-based devices and electronics [31–36]. Flexible nanoelectronic devices based on unique characteristics of H-bonding interaction would represent an innovative approach to design electronic components that can be integrated into flexible substrates or other device components [37]. In particular, the unique properties of water molecules to form simple to intricate H-bonded networks under different conditions play crucial roles in the self-assembly processes. Moreover, the use of water molecules for self-assembly offers a sustainable and environmentally friendly approach to device fabrication and integration. However, challenges needed to address important issues such as precise control over device properties and stability under various external influences [38] remain the subject of open research [39].

The dipole-field interactions can also have significant impact on the other physical processes, such as proton transport in water [40–42], water flow rate [43] and diffusion [44, 45], which are important for designing nanofluidic devices [46, 47], molecular sieves [48, 49], and desalination channels [50, 51]. Applying an electric field is also demonstrated to have an impact on the H-bond lengths in the H-bonded networks. A computational study has shown highly compact H-bonds featuring very strong H-bonds in the water whiskers in the presence of electric fields [52]. Isolated water chain structures or water whiskers are capable of withstanding

extremely strong fields of up to 1 V/\AA [52, 53], which is four times stronger than the critical field 0.25 V/\AA that causes the dissociation of water molecules in liquid water [40, 42]. This contrasts sharply with liquid water [54], where the oxygen-hydrogen bonds are significantly weakened by changes in the local electric field brought on by molecular motion, enhanced intermolecular interactions, and mutual polarization, which facilitates field-induced water dissociation at a lower field value of 0.25 V/\AA .

The water molecules also coordinate with ions to form organized H-bonded networks that include ring structures [55]. This facilitates strong interaction within the network that can be potentially exploited in the flexible energy-dissipation devices [39]. In an effort to understand and exploit some of the peculiar characteristics of the H-bonded ring structures, we consider exotic nanoscale ring water structures consisting of 36, 72, and 108 water molecules that resemble twisted ribbon joined end-to-end. This work focuses on the impact of electric fields on the stability, geometric and electronic structures, and distinctive characteristics that are significant for device applications. A thorough examination of the distinctive local modes of a ring's vibrational response to applied fields, as revealed by the IR and Raman spectra, enables their manifestation from spectroscopic signatures. Nevertheless, we do not examine the disintegration of ring structures into arbitrary structures occurring at very strong fields.

3.2 Scope of the Work

In this chapter, we examine H-bonded networks of water molecules where the basic repeating units are the four-membered ring water clusters that share a corner water molecule and oriented perpendicular to each other. When connected end-to-end, they form twisted ribbon networks resembling crown- or bracelet-like ring structures. H-bonding water molecules resembling crown-like structures have also been reported to exist under confined conditions [56]. Here we consider three

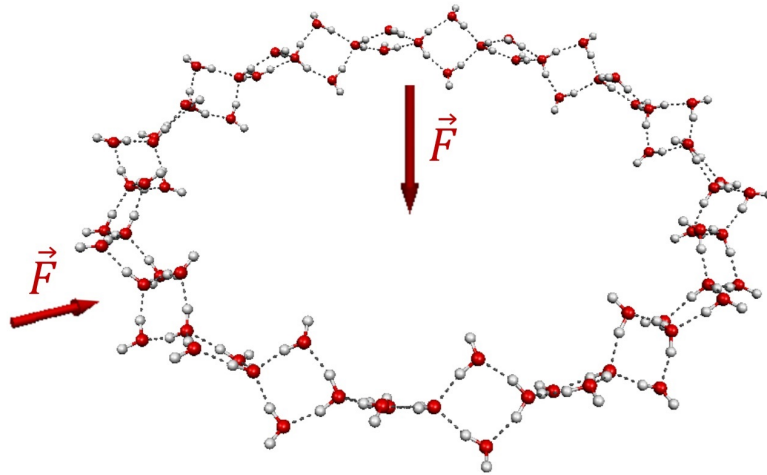


FIGURE 3.1: Nanoscopic H-bonded ring formed by 72 water molecules organized in a twisted ribbon-like network. The arrows indicate the directions along which an electric field (\vec{F}) is applied, i.e., parallel and perpendicular to the ring.

nano-sized ring water structures. Their overall configurations varied slightly, with two of them being polar and non-symmetric and the other being very symmetric, and therefore, non-polar. A representative structure is shown in Fig. 3.1.

Recent years have seen significant interest in the understanding of the electron conduction properties of the H-bonding systems [57–61]. Interestingly, it was observed that H-bonds conduct electrons more effectively than covalent bonds, while the efficiency decreases with increasing the H-bonded chains [62, 63]. Such investigations are driven by two goals: one is to explore the effects of water on the conductivity properties [64–67], and the other is to advance the promising field of water-based devices and electronics [31–36]. For the latter objective, the ring structures under consideration could serve as a test-bed for examining the conduction characteristics of H-bonded ring structures. The reason ring structures are of interest in molecular electronics is that they show unique conduction characteristics due to quantum interference between the competing pathways, which can be modulated by applied magnetic field [68, 69]. Therefore, a deeper understanding of how the H-bonded ring structures respond to the applied field is crucial for the feasibility of using such ring structures in high electric field conditions in molecular junction setups. Addressing this is one of the main objectives of the present

endeavour.

We examine how electric fields affect the H-bonded ring structures when applied parallel and perpendicular to the ring structures. This holds significance for the structural integrity of the H-bonded ring structures against bond breaking caused by electric fields in molecular junction devices operating at high voltage bias [70], which also occurs as a result of bias-induced circular current in the ring structures [71]. Moreover, the substantial dipole moment of the H-bonded ring structures in the field may provide ring junction-based molecular devices with additional functionalities, since the device characteristics are substantially modulated by the coupling of the dipole moment of ring structure with the junction field or external electric gate field [72]. Concerning the potential existence of such ring structures, the infrared and Raman spectral analysis of local modes typically demonstrates the vibrational response of water molecules to various H-bonding environments and applied fields, thereby providing a spectroscopic signature that can be used to identify the manifestation of such H-bonded ring networks.

Here, we perform density functional calculations to investigate the structure, energetics, and stability of the H-bonded ring structures in the external electric field in the hope of providing some useful insights on some of the intriguing objectives. We'll examine and discuss characteristics that are relevant to device applications. However, our results are limited to particular situations, like the matrix-isolated small water cluster rings [73], where our calculations can be compared. We now provide a detailed strategy for calculations in this chapter.

3.3 Methodology and Computational Details

We generated several ring structures and optimized them at the Hartree-Fock level of theory using the Gaussian 16 suite of programs (GAUSSIAN) [74]. The characteristic response of such ring structures to the electric field is studied by considering only three representative ring structures within the DFT description.

The ring structures include a H-bonding network that is essentially symmetric and non-polar, as well as a less symmetrical polar configuration. Geometry optimization in the field not only establishes the characteristic response of the system as deduced from the properties depending on the field, but it also determines the preferred orientation of the system relative to the applied electric field.

The uniform and static electric fields employed in the calculations are effected through a keyword `Field=X-5`, which adds 0.0005 a.u. electric field, i.e., 26 mV/Å field along +X direction. For all rings under consideration, fields are applied both parallel and perpendicular to the ring planes. We use the popular hybrid density functional B3LYP with a decent basis set 6-31+G(d,p) for both the geometry optimizations and frequency calculations. Furthermore, using the 6-31++G(d,p) basis set, which also adds diffuse functions to hydrogen atoms, computations are performed in the presence of an electric field and the results are compared for if the basis set effect is significant. Since the ring systems under consideration are the extended structures, we also perform calculations using a hybrid functional ω B97X-D, which is appropriate for characterizing non-covalent and medium to long-range dispersion interactions [75]. The ω B97X-D calculations are compared and/or contrasted with the B3LYP results. However, unless stated otherwise, the results presented in the next sections are obtained from the B3LYP/6-31+G(d,p) level of theory calculations.

The applied electric field \vec{F} is increased progressively in steps of 0.0005 a.u. (1 a.u. \approx 51.42 V/Å) until no more geometry optimization is feasible. The preferential reorientation of water dipoles along the field at large field values severely disrupts the hydrogen bonds, leading to repeated failure of the optimization process. The maximum field applied is also indicative of the characteristic high field a ring can sustain, beyond which the ring tends to form an arbitrary structure. When exposed to an applied field, a molecular structure may go through a transition state that is characterized by the presence of imaginary vibrational frequencies. However, the computed vibrational frequencies in the presence of an applied field were

all determined to be real, which validated the local minimum configurations of the structures for each value of the applied field.

As outlined in the preceding chapter, a field in the range not exceeding 0.02 a.u. or 1.02 V/Å, is typical in the vicinity of nanotips [76] and in the STM [77, 78] and AFM setups [79–81].

3.4 Computed Results and Discussion

We now present the structural features of the nano-rings, followed by a discussion on stability and field-induced structural evolution. Non-covalent interactions have been analyzed within the well-established reduced density gradient formalism. Later sections address the field influence on vibrational spectra, while the last section explores the technological implications of the work.

3.4.1 Structure, Stability and Dipole Moment

A pair of perpendicularly oriented 4-membered ring water clusters that share a water molecule represents the fundamental building unit of the nano-sized ring water structure considered in the work. Each structural unit consists of seven water molecules as shown in Fig. 3.2 (a). The molecular electrostatic potential (MESP) surface for the structural unit is shown in Fig. 3.2 (b). The MESP surface reveals the regions of high and low electron density that can be considered as a reference to identify the most favorable bonding sites for molecular clustering of the structural units that result in the formation of ring structures considered in this work. In the present study, we have considered 6, 12 and 18 such structural units that cluster up to form three nano-sized ring structures having 36, 72 and 108 water molecules, respectively. These structures, shown in Fig 3.3, are labeled as T4(1)-6R, T4(1)-12R, and T4(1)-18R, in accordance to the nomenclature employed in [82]. The T4(1)-6R ring structure obtained by successively repeating six tape

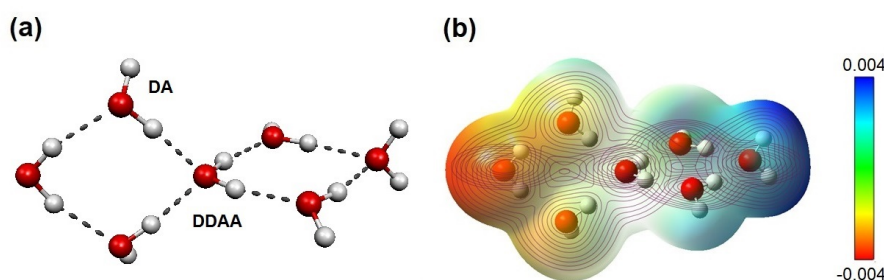


FIGURE 3.2: (a) A structural unit consisting of 2- and 4-coordinated water molecules, labeled as DA and DDAA respectively, which on successive repetition by sharing water molecules generate the nano-sized ring water structures. (b) MESP topology in a.u. mapped on electron number density iso-surface value set at ± 0.004 a.u.

(T) structures of four-membered rings sharing a molecule has C_6 symmetry, and the larger T4(1)-12R and T4(1)-18R rings are S_8 and C_6 symmetric, respectively.

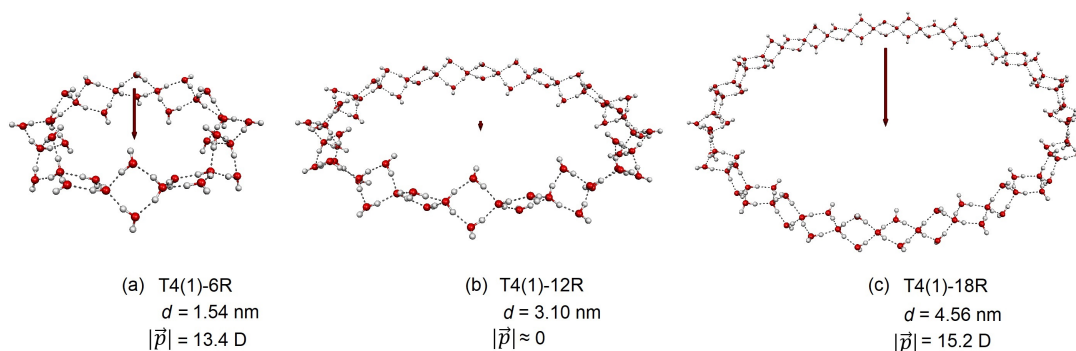


FIGURE 3.3: (a) T4(1)-6R, (b) T4(1)-12R and (c) T4(1)-18R nano-sized rings consisting of 36, 72 and 108 water molecules with an average diameter (O...O distance between the diametrically opposite DDAA molecules) of 1.54, 3.10, and 4.56 nm and possessing a permanent dipole moment ($|\vec{p}|$) of 13.4, 0 and 15.2 Debye (D), respectively, oriented perpendicular to the ring geometry.

Viewed in terms of the proton donor (D)-acceptor (A) coordination of each water molecule that is essential for the formation of H-bonds, all nano-ring structures under study exhibit two H-bonding patterns, involving 2- and 4-coordinated water molecules in the DA and DDAA pattern, respectively. As shown in Fig. 3.2 (a), one of the O-H bonds of each DA water molecule is H-bonded, while the other remains free and does not participate in the H-bonding network. Such coordination of water molecules consequently gives rise to 48, 96 and 144

number of H-bonds in the T4(1)-6R, T4(1)-12R, and T4(1)-18R rings, respectively. The optimized geometry of the nano-ring structures, T4(1)-6R, T4(1)-12R, and T4(1)-18R, have the average O...O distance between diametrically opposite DDAA water molecules to be 1.54, 3.10 and 4.56 nm, respectively. However, it must be mentioned here that these nano-ring structures, unlike the previously studied linear chain structure, are structurally stable even in the absence of a field. Thus, a minimal field is not required to support the extended structures.

Now, to examine the energetic stability of the T4(1)-6R, T4(1)-12R, and T4(1)-18R structures, we evaluate the stabilisation energy of structures as the difference between the energy of the ring structure and the sum of the energies of its constituent water molecules in isolation. The stabilisation of nano-ring structures

TABLE 3.1: Zero-point energy (ZPE) corrected stabilisation energy of the T4(1)-6R, T4(1)-12R and T4(1)-18R nano-rings evaluated at the B3LYP/6-31+G(d,p) level of theory.

Structure	ZPE corrected total energy (Hartree)	Stabilisation energy (kcal/mol)	Stabilisation energy per H-bond (kcal/mol)
H ₂ O	-76.412758		
T4(1)-6R	-2751.287636	-268.7	-5.5
T4(1)-12R	-5502.583996	-543.0	-5.6
T4(1)-18R	-8253.888177	-822.2	-5.7
Water dimer			-3.3±0.1 ^a
Ice			-7.0 ^b

^aReported from experimental value of the enthalpy of dimerisation [83].

^bCalculated from experimental lattice energy of the various ice phases [84].

by H-bonding, as presented in Table 3.1, shows that the stabilisation energy ranges around -5.6 ± 0.1 kcal/mol per H-bond. These values are found to lie within the experimental stabilisation energy estimates for water dimer and ice. The nano-ring structures become more stable with growth, as indicated by the increase in stabilisation energy values in Table 3.1. The stabilisation energy per H-bond, however, does not necessarily follow a consistently increasing trend [85, 86] and is expected to saturate within the first few decimals of 5.6 kcal/mol per H-bond [85].

Having assessed the stabilisation energy of optimized field-free T4(1)-6R, T4(1)-12R and T4(1)-18R structures, we study the structural evolution of these structures under a static and uniform electric field application. To begin with, we consider the smallest T4(1)-6R ring as shown in Fig. 3.3, having a permanent electric dipole moment of ~ 13.4 Debye perpendicular to the plane of the ring. When the electric field is applied along the plane of the ring, even a very low field strength of 0.001 a.u. distorts the ring structure, and on further increasing the field strength, it transforms into arbitrary complex structures. The T4(1)-12R and T4(1)-18R structures also undergo similar structural transformations for the same field direction. Therefore, the nano-ring structures under consideration are structurally unstable for fields that are oriented parallel to the plane of the ring geometry. The ring structures, however, are stable for the field directed perpendicular to the plane of the T4(1)-6R ring, i.e. along its permanent dipole moment direction. The T4(1)-6R is found to maintain its structure up to a field strength of 0.019 a.u. after which the structure begins to disrupt resulting in complex structures. The T4(1)-12R and T4(1)-18R geometries are also found to be stable for the field directed perpendicular to the plane, maintaining their structures up to a maximum field value of 0.011 a.u and 0.009 a.u., respectively. Consequently, all the results presented herein corresponds to fields that are applied in a direction perpendicular to the plane of the ring structure.

The variation of the dipole moment and H-bond length with the field for the nano-rings are illustrated in Fig. 3.4. The structural evolution of the T4(1)-6R ring in response to the applied field is rather smooth, as indicated by the steady increase of dipole moment and H-bond length as a function of field strength. As shown, for the field strength in the range 0 to 0.019 a.u., the average H-bond length increases from 1.775 Å to 1.826 Å. Meanwhile, the dangling OHs oriented initially in the direction opposite to the applied field gradually orient themselves along the field direction, thereby increasing the net dipole moment from ~ 13.33 Debye to a maximum value of ~ 50.58 Debye at 0.019 a.u. Here, we note that the dipole moment and H-bond length values computed with a larger

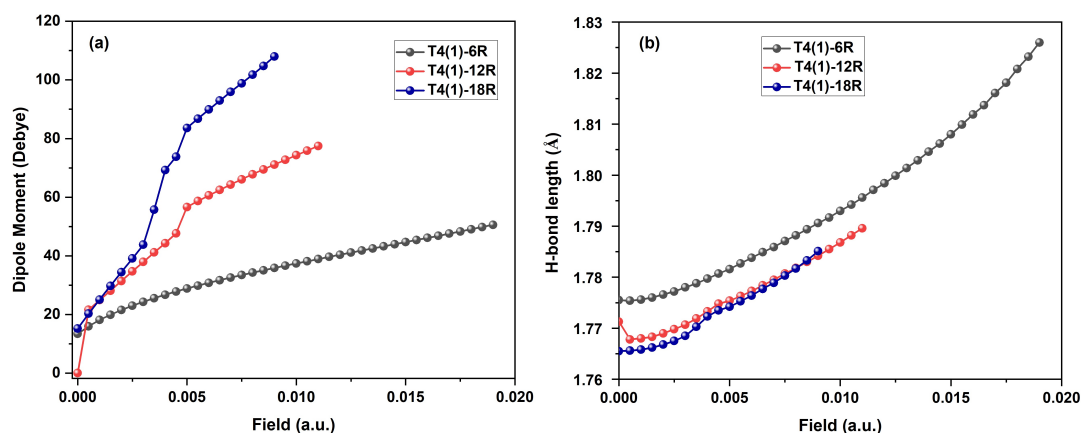


FIGURE 3.4: Variation of (a) dipole moment and (b) average H-bond length with the field applied perpendicular to the plane of the ring structures. The field free dipole moment for T4(1)-6R, T4(1)-12R and T4(1)-18R are 13.4, 0 and 15.2 Debye, respectively.

basis set 6-31++G(d,p) for the T4(1)-6R ring show no discernible difference from the 6-31+G(d,p) calculated values. In the case of a highly symmetric non-polar T4(1)-12R ring with a negligible permanent electric dipole moment in the field-free case, the field-induced dipole moment increases with the field showing an abrupt increase at a field strength of 0.005 a.u. corresponding to the realignment of dangling OHs along the applied field direction. The induced dipole moment attains a value of 77.4 Debye at a maximum field strength of 0.011 a.u. that the T4(1)-12R structure can sustain. As a consequence, the average H-bond length increases from 1.771 Å to 1.789 Å, even though it initially decreases below the field-free value caused by the reorientation of constituent dipoles in the field, thus reorganizing the H-bond network in the applied field. The T4(1)-18R ring with a permanent dipole moment of ~ 15.2 Debye is stable in a very narrow field range of (0–0.009 a.u.) with the average H-bond length varying from 1.765 Å to 1.785 Å. Structural variation similar to the T4(1)-12R structure is observed for the T4(1)-18R structure, marked by an abrupt increase in the dipole moment at 0.0035 a.u. field value, at which the alignment of dipoles becomes so important that the free OH bonds suddenly reorient along the direction of the applied field. Overall, it is noticed that with the increase in the rings' size, the structural stability of H-bonded ring structures decreases. Similar to the case of larger linear water chains

discussed in the preceding chapter, the larger nano-rings are more susceptible to the electric field effect than the smaller ones because of the increased dipole-field interaction caused by an increase in mutual polarization between the dipoles when the size of the structure grows. However, in contrast to the linear water chains, which exhibit an increase in chain length while the average H-bond length decreases with an increase in field strength, the nano-rings under study show an opposite trend. The ring size, instead, decreases even though the average H-bond length increases with the field, while the H-bonded O-H bonds tend to reorient in the direction of the applied field.

Additionally, we also take note of how the entropy of nano-rings under consideration varies in response to an external field. The entropy of the H-bonded ring structures is found to decrease with the application of a field, however, it increases at higher field strengths. On examining the thermodynamic data obtained at a standard temperature of 298.15 K and pressure of 1 Atm, the rotational entropy of water dipoles decreases with an increase in field strength due to the gradual alignment of water dipoles along the field direction. Meanwhile, the vibrational entropy, which is the major component of total entropy in this case, initially decreases with the increase in the field due to field-induced local structural adjustments causing each water dipole to relax in the local field but subsequently increase at a higher field strengths, resulting from an extensive disruption in the bonding environment of the otherwise ordered H-bonded structure of the water nano-rings. Specifically, on the application of the field perpendicular to the plane of the T4(1)-R ring, the rotational entropy decreases gradually from its field-free value of 41.8 cal/mol-K. However, the vibrational entropy, initially at 481.0 cal/mol-K at zero field, decreases to 432.3 cal/mol-K at a field strength of 0.0155 a.u., before increasing to 439.7 cal/mol-K at the field strength of 0.019 a.u. The T4(1)-12R and T4(1)-18R nano-rings exhibit a similar trend, although the increase in vibrational entropy at higher field strengths is not as pronounced as it is for the T4(1)-6R ring. This observation is consistent with a recent study using the molecular dynamics simulations of liquid water subjected to an electric

field that demonstrated a decrease in the entropy of bulk water molecules exposed to an electric field [87].

3.4.2 Noncovalent Interaction (NCI) Analysis

As outlined in Chapter 1, the noncovalent interaction (NCI) analysis can be carried out by analysing a dimensionless quantity, i.e., the reduced density gradient (RDG). To elucidate and characterise the interactions leading to energetically stable nano-sized ring structures under consideration, we perform the noncovalent interaction analysis by plotting the RDG isosurface maps and its corresponding RDG scatter plots for the structural unit and that for the three nano-rings at the B3LYP/6-31+G(d,p) level of theory. As depicted in Fig. 3.5 (a), in the structural unit comprising of DA and DDAA coordinated water molecules, a horizontal line intersects the scatter plot at 0.5 RDG value at various locations. These locations are then mapped in the corresponding structure. The scatter plots and NCI-RDG isosurfaces presented in Fig. 3.5 for (b) T4(1)-6R, (c) T4(1)-12R and (d) T4(1)-18R ring structures are obtained likewise. In the scatter plot for the structural unit, the RDG plot exhibits two prominent troughs (inverted narrow peaks) for $\text{sign}(\lambda_2)\rho(r)$ value in the range -0.03 a.u. to -0.02 a.u., suggesting stronger H-bonding (dark blue) with DDAA water molecules and less strong H-bonding (light blue) with DA water molecule, while a trough in the vicinity of $\text{sign}(\lambda_2)\rho(r) \simeq 0$, indicates the presence of weak van der Waals (vdW) interactions. Upon ring formation, the two distinct troughs combine to sharpen and migrate towards a more negative $\text{sign}(\lambda_2)\rho(r)$ region, which becomes even more evident in the larger ring structures. On the other hand, the trough around $\text{sign}(\lambda_2)\rho(r) \simeq 0$ characterizing weak interactions remains essentially unaffected with the growing ring size. The NCI analysis shows that the H-bonding interactions become stronger, identical and uniform with the increasing ring size, demonstrating that the NCIs between the water molecules in the ring structures are predominantly H-bonding, thus validating our choice of the B3LYP functional for the present study [88].

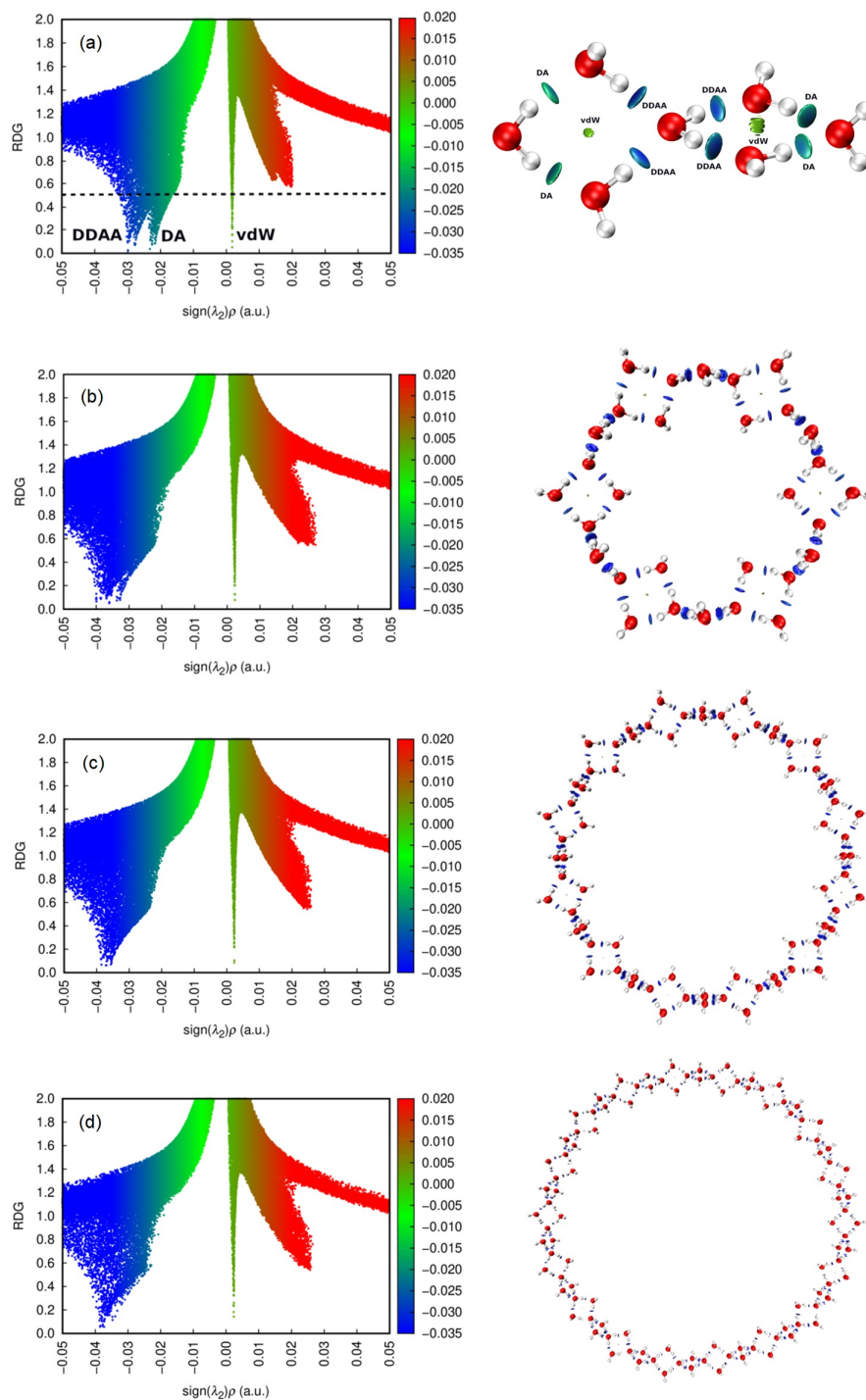


FIGURE 3.5: RGB (red-green-blue) colour scatter plots illustrating the variation of RDG against $\text{sign}(\lambda_2)\rho(r)$ in (a) structural unit, (b) T4(1)-6R, (c) T4(1)-12R and (d) T4(1)-18R nano-rings, and the isosurfaces depicting NCI regions in the respective nano-rings at RDG value of 0.5 computed at the B3LYP/6-31+G(d,p) level of theory.

3.4.3 Frontier MOs and HL Gap

With the advancement in molecular cluster-based electronics [62, 63, 89, 90], the study of the frontier orbital energy gap, i.e. the energy difference between the HOMO and the LUMO in a molecular cluster has become increasingly important. As discussed in Chapter 1, in the case of water nano-chains, the HOMO-LUMO (HL) energy gap (E_g) is associated with the kinetic stability and chemical reactivity of a system. Higher energy gaps are closely linked to increased energy needs for electrons to make transition from an occupied orbital to an unoccupied orbital. Thus, a large E_g is indicative of the kinetic stability of the system against further clustering or fragmentation and a remarkable chemical inertness. With the

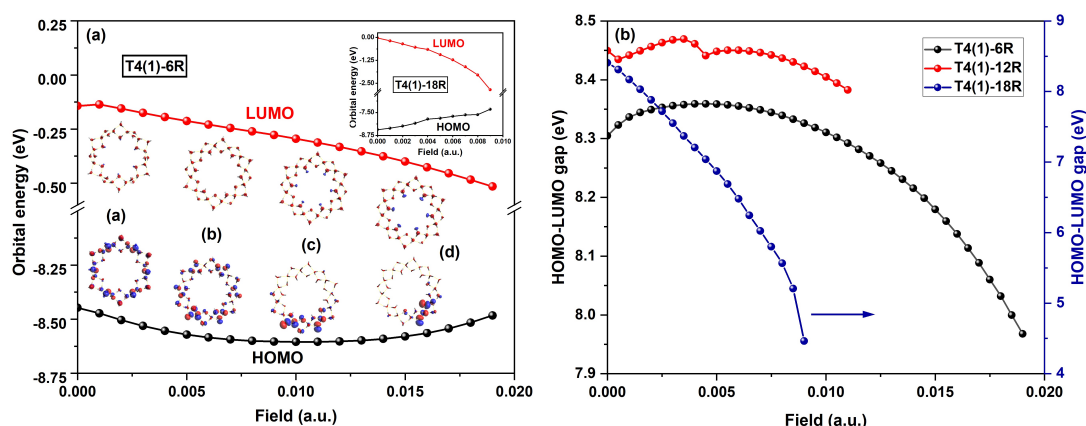


FIGURE 3.6: (a) Frontier molecular orbital (MO) energies in T4(1)-6R as a function of the electric field in the range of 0 to 0.019 a.u. applied perpendicular to the ring plane. The HOMO and LUMO for field values, (a) 0, (b) 0.0050, (c) 0.0100, and (d) 0.0150 a.u. shown are drawn at the contour value ± 0.02 . The inset depicts the field variation of frontier MO energies for T4(1)-18R. (b) Evolution of the HL gap for the T4(1)-6R, T4(1)-12R and T4(1)-18R rings with field.

increase in field strength, the energy gap E_g for the chain structures considered in the preceding chapter was found to increase up to a threshold field value beyond which the energy gap decreases. A similar variation of E_g with field is observed for the T4(1)-6R and T4(1)-12R structures, as shown in Fig. 3.6 (b). The threshold field for T4(1)-6R is 0.004 a.u., while T4(1)-12R exhibits a double hump due to the structural rearrangement caused by the applied field. The T4(1)-18R ring, on

the other hand, does not exhibit such behavior, the energy gap rather steadily decreases with an increase in field. The energy gap for the T4(1)-6R ring employing a 6-31++G(d,p) basis set at each field strength is found to be 1 eV smaller than the values determined at the 6-31+G(d,p) basis set. For the T4(1)-12R ring, a similar variation in energy gap characterized by a double hump was reproduced by calculations performed at the ω B97XD/6-31+G(d,p) level of theory, however, the energy gap at each field strength is found to be around 4.5 eV higher than B3LYP/6-31+G(d,p) calculated values. Here, we emphasize that the increase in the HL gap with the applied field is related to the structural relaxation and localizations of the frontier orbital in the system [91, 92]. With the increase in field, the water dipoles relax progressively in the local field until saturation occurs at the threshold field. Beyond the threshold field, the energy gap decreases indicating structural disruption resulting from the forceful alignment of water dipoles along the field direction, which leads to the eventual breakdown of the structure at sufficiently large fields.

The evolution of the HL gap can be understood in terms of the field-induced migration and localisation of the HOMO and LUMO [53, 92], the schematic of which is presented in Fig. 3.6 (a) for the T4(1)-6R ring structure. With the application of field, the HOMO undergoes delocalisation over the ring, albeit unevenly, thus lowering the orbital energy till a certain field strength, beyond which the orbital energy rises as the HOMO migrates to a particular region of the ring where it becomes localised. Meanwhile, the LUMO progressively delocalises towards the inner edge of the ring, thereby causing a steady decrease in its energy. This variation of orbital energy with field results in the initial growth of the HL energy gap in T4(1)-6R and T4(1)-12R structures and its eventual fall after the threshold field value. However, for the T4(1)-18R ring having no threshold field, the energy gap undergoes progressive narrowing with the increase in field (inset figure of Fig. 3.6 (a)), which is indicative of increased susceptibility of larger ring structures to field influence.

Here, we note that considering the useful range (0.5 to 3 eV) for the energy gap suitable for optoelectronic device applications, the nano water rings under study have a significant HL energy gap, $E_g > 4$ eV, which can limit the potential use of such ring structures for optical device applications. The energy gap, however, can be tuned by the application of an external electric field and can be made useful in manipulating the conduction properties of nano-rings under study. We now present the infrared spectra of the ring structures and their evolution as the field strength is increased.

3.4.4 Infrared Spectra

A water molecule in the gas phase exhibits discrete line peaks in its infrared (IR) vibrational spectrum about 1595 cm^{-1} , corresponding to the H-O-H bending mode, and around 3657 and 3756 cm^{-1} , associated with the symmetric stretching (SS) and antisymmetric stretching (AS) of the O-H bonds, respectively [93]. However, for water clusters with intricate H-bonded networks, in addition to the peaks associated with bending and stretching modes, the IR vibrational spectra exhibit peaks in the low frequency corresponding to hindered translations and rotations (called librational modes) of the water molecules. It is interesting to study the effect of an external field on the vibrational dynamics to comprehend the dissipation of vibrational energy in the water molecules, and to investigate the implications of the vibrational energy dissipation pathways and energy management for technological applications.

The frequency calculations are performed for all the field-optimized structures, thereby generating a series of in-field IR spectra. All the frequencies were found to be real confirming the local minima configurations for the field-optimized structures. The IR spectra for all three nano-ring structures under study in the absence of field, along with the experimentally obtained features for bulk liquid water, redrawn from [94] as shown herein by a dotted curve, are presented in Fig.

3.7 (a). The computed spectral features are presented in Gaussian line shape with an FWHM bandwidth of 40 cm^{-1} . As shown in the IR spectrum for nano-rings for the field free case, the librational modes lie below 990 cm^{-1} , the bending modes with two distinct peaks lie in the range of 1640 cm^{-1} to 1760 cm^{-1} , and the SS and AS modes of the O-H bonds range from 3310 cm^{-1} to 3910 cm^{-1} frequency oscillations with varying intensities. The obtained spectral features of the three nano-rings qualitatively fit within the experimentally determined overall spectral envelope of liquid water. However, the spectra computed within the harmonic approximation used in the present investigation lack a relatively weak and broad feature present in the experimental profile at around 2140 cm^{-1} which corresponds to the “libration+bending” mode associated with the anharmonic effects [95, 96]. In Fig. 3.7 (b), the field evolution of the IR spectrum for the T4(1)-6R structure at

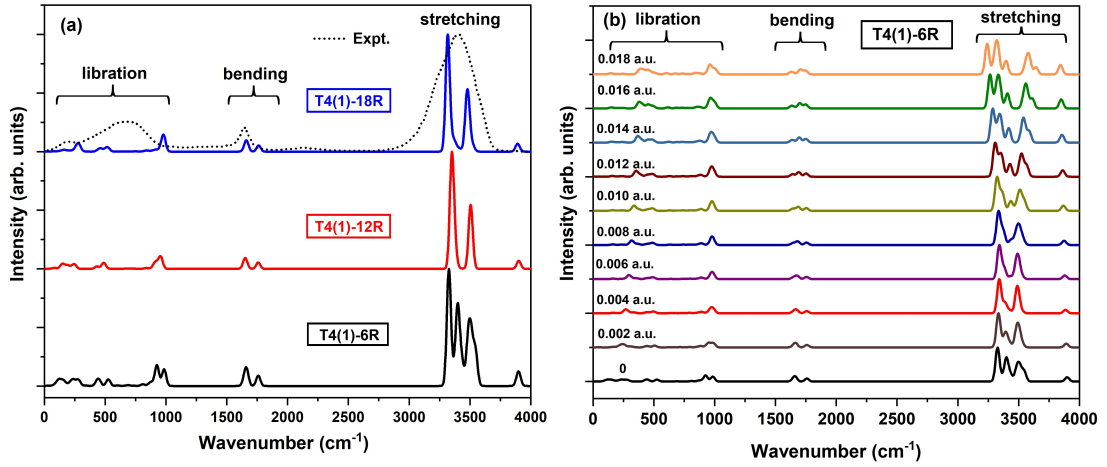


FIGURE 3.7: (a) Full IR spectra of the three nano-rings for field-free case, along with the experimental profile for bulk liquid water (dotted spectral profile) redrawn from [94]. (b) Evolution of the IR spectra of the T4(1)-6R nano-ring under the influence of field in the range 0-0.018 a.u.

the indicated field values are presented. It is evident from the figure that the field effect is significant in the stretching and bending regions of the spectra, while the changes in the librational band are not very noticeable. According to a recent ab initio molecular dynamics simulation-based investigation of bulk liquid water, the applied field is found to compress the entire spectrum causing modifications in the librational mode and red-shift of the O-H stretching band, thereby suggesting the

strengthening of the H-bonding on field application [97]. When compared to the bulk liquid water, the water nano-rings under study do not show such field-induced H-bond strengthening and ice-like water ordering that the bulk liquid water does.

3.4.5 Bending mode

To describe the vibrations in the bending region, we consider the vibrational peaks within the 1600 cm^{-1} to 1800 cm^{-1} range, as shown in Fig. 3.8. In the absence of field, the most significant bending modes correspond to an asymmetric bending (ν_1) of the paired DA water molecules in alternate rings at 1648 cm^{-1} and the symmetric bending (ν_2) of all DA and DDAA molecules at 1662 cm^{-1} . The two peaks ν_1 and ν_2 give rise to the first peak ($\nu_1 + \nu_2$) at $\sim 1660\text{ cm}^{-1}$. The second peak

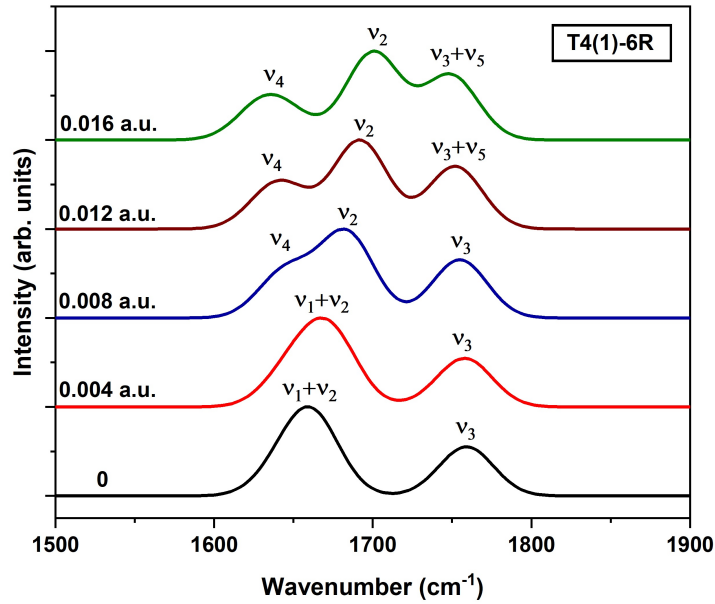


FIGURE 3.8: Field-induced variation of H-O-H bending modes in the T4(1)-6R nano-ring, while the detailed description is presented in the text.

at 1760 cm^{-1} is associated with the third bending mode (ν_3) i.e., the symmetric bending of all DDAA water molecules. When the field is applied, the intensity of ν_1 mode is found to diminish and gradually becomes inactive. A new mode (ν_4) corresponding to the symmetric bending of all DA molecules, however, appears as a shoulder at about 1645 cm^{-1} , whereas the ν_2 mode decouples from the first

and emerges as a distinct peak at $\sim 1680 \text{ cm}^{-1}$ as indicated in the Fig. 3.8 for a field value of 0.0080 a.u. Further strengthening of the field leads to a new mode (ν_5) corresponding to the asymmetric bending of the alternate DDAA water molecules comprising the third peak ($\nu_3 + \nu_5$) centered at about 1750 cm^{-1} for the field strength of 0.0120 a.u. This spectral feature with three prominent peaks at larger field values essentially persists up to a maximum field of 0.019 a.u., after which the T4(1)-6R geometry enters into a stationary point on its potential energy surface with two imaginary frequencies.

In the case of T4(1)-12R and T4(1)-18R nano-rings, essentially similar characteristics with two distinct bending mode peaks separated by $\sim 110 \text{ cm}^{-1}$ and $\sim 100 \text{ cm}^{-1}$, respectively, are observed in absence of field. On field application, as observed for the T4(1)-6R nano-ring, the corresponding field-free peaks evolve resulting in the distinctive three peaks at higher field values. The study of such H-O-H bending vibrational features is appealing as they can serve as a marker for characterizing the different H-bonded networks present in various configurations and diverse environments [98]. It is interesting to note that the study of the H-O-H bending mode, as opposed to the more widely studied O-H stretch mode, has been shown to allow direct access to the H-bond network, as well as in understanding efficient mechanisms related to vibrational energy delocalisation and dissipation [99].

3.4.6 Stretching mode

We next consider the O-H stretching region between 3200 cm^{-1} to 3900 cm^{-1} for the T4(1)-6R ring. The O-H stretch region between $\sim 3300 \text{ cm}^{-1}$ to $\sim 3600 \text{ cm}^{-1}$ is associated with the active participation of the H-bonded O-H bonds, while that at higher frequencies over $\sim 3800 \text{ cm}^{-1}$ corresponds to the stretching of dangling O-H bonds of the DA water molecules. Moreover, the O-H stretching region for the T4(1)-6R ring is isolated and its variation in response to the applied field is

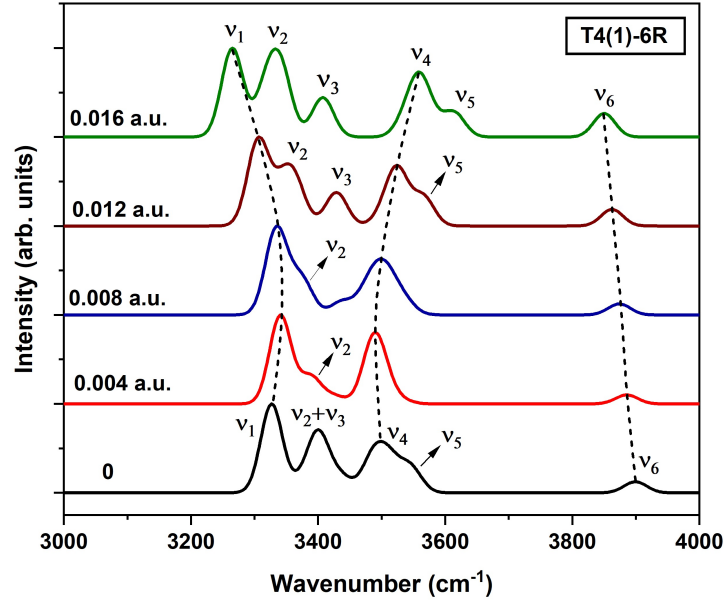


FIGURE 3.9: Field-induced evolution of O-H stretching modes in the T4(1)-6R nano-ring. Detailed descriptions of the vibrational modes and the associated peaks are presented in the text.

studied as presented in Fig. 3.9. The first peak at $\sim 3325 \text{ cm}^{-1}$ is associated with the H-bonded O-H stretch mode (ν_1), which corresponds to the SS of the DDAA molecules. A strong H-bonded O-H stretch mode (ν_2) at 3400 cm^{-1} attributed to a combined SS and AS of the DDAA water molecules and another H-bonded OH stretch mode (ν_3) at 3436 cm^{-1} corresponding to SS of the alternate DDAA molecules result in the second peak ($\nu_2 + \nu_3$) centered at 3436 cm^{-1} . Another distinct mode (ν_4) that involves the AS of the DDAA molecules gives rise to the third peak at $\sim 3508 \text{ cm}^{-1}$, while the ν_5 mode associated with the mixture of both SS and AS of the alternate DDAA water molecules results in a shoulder peak at 3540 cm^{-1} . The active stretching mode of dangling the O-H bonds of the DA molecules (ν_6) results in the last peak at $\sim 3890 \text{ cm}^{-1}$.

On field application, as shown in Fig. 3.9, the H-bonded O-H stretching region undergoes a substantial narrowing for the field range 0.004-0.008 a.u., with ν_1 to ν_5 modes displaying both red- and blue-shifts in their frequencies, whereas the ν_6 mode exhibits monotonic red-shift. Notably, at a field value of 0.0120 a.u. and above, the ν_3 and ν_5 vibrational modes normally dormant on field application

become active, thereby featuring among others as prominent peaks. This characteristic feature comprising of peaks undergoing both red- and blue-shifts on field application, essentially persists up to a maximum field strength of 0.019 a.u. applied perpendicular to the plane of T4(1)-6R nano-ring, beyond which the applied field causes substantial distortion of the ring structure to the point of eventual collapse.

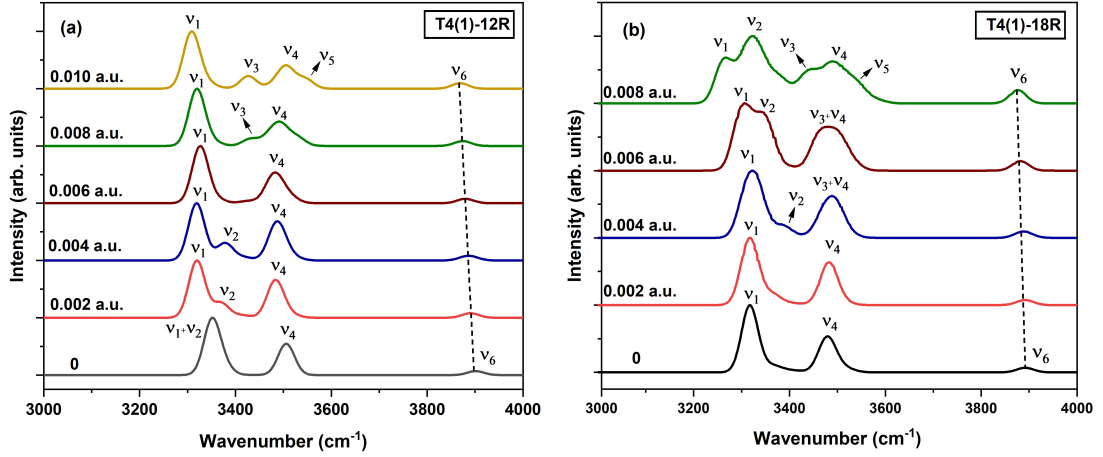


FIGURE 3.10: Field evolution of O-H stretching modes in the (a) T4(1)-12R and (b) T4(1)-18R nano-ring structures, wherein the labelling for vibrational modes is identical to that in Fig. 3.9.

The O-H stretching vibrational modes for the T4(1)-12R and T4(1)-18R structures, unlike the bending modes, are more sensitive to the applied field, as shown in Fig. 3.10. While the basic features of the H-bonded O-H stretch vibrations being shown in the range $\sim 3300 \text{ cm}^{-1}$ to $\sim 3600 \text{ cm}^{-1}$, and the dangling O-H vibration around 3900 cm^{-1} remain essentially same, however, the details of the vibrational modes and their response to the field are different. In the absence of field, the most distinct peaks in the H-bonded O-H stretching region are associated with the SS (ν_1) and AS (ν_4) of the DDAA molecules. These peaks exhibit both red- and blue-shifts for an increase in field strength, together with the appearance of shoulder peaks (ν_2 , ν_3 , and ν_5), which at higher field strengths develop into distinct peaks. Furthermore, at higher field values, the O-H vibrational stretch modes in the ring exhibit localized vibrations restricted to individual ring units as opposed to the otherwise extended across the ring. This is indicative of strain

in the ring geometry at higher fields as the vibrational localisation is a general feature of strain in the system that limits the molecular vibrations. This, again demonstrates that the larger rings are more susceptible to the applied electric field due to enhanced dipole-field interaction.

3.4.7 Raman Spectra

In addition to the IR vibrational modes, we also examine the Raman active modes for nano-rings under study. The vibrational modes in water molecules are both IR and Raman active [100], and in particular, the stretching vibrational modes are significantly Raman active than the bending and librational modes [101]. Consequently, the Raman spectrum for the T4(1)-6R ring shown in the Fig. 3.11 and its IR spectrum shown in Fig. 3.9 are identical, and the same holds for the other ring structures, T4(1)-12R and T4(1)-18R.

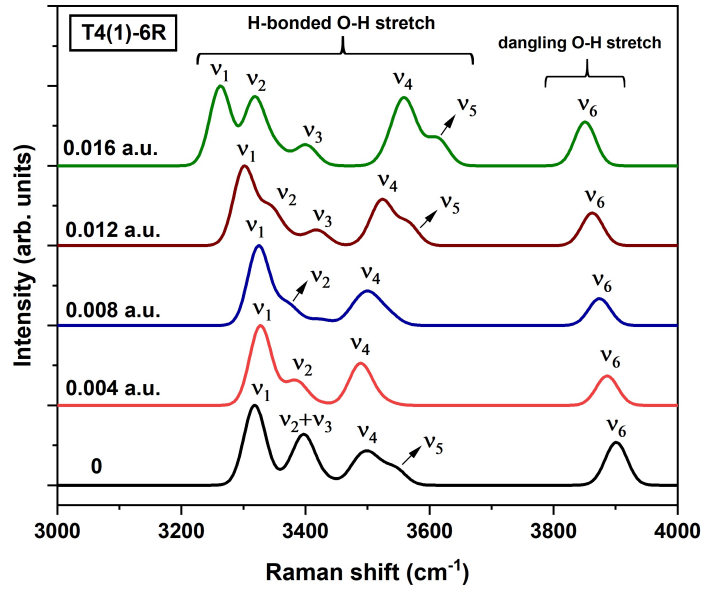


FIGURE 3.11: Field-induced variation of Raman signals in the O-H stretching region for the T4(1)-6R nano-ring. The labelling for vibrational modes is identical to that in Fig. 3.9.

The Raman spectrum for liquid water which consists of all possible water coordination, including the 3-coordinated DDA and DAA water molecules, is

usually deconvoluted into five sub-bands with peaks assigned to the OH stretch of such differently coordinated water molecules [100, 102, 103]. However, for the nano-ring structures under study, the Raman spectrum can be reasonably characterized into two sub-regions, the H-bonded O-H and the dangling O-H stretching region. The stretching region of the H-bonded O-H bonds in the range ~ 3200 cm^{-1} to ~ 3700 cm^{-1} comprises the Raman scattering of the O-H stretching of both DA and DDAA molecules, while it is the SS/AS of DDAA molecules and their various combinations produce various peaks which become distinct at higher field values. It is observed experimentally that the Raman active O-H stretch vibration at ~ 3420 cm^{-1} with a shoulder peak at ~ 3250 cm^{-1} [104] in the bulk liquid water undergoes a red-shift on the application of an electric field [97]. Contrary to this, as can be seen from Fig. 3.11 for the T4(1)-6R ring, the Raman peaks associated with the H-bonded O-H stretching frequency undergo both red- and blue-shifts when exposed to an electric field, whereas the dangling O-H stretching frequency is gradually red-shifted. Overall, as the Raman modes are sensitive to H-bonding environments [105, 106], the Raman spectrum studied for the ring structures offers a spectroscopic signature, which can be used in identifying their presence in suitable coordination environments, or their manifestation in the bottom-up fabrication of nano-structures through precise control of single molecules [107, 108].

3.5 Technological Implications

Here, we draw attention to the significance of the work presented in this chapter. While keeping an appropriate perspective on the water cluster-based device applications can be challenging, the insights gained from the study of nano-sized ring water structures unequivocally demonstrate their significant potential in the advancement of the molecular cluster-based nanoscale devices [89, 90]. One possible approach would be to fabricate the water ring structure junctions with a suitable anchoring group [109], which may facilitate the study of electron transport

characteristics along the H-bonded pathways [110, 111]. Such an approach could also facilitate the H-bond engineering aimed at designing stretchable and flexible electronic devices [112]. Additionally, owing to their substantial electric dipole moment, which amplifies with the applied field, the water nano-ring structures could be employed in designing molecular junction devices featuring dipole-modulated charge transport mechanisms [72, 113, 114].

Furthermore, it is hoped that the nano-ring structures can serve as a test-bed for understanding the electron transport mechanism in H-bonded molecular junction setups [115] and the role of H-bonds in forming the molecular conformational networks [116]. The latter aspect holds the potential to pave the way forward for new advancements in molecular electronics, such as the molecular device based on H-bonded conjugated molecules [117] and self-healing devices that rely on the dissociation and reformation of H-bonds [118]. The precise control and flexibility of H-bonds in terms of their breaking and reforming can regulate the energy dissipative properties of H-bonding, which could be advantageous for energy management in the H-bonding-based molecular electronic devices [119]. The widespread presence and adaptable nature of the H-bonds lead to the formation of diverse H-bonded networks depending on the conditions in which they are grown [120], or through local manipulation of the individual water molecules on a surface by the STM tip [121–123]. Indeed, the experimental enthusiasts might get motivated to explore along this direction with the goal of finding and discussing any potential observations of water nano-rings. Moreover, considering the significant cosmic implications of water nanoclusters [124], this endeavour holds considerable promise.

3.6 Summary and Concluding Remarks

In conclusion, our computational analysis demonstrates that the repeating of a H-bonded structural unit, consisting of a pair of perpendicularly arranged 4-membered ring water clusters sharing a water molecule, can result in the formation of energetically stable nano-sized water rings when joined end-to-end. These structures, created by repeating 6, 12, and 18 structural units successively, result in ring-shaped water clusters with diameters in the range 1.54 to 4.56 nm. The nano-sized water rings so formed exhibit both the non polar (higher-symmetry) and polar (lower-symmetry) H-bonded configurations. While, unlike their linear counterparts, these water nano-ring structures are structurally stable even in the absence of an external electric field. The larger rings are found to be more susceptible to electric field effects because of increased dipole-field interaction similar to what was observed for linear chains in the preceding chapter. For the in-plane field, the ring-shaped structures transform into arbitrary structures even at low field values. On the other hand, when the field is applied perpendicular to the plane of the ring, despite the dipoles tending to orient along the field direction, the nano-rings can even survive in fields as strong as 0.009 a.u. (≈ 0.46 V/Å), resulting in a dipole moment of the structures ~ 40 Debye or more. Due to collective physical processes that are typical and conducive to liquid water, such a strong field results in the dissociation of liquid water, while this is not the case for isolated water structures. Our results, however, are limited to specific situations wherein such calculations in the presence of an external electric field are deemed justifiable.

The substantial dipole moment, which is a key characteristic of the H-bonded ring structures on field application, can be utilized in designing dipole-modulated electron transport molecular junction devices. However, a comprehensive understanding would necessitate theoretical models that also consider the energy dissipation and thermal runaway mechanisms in the nano-sized H-bonded

junction devices. The HL energy gap of the water nano-rings decreases gradually under the influence of the applied field. However, since the energy gap lies outside the relevant operational range (0.5-3 eV), the potential use of these rings in opto-electronics device applications is limited. Nonetheless, the application of an electric field could potentially alter the conduction characteristics and the chemical stability of the water nano-ring structures. Also, a detailed analysis of the IR and Raman active vibrational mode spectra of the water nano-rings offers a spectroscopic signature which can be used in identifying their presence in suitable environments. Considering the significant implications of the water cluster-based molecular devices, especially exploiting their structural features, flexibility, and related properties, we hope that our results will stimulate experimental investigations on the water nano-ring structures.

References

- [1] Y. -G. Huang, Y. -Q. Gong, F. -L. Jiang, D. -Q. Yuan, M. -Y. Wu, Q. -Gao, W. Wei, and M. -C. Hong, *Cryst. Growth Des.* **7**, 1385 (2007).
- [2] B. Zhou, A. Kobayashi, and H. Kobayashi, *Chem. Lett.* **42**, 1131 (2013).
- [3] N. S. Oxtoby, A. J. Blake, N. R. Champness, and C. Wilson, *Chem. Eur. J.* **11**, 4643 (2005).
- [4] W. H. Noon, K. D. Ausman, R. E. Smalley and M. Jianpeng, *Chem. Phys. Lett.* **355**, 445 (2002).
- [5] S. Zang, Y. Su, C. Duan, Y. Li, H. Zhu, and Q. Meng, *Chem. Commun.* 4997 (2006).
- [6] R. Natranjan, J. P. H. Charmant, A. G. Orpen, and A. P. Davis, *Angew. Chem. Int. Ed.* **49**, 5125 (2010).
- [7] B. Q. Ma, H. L. Sun and S. Gao, *Chem. Commun.* **2220**, 2336 (2004).
- [8] B. -H. Ye, A. -P. Sun, T. -F. Wu, Y. -Q. Weng, and X. -M. Chen, *Eur. J. Inorg. Chem.* 1230 (2005).
- [9] X. -M. Zhang, R. -Q. Fang, and H. -S. Wu, *Cryst. Growth Des.* **5**, 1335 (2005).
- [10] J. P. Naskar, M. G. B. Drew, A. Hulme, D. A. Tocher, and D. Datta, *Cryst. Eng. Comm.* **7**, 67 (2005).
- [11] H. -Q. Hao, J. -X. Li, M. -H. Chen, and L. Li, *Inorg. Chem. Commun.* **37**, 7 (2013).
- [12] R. L. -Garcia, B. M. D. -Murillo, V. Barba, H. Höpfl, H. I. Beltrán, and L. S. Z. -Rivera, *Chem. Commun.* 5527 (2005).

- [13] L. Cheng, J. -B. Lin, J. -Z. Gong, A. -P. Sun, B. -H. Ye, and X. -M. Chen, *Cryst. Growth Des.* **6**, 2739 (2006).
- [14] H. J. Hao, D. Sun, F. J. Liu, R. Bin Huang and L. S. Zheng, *Cryst. Growth Des.* **11**, 5475 (2011).
- [15] J. Wu and J. Q. Liu, *Inorganica Chim. Acta.* **402**, 20 (2013).
- [16] M. J. Mayoral, N. Bilbao, and D. G. -Rodriguez, *ChemistryOpen*, **5**, 10 (2016).
- [17] O. Hod, R. Baer, and E. Rabani, *J. Phys. Chem. B* **108**, 14807 (2004).
- [18] O. Hod, and A. Nitzan, *J. Phys. Chem. Lett.* **2**, 2118 (2011).
- [19] O. Hod, E. Rabani, and R. Baer, *Acc. Chem. Res.* **39**, 109 (2006).
- [20] B. Kudisch, et al., *Proc. Nalt. Am. Sci. U.S.A.* **117**, 11289 (2020).
- [21] D. Rai, H. Joshi, A. D. Kulkarni, S. P. Gejji, and R. K. Pathak, *J. Phys. Chem. A* **111**, 9111 (2007).
- [22] T. Lu and Q. Chen, *Chem. Phys. Chem.* **22**, 386 (2021).
- [23] C. Lu, F. Jiang, and J. Wang, *Mater. Res. Express*, **9**, 064001 (2022).
- [24] X. Wu and D. Ren, *Molecules*, **22**, 1714 (2022).
- [25] T. Yaping, S. Mingzhu, X. Renyong, A. Jinfan, and Z. Weiying, *J. Phys. Org. Chem.* **36**, e4554 (2023).
- [26] Z. Yan, et. al., *Sci. Adv.* **8**, eamb3541 (2022).
- [27] K. J. Lozano, R. Santiago, J. R. -Arino, and S. T. Bromley, *Phys. Chem. Chem. Phys.* **23**, 3844 (2021).
- [28] Y. C. Choi, C. Pak, and K. S. Kim, *J. Chem. Phys.* **124**, 094308 (2006).

- [29] D. Rai, A. D. Kulkarni, S. P. Gejji, and R. K. Pathak, *J. Chem. Phys.* **128**, 034310 (2008).
- [30] D. Rai, A. D. Kulkarni, S. P. Gejji, and R. K. Pathak, *J. Chem. Phys.* **135**, 024307 (2011).
- [31] H. Sabzyan and M. Kowsar, *Phys. Chem. Chem. Phys.* **19**, 12384 (2017).
- [32] Z. G. Chiragwandi, O. Nur, M. Willander, and N. Calander, *App. Phys. Lett.* **85**, 5310 (2003).
- [33] R. E. Jacobsen, S. Arslanagic and A. V. Lavrinenko, *Appl. Phys. Rev.* **8**, 041304 (2021).
- [34] Y. Lu, et al., *Research (Wash DC)* 7505638 (2021).
- [35] A. Buchmann, C. Hoberg, and F. Novelli, *APL Photonics*, **7**, 121302 (2022).
- [36] S. Melnik, A. Ryzhov, A. Kiselev, A. Radenovic, T. Weil, K. J. Stevenson, and V. G. Artemov, *J. Phys. Chem. Lett.* **14**, 6572 (2023).
- [37] J. Chen, Z. Wang, Z. Deng, L. Chen, X. Wu, Y. Gao, Y. Hu, M. Li and H. Wang, *Front. Chem.* **11**, 1200644 (2023).
- [38] L. Zhao, K. Ma, and Z. Yang, *Int. J. Mol. Sci.* **16**, 8489 (2015).
- [39] Y. Gao, M. Li, C. Zhan, H. Zhang, M. Yin, W. Lu, and B. Xu, *Adv. Mater.* **35**, 2303759 (2023).
- [40] G. Cassone, P. V. Giaquinta, F. Saija and A. M. Saitta, *J. Phys. Chem. B* **118**, 4419 (2014).
- [41] N. H. Vu, H. C. Dong, M. V. Nguyen, D. Hoang, T. T. Trinh and T. B. Phan, *Curr. Appl. Phys.* **25**, 62 (2021).
- [42] G. Cassone, *J. Phys. Chem. Lett.* **11**, 8983 (2020).

- [43] K. Ritos, M. K. Borg, N. J. Mottram and J. M. Reese, *Phil. Trans. R. Soc. A* **374**, 20150025 (2015).
- [44] J. A. Garate, N.J . English and J. M. D. MacElroy, *Mol. Simul.* **35**, 3 (2009).
- [45] D. N. de Freitas, B. H. S. Mendonça, M. H. Köhler, M. C. Barbosa, M. J. S. Matos, R. J. C. Batista, and A.B. de Oliveira, *Chem. Phys.* **537**, 110849 (2020).
- [46] C. Duan, W. Wang and Q. Xie, *Biomicrofluidics*, **7**, 026501 (2013).
- [47] H. Zhou, W. Li and P. Yu, *ChemistryOpen*, **11**, e202200126 (2022).
- [48] T. Sun, S. Xu, D. Xiao, Z. Liu, G. Li, A. Zheng, W. Liu, Z. Xu, Y. Cao, Q. Guo, N. Wang, Y. Wei, and Z. Liu, *Angew. Chem. Int. Ed.* **59**, 20672 (2020).
- [49] U. T. -Herrera, M. F. B. -Rivas, V. V. -Guerrero and J. Balmaseda, *Transp. Porous Med.* **149**, 479 (2023).
- [50] Y. Hong, J. Zhang, C. Zhu, X. C. Zeng, and J. S. Francisco, *J. Mater. Chem. A* **7**, 3583 (2019).
- [51] L.-B. Huang, et al., *J. Am. Chem. Soc.* **143**, 4224 (2021).
- [52] Y. Bai, H. -M. He, Y. Li, Z. -R. Li, Z. -J. Zhou, J. - J. Wang, D. Wu, W. Chen, F. -L. Gu, B. G. Sumpter, and J. Huang, *J. Phys. Chem. A* **119**, 2083 (2015).
- [53] M. Karahka and H. J. Kreuzer, *Phys. Chem. Chem. Phys.* **13**, 11027 (2011).
- [54] B. Reischl, J. Köfinger and C. Dellago, *Mol. Phys.* **107**, 495 (2009).
- [55] B. Peng, L. -X. Zheng, P. -Y. Wang, J. -F. Zhou, M. Ding, H. -D. Sun, B. -Q. Shan, and K. Zhang, *Front. Chem.* **9**, 756993 (2021).

- [56] P. S. Lakshminarayanan, E. Suresh and P. Ghosh, *J. Am. Chem. Soc.* **127**, 13132 (2005).
- [57] X. Chen. *J. Biol. Phys.* **39**, 607 (2013).
- [58] L. Wang, Z. -L. Gong, S. -Y. Li, W. Hong, Y. -Wu. Zhong, D. Wang, and L. -J. Wan, *Angew. Chem. Int. Ed.* **55**, 12397 (2016).
- [59] R. Fukuzumi, S. Kaneko, S. Fujii, T. Nishino, and M. Kiguchi, *J. Am. Chem. Soc.* **122**, 4698 (2018).
- [60] L. Xiang, et al., *Matter*, **3**, 166 (2020).
- [61] J. -H. Fang, Z. -H. Zhao, A. -X. Li, and L. Wang, *Chin. J. Chem.* **41**, 3433 (2023).
- [62] T. Nishino, N. Hayashi and P.T. Bui, *J. Am. Chem. Soc.* **135**, 4592 (2013).
- [63] M. Wimmer, J. L. Palma, P. Tarakeshwar and V. Mujica, *J. Phys. Chem. Lett.* **7**, 2977 (2016).
- [64] M. Kula, J. Jiang, W. Lu, and Y. Luo, *J. Chem. Phys.* **125**, 194703 (2006).
- [65] D. P. Long, et al., *Nat. Mater.* **5**, 901 (2006).
- [66] S. Nakashima, Y. Takahashi, and M. Kiguchi, *Beilstein J. Nanotechnol.* **2**, 755 (2011).
- [67] Z. -L. Li, X. -H. Yi, R. Liu, J. -J. Bi, H. -Y. Fu, G. -P. Zhang, Y. -Z. Song, and C. -K. Wang, *Sci. Rep.* **7**, 4195 (2017).
- [68] D. Rai, O. Hod, and A. Nitzan, *J. Phys. Chem. C* **114**, 20583 (2010).
- [69] D. Rai, O. Hod, and A. Nitzan, *Phys. Rev. B* **85**, 155440 (2012).
- [70] H. Li, T. A. Su, V. Zhang, M. L. Steigerwald, C. Nuckolls, and L. Venkataraman, *J. Am. Chem. Soc.* **137**, 5028 (2015).
- [71] U. Dhakal and D. Rai, *J. Phys.: Condens. Matter*, **31**, 125302 (2019).

- [72] S. Tanimoto, M. Tsutsui, K. Yokota, and M. Taniguchi, *Nanoscale Horiz.* **1**, 399 (2016).
- [73] V. M. -Grošev, K. Furić, and V. Vujnović, *Spectrochim Acta A Mol Biomol Spectrosc.* **269**, 120770 (2022).
- [74] M.J. Frisch, et al., Gaussian 16, Revision C.01 (Gaussian, Inc., Wallingford, CT, 2016).
- [75] J. -D. Chai and M. H. -Gordon, *Phys. Chem. Chem. Phys.* **18**, 6615 (2008).
- [76] S. -W. Cheng and H.-F. Cheung, *J. Appl. Phys.* **94**, 1190 (2003).
- [77] G. M. Shedd and P. E. Russell, *Nanotechnology*, **1**, 67 (1990).
- [78] S. Kondo, S. Heike, M. Lutwyche, and Y. Wada, *J. Appl. Phys.* **78**, 155 (1995).
- [79] Ph. Avouris, R. Martel, T. Hertel, and R. Sandstrom, *Appl. Phys. A* **66**, S659 (1998).
- [80] R. Nemetudi, N. J. Curson, N. J. Appleyard, D. A. Ritchie, and G. A. C. Jones, *Microelectron. Eng.* **57**, 967 (2001).
- [81] X. N. Xie, H. J. Chung, C. H. Sow, and A. T. S. Wee, *Mater. Sci. Eng. R* **54**, 1 (2006).
- [82] L. Infantes and S. Motherwell, *CrystEngComm.* **4**, 454 (2002)
- [83] W. Klopper, J. G. C. M. van Duijneveldt-van de Rijdt and F. B. van Duijneveldt, *Phys. Chem. Chem. Phys.* **2**, 2227 (2000).
- [84] Y. Tao and E. Kraka, *J. Chem. Theory Comput.*, **18**, 562 (2022).
- [85] L. Yang, H. Ji, X. Liu and W.C. Lu, *ChemistryOpen.* **9**, 210 (2019).
- [86] L. E. Seijas, C. H. Zambrano, R. Almeida, J. Alí-Torres, L. Rincón and F.J. Torres, *Int. J. Mol. Sci.* **24**, 5271 (2023).

- [87] V. C. Nibali, S. Maiti, F. Saija, M. Heyden and G. Cassone, *J. Chem. Phys.* **158**, 184501 (2023).
- [88] F. Li, L. Wang, J. Zhao and J. R. -H. Xie, K. E. Riley and Z. Chen, *Theor. Chem. Acc.* **130**, 341 (2011).
- [89] E. S. Soldatov, S. P. Gubin, I. A. Maximov, G. B. Khomutov, V. V. Kolesov, A. N. S. -Cherenkov, V. V. Shorokhov, K. S. Sulaimankulov, and D. B. Suyatin, *Microelectron. Eng.* **69**, 536 (2003).
- [90] S. Gunasekaran, D. A. Reed, D. W. Paley, A. K. Bartholomew, L. Venkataraman, M. L. Steigerwald, X. Roy, and C. Nuckolls, *J. Am. Chem. Soc.* **142**, 14924 (2020).
- [91] A. Vegiri, *Pure Appl. Chem.* **76**, 215 (2004).
- [92] L. R. C. Wang, H. J. Kreuzer and O. Nishikawa, *Org. Electron.* **7**, 99 (2006).
- [93] A. A. Kananenka and J. L. Skinner, *J. Chem. Phys.* **148**, 244107 (2018).
- [94] J. H. Bertie and Z. Lan, *Appl. Spectrosc.* **50**, 1047 (1996).
- [95] P. Bour, *Chem. Phys. Lett.* **365**, 82 (2002).
- [96] A. B. McCoy, *J. Phys. Chem. B.* **118**, 8286 (2014).
- [97] G. Cassone, J. Sponer, S. Trusso and F. Saija, *Phys. Chem. Chem. Phys.* **21**, 21205 (2019).
- [98] T. Seki, K. -Y. Chiang, C. -C. Yu, X. Yu, M. Okuno, J. Hunger, Y. Nagata, and M. Bonn, *J. Phys. Chem. Lett.* **11**, 8459 (2020).
- [99] C. -C. Yu, M. Okuno, T. Seki, T. Ohto, X. Yu, V. Korepanov, H. -O. Hamaguchi, M. Bonn, J. Hunger, and Y. Nagata, *Nat. Commun.* **11**, 5977 (2020).
- [100] Q. Sun and H. Zheng, *Prog. Nat. Sci.* **19**, 1651 (2009).

- [101] G. R. Medders and F. Paesani, *J. Chem. Theory Comput.* **11**, 1145 (2015).
- [102] Q. Sun, *J. Chem. Phys.* **132**, 054507 (2010).
- [103] Q. Hu, X. Lü, W. Lu, Y. Chen and H. Liu, *J. Mol. Spectrosc.* **292**, 23 (2013).
- [104] S. R. Pattenaude, L. M. Streacker, and D. B. -Amotz, *J. Raman Spectr.* **49**, 1860 (2018).
- [105] B. Wang, W. Jiang, Y. Gao, Z. Zhang, C. Sun, F. Liu and Z. Wang, *RSC Adv.* **7**, 11680 (2017).
- [106] T. Morawietx, A. S. Urbina, P. K. Wise, X. Wu, W. Lu, D. Ben-Amotz and T. E. Markland, *J. Phys. Chem. Lett.* **10**, 6067 (2019).
- [107] Q. Ferreira, C. L. Delfino, J. Morgado, and L. Alcácer, *Materials.* **12**, 382 (2019).
- [108] B. Ramsauer, G. J. Simpson, J. J. Cartus, A. Jeindl, V. García-López, J. M. Tour, L. Grill and O.T. Hofmann, *J. Phys. Chem. A.* **127**, 2041 (2023).
- [109] S. Ghosh and S. Wategaonkar, *J. Phys. Chem. A.* **123**, 3851 (2019).
- [110] L. Ge, S. Hou, Y. Chen, Q. Wu, L. Long, X. Yang, Y. Ji, L. Lin, G. Xue, J. Liu, X. Liu, C. J. Lambert, W. Hong and Y. Zheng, *Chem. Sci.* **13**, 9552 (2022).
- [111] L. Wang, Z. Gong, S. Li, W. Hong, Y. Zhong, D. Wang, and L. Wan, *Angew. Chem. Int. Ed.* **55**, 12393 (2016).
- [112] J. Chen, Z. Wang, Z. Deng, L. Chen, X. Wu, Y. Gao, Y. Hu, M. Li and H. Wang, *Front. Chem.* **11**, 1200644 (2023).
- [113] M. Li, H. Fu, B. Wang, J. Cheng, W. Hu, B. Yin, P. Peng, S. Zhou, X. Gao, C. Jia, and X. Guo, *J. Am. Chem. Soc.* **144**, 20797 (2022).

- [114] A. G. C. Zhou, R. T. W. Popoff, L. Zhu, and H. -Z. Yu, *J. Phys. Chem. C* **127**, 2471 (2023).
- [115] A. Olejnik, B. Dec, W. A. Goddard and R. Bogdanowicz, *J. Phys. Chem. Lett.* **13**, 7972 (2022).
- [116] Z. Xue, F. Gan, H. Liu, C. Shen, H. Qiu, B. Yang and P. Yu, *CCS Chem.* **4**, 1405 (2022).
- [117] X. Shi and W. Bao, *Front. Chem.* **9**, 723718 (2021).
- [118] L. Chen, J. Xu, M. Zhu, Z. Zeng, Y. Song, Y. Zhang, X. Zhang, Y. Deng, R. Xiong, and C. Huang, *Mater. Horiz* **10**, 4000 (2023).
- [119] H. Elgabrty, T. Kampfrath, D. J. Bonthuis, V. Balos, N. K. Kaliannan, P. Loche, R. R. Netz, M. Wolf, T. D. Kühne, and M. Sajadi, *Sci. Adv.* **6**, eaay7074 (2020).
- [120] C. X. Kronawitter, C. Riplinger, X. He, P. Zahl, E. A. Carter, P. Sutter, and B. E. Koel, *J. Am. Chem. Soc.* **136**, 13283 (2014).
- [121] H. Okuyama and I. Hamada, *J. Phys. D: Appl. Phys.* **44**, 464004 (2011).
- [122] J. Guo, K. Bian, Z. Lin and Y. Jiang, *J. Chem. Phys.* **145**, 160901 (2016).
- [123] L. Zhao, M. Tao, K. Sun, Y. Tu, D. Yang, Z. Wang, M. Shi and J. Wang, *Appl. Surf. Sci.* **515**, 145973 (2020).
- [124] K. Johnson, *Int. J. Astrobiology.* **20**, 111 (2021).

Chapter4

Electric Field Response of a Molecule Nanoconfined in Molecular Cages[†]

Abstract

We take into consideration a water molecule confined in the covalently bonded small-size fullerenes and a carbon monoxide confined in the hydrogen-bonded building blocks of the sI and sII clathrate hydrates. Such nanoscopic molecular cages provide an ideal setup to study their characteristic properties not present in the condensed phase. We study their response to the applied electric fields in terms of change in geometrical parameters, dipole moment, HOMO-LUMO gap, and vibrational frequency shift. The electric field shielding property of small-size fullerene cages is explored and results that hold significance for technological applications are discussed. Likewise, the stability of CO clathrate hydrate building block cages is examined, and potential signs of field-induced controlled release of CO are succinctly discussed.

[†]This chapter is based on research articles under preparation:
Smita Rai and Dhurba Rai, (i) “*Electric field response of a water molecule confined in small carbon nanocages*”, and (ii) “*Electric field influence on CO clathrate hydrates*”.

4.1 Background

As elucidated in Chapter 1, molecules in confinement offer an invaluable opportunity to investigate novel properties of molecules that are otherwise obscured when they are in bulk [1–4]. Undoubtedly, molecular confinement has emerged as a potent tactic for unlocking new aspects of molecules [5, 6]. One of the most studied confinements from the perspective of potential device applications is a water molecule trapped inside C_{60} fullerene molecule [7]. Fullerenes are carbon molecular cages known to exist in a variety of shapes and sizes [8], and are found everywhere from combustion flame soot [9] to deep in the interstellar space [10]. The C_{60} fullerene is a nonpolar molecule having a spherical cavity approximately 7 Å in diameter, providing sufficient space for atoms and molecules or small molecular clusters [11] to dwell in, however, imprisoning a molecule inside a nanoscopic molecular cavity is experimentally challenging that involves opening of cage through controlled chemical reactions followed by insertion of the guest molecule and reclosure [12, 13]. One such effort due to Kurotobi and Murata [7, 14], and a subsequent endeavor [15], have led to the confinement of a water molecule inside the C_{60} cage. Since then, a great deal of research, both theoretical and experimental, has been carried out to examine the characteristics of confined water for prospective device applications [16–19]. Additionally, investigations [18, 19] have been carried out to understand the characteristic way the confined water molecule modulates the properties of the confining cage, which makes it possible for molecular electronics devices to use the controlled features of the molecular cage, thereby broadening device functionalities.

A striking effect of confining a water molecule inside a C_{60} cage is the significant reduction of electric dipole moment of the water molecule as indicated by smaller polarity of the $H_2O@C_{60}$ system, which can be understood (or, may involve a more complex mechanism) as due to polarization of the cavity wall by the confined water molecule, counteracting the electron distribution in the water molecule

that results in a much lower dipole moment. This raises the possibility that the confined molecule and the encapsulating cage are not electrically isolated. Significant interactions between the confined H_2O and the C_{60} cage have been found by the atoms in molecules (AIM) analysis at the PBE0/6-311++G(d,p) level of DFT calculations [20]. Although the results, e.g., small dipole moment and downshift of O-H stretching vibrational frequencies, are in conformity with the other DFT-based and perturbative calculations [21–23], which however, strongly disagree with the DFT-based molecular dynamics (MD) simulations employing the BLYP-D functional [24] and the DFT calculations employing the M062X functional [14] that estimate the dipole moment of $\text{H}_2\text{O}@\text{C}_{60} \sim 2.0$ Debye, which is comparable to that of an isolated water molecule, i.e., 1.84 Debye. The latter results are in agreement with a UV/Vis spectroscopy study that shows no observable electronic interaction between the confined H_2O and C_{60} cage, and imply the polar nature of $\text{H}_2\text{O}@\text{C}_{60}$ based on the ease of chromatographic separation of $\text{H}_2\text{O}@\text{C}_{60}$ as opposed to C_{60} [15]. Also, a recent study based on scanning tunneling microscopy (STM), non-contact atomic force microscopy (ncAFM) and photoemission spectroscopy determine that the confined water molecule does not contribute to the C_{60} frontier orbitals, indicating no influence on the dipole moment of the water molecule by the encapsulating C_{60} cage [25]. However, the dipole moment estimated from the high-temperature measurement of the molecular polarizability of $\text{H}_2\text{O}@\text{C}_{60}$ is found to be 0.5 ± 0.1 D [26]. Furthermore, a recent infrared absorption spectroscopy study of rotational line intensities of $\text{H}_2\text{O}@\text{C}_{60}$ system determines the dipole moment to be 0.50 ± 0.05 D [27]. Thus, careful, in-depth investigations are deemed necessary to resolve the perplexing issue of the polarity of $\text{H}_2\text{O}@\text{C}_{60}$ system.

Of particular interest to us are water molecules in extreme geometric confinement, such as those confined in small fullerenes (C_n , $n < 60$). Such a situation, somewhat similar to high-pressure conditions, may be prevalent in the clathrate formation, which is frozen crystalline water at low temperature but extremely high pressure. This will be discussed shortly, but for now, we take a

moment to consider the significance of small fullerene cages, which are usually highly strained, unstable and very reactive. Breaking the barrier of otherwise exclusive focus dedicated to the theoretical domain [28–30], significant progress has been made in observing stable small fullerene cages by encapsulating metal atoms like Ti, Zr and U [31, 32]. Numerous studies have also demonstrated that the small fullerenes exhibit unique characteristics distinct from those of their larger counterparts and that these characteristics may hold technological relevance in molecular electronic devices, such as Fe@C₂₈ molecular junction, which acts as an efficient spin filter device [33] and Cr@C₂₈ molecular junction as a device for high-density data storage applications [34]. One subtle issue, not much discussed in the literature [35], is the shallow potential energy surface (PES) of H₂O@C₆₀ due to spherical symmetric geometry, while the confined water molecule does not cause distortion due to weak interactions with the larger cavity wall. This makes it difficult to find the true local energy minimum structure characterized by all real vibrational frequencies. Applying an electric field also causes the system to rapidly deviate from the PES’s local energy minimum. This is not the case, however, for the small fullerenes, which are distorted spheres. Because of their small size and the significant interaction that the confined water molecule has with the cavity wall, the PES is distorted with discernible features that make it easy to locate the true local energy minimum structure. This validates our choice for small fullerenes over C₆₀, which are ideal for our study on the response of a water molecule to an external field under extreme geometric confinement.

Concerning nanoconfined molecules in molecular cages, clathrates are natural room for the confinement of gas molecules. Clathrates (also known as clathrate hydrates or gas hydrates) are crystalline water-based solids resembling ice with cage-like lattices of water molecules that enclose different gas molecules [36, 37]. Clathrates are studied in relation to the confinement of molecules, such as CH₄, CO₂, N₂, O₂, etc. In particular, methane clathrates are found naturally in large quantities in the polar permafrost regions where the ground temperature stays below 0°C and beneath the deep ocean sediments [38, 39]. They are

also commonly formed during the natural gas and petroleum extraction process when liquid water condenses at high pressure in the presence of methane. When clathrates are formed, they clog the pipelines and processing equipment, thereby severely slowing down the transportation and production processes in the oil and gas industries [40, 41]. The formation of clathrates also possesses serious safety risks as when the pressure is reduced or temperature is increased, clathrates undergo a phase transition from the solid to the liquid-gas mixture, releasing gaseous methane at a high rate [42]. However, interest in methane clathrate research has now shifted from understanding the mechanism that inhibits its formation to extracting methane itself, realizing that methane clathrate is a promising alternative energy source for the future [43, 44].

On a molecular scale, the frozen polyhedral water cages are stabilized by hydrogen-bonding (H-bonding) interaction between the water molecules holding the cages together and the van der Waals (vdW) interaction between the enclosed molecule and the water molecules, resulting a crystalline structure that is more stable than hexagonal ice. Clathrates naturally adopt three structures, viz., cubic sI and sII and hexagonal sH, distinguishing from one another depending on the size and type of cages and their periodic crystal structure [45]. A unit cell of sI lattice structure of clathrate consists of 46 water molecules in a framework of two sets of building block cages, viz., two pentagonal dodecahedron cages, i.e., 5^{12} structure consisting of 12 pentagonal faces and, six tetrakaidecahedron cages, i.e., $5^{12}6^2$ structure consisting of 12 pentagonal and 2 hexagonal faces. Other combinations of such building block cages result in sII and sH clathrate structures as shown in Fig. 4.1. Owing to the flexibility of H-bonds, clathrates can undergo structural phase transitions with changes in thermodynamic conditions (pressure and temperature) or possibly even coexist in mixed phases. The enormous potential for technological applications of clathrates stems from the inherent ability to tailor their molecular scale properties under various thermodynamic conditions. Among others, clathrates hold great promise for application in hydrogen storage and as an alternative energy source, however, the adverse thermodynamic conditions impede

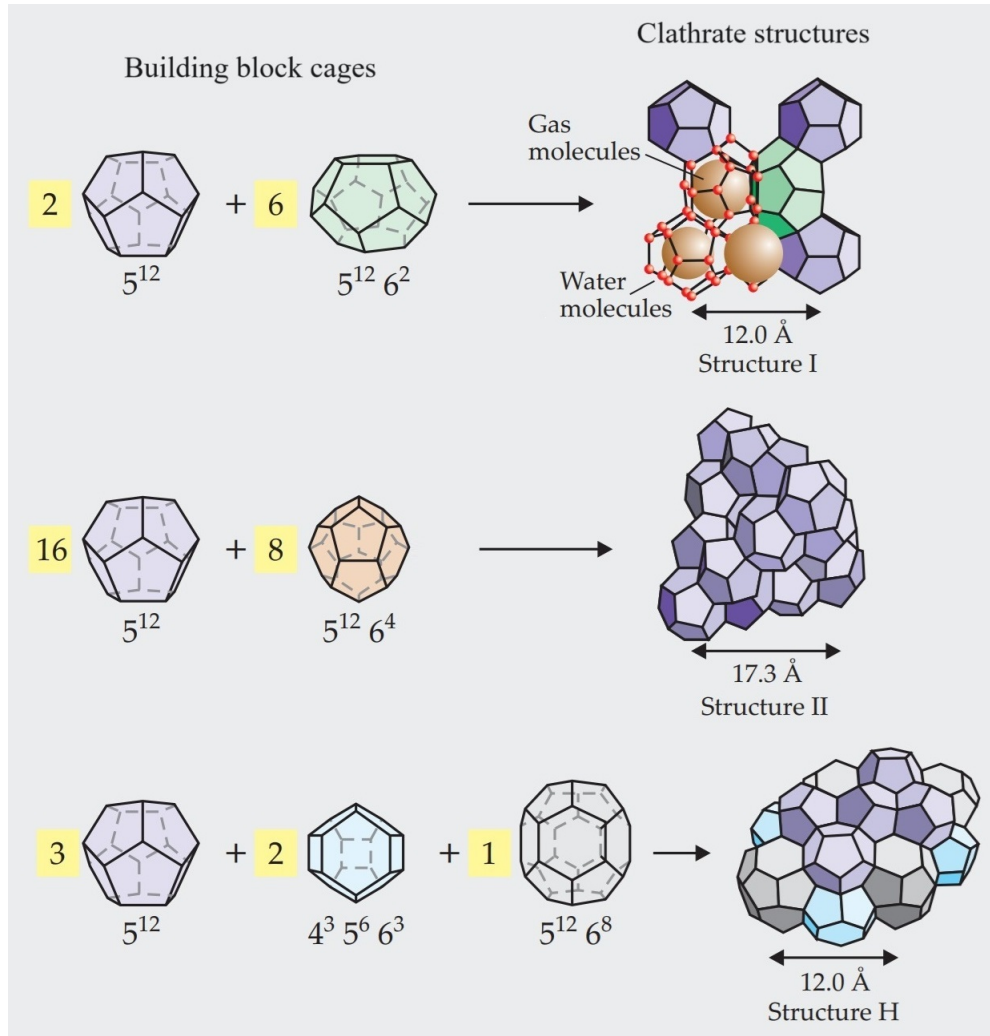


FIGURE 4.1: Five building block cages (5^{12} , $5^{12}6^2$, $5^{12}6^4$, $5^{12}6^8$, and $4^35^66^3$) that make up the three common clathrate structures, sI, sII and sH [46].

their practical applications. It was found that the hydrogen storage capacity of sI and sII clathrate at 70 MPa and 263K is only 0.02 and 0.31 wt%, respectively [47]. These values of storage capacity are significantly less than the U.S. Department of Energy's standard for commercial practical applications, which is set at 6.5 wt% for the operational temperature in the range 333-393K. Therefore, an extensive search for an alternative to temperature and pressure that affect the characteristics of clathrates on a molecular scale is crucial in order to bring clathrates in technological applications closer to reality. Additionally, exploring the characteristic properties of the building block cages may facilitate understanding the bulk property of clathrates.

Of special importance to us is carbon monoxide (CO) clathrate hydrate. While carbon monoxide exists in abundance in the cosmos (gaseous nebulae, interstellar medium, other planets' atmosphere, comet's ice etc.), possibly in clathrate form [48], whereas on Earth it is primarily found in gaseous form, chiefly emanating from the industrial and human activities. The X-ray diffraction study reveals that CO clathrate hydrate has sI structure with a lattice constant of 11.88 Å and crystallization takes place at 17.3 MPa and 243K [49], with the latter finding also supported by a neutron diffraction experiment [50]. Remarkably, it has been found that CO clathrate hydrate initially forms in the kinetically preferred sI structure and then transforms into the thermodynamically stable sII structure [50]. In the recent past, isolated building block cages have been taken into consideration in theoretical investigations of the CO clathrate hydrate based on the MD simulations and DFT calculations to characterize the sI type (5^{12} and $5^{12}6^2$) and sII type (5^{12} and $5^{12}6^4$) clathrate structures [50, 51]. Further insights into the circumstances governing the stability of one structure over another have been obtained from a more comprehensive combination of DFT-based and neutron diffraction investigations that took into account the entire clathrate unit cell (sI and sII) [52]. It would be interesting to study how an external electric field influences the H-bonded building block cages of the clathrates with a CO molecule confined inside. This is crucial in understanding if the electric field can regulate the capture and release of CO for specific applications.

4.2 Scope of the Work

In this chapter, we study the response of a water molecule to an external electric field when it is confined in small-sized fullerenes such as C_{28} , C_{30} , and C_{32} . We examine their stability, electronic structure, dipole screening, and vibrational spectra when subjected to external field application, thereby identifying any characteristics pertinent to device applications. Given the small size of the confining

cage, it would be interesting to see what new effects the water molecule would exhibit when subjected to extreme confinement. In keeping with this, a very recent study using MD simulations has shown that the fusion of H_2O and H_2 inside the small-sized fullerenes (C_{24} , C_{26} , C_{28} , and C_{30}) results in the synthesis of hyper-hydrogenated water species H_4O [53]. This demonstrates the ability of the small fullerenes to operate as nanoreactors for unforeseen reactions that would not otherwise be possible in bulk or free space. Also, recent DFT calculations at the M06-2X/6-31++G(d,p) level of theory demonstrated O-O covalent bonding between the two water molecules when confined inside C_{36} fullerene [54]. This is reminiscent of field-induced C-O covalent bonding between H_2O and CO_2 [55].

From the perspective of molecular device application, C_{28} fullerene with caged atoms (Fe, Cr) has been shown to function as an efficient spin filter for spin transport in spintronics [33] and as a data storage device for future high-density miniaturized circuits [34]. It is specifically hoped that, due to the small size of the confining cage, the electric dipole of $\text{H}_2\text{O} @ (\text{C}_{28}, \text{C}_{30}, \text{C}_{32})$ can be modulated more effectively than that of $\text{H}_2\text{O} @ (\text{C}_{60})$, which could result in a potential switching device with characteristic hysteresis and negative differential conductance (NDC) features, as has been observed for $\text{Tb} @ \text{C}_{82}$ in a low-temperature STM junction setup [56]. These characteristics are found to be caused by molecular orientation in response to the interaction between its electric dipole moment and an external electric field. Therefore, it is crucial to investigate the electric field response of $\text{H}_2\text{O} @ (\text{C}_{28}, \text{C}_{30}, \text{C}_{32})$ that would be useful in the design of molecular devices based on small-sized fullerenes that take advantage of the properties of a water molecule contained within them.

We also consider CO confined inside 5^{12} , $5^{12}6^2$ and $5^{12}6^4$ molecular cages and examine its response to the external electric field in terms of the frequency shift of the CO stretching mode in the vibrational spectrum. The stability of the three building block cages ($\text{CO} @ 5^{12}$, $\text{CO} @ 5^{12}6^2$, $\text{CO} @ 5^{12}6^4$), and the field influence on the structure and the factors dictating physico-chemical properties, are examined.

Any characteristic indicative of field-induced CO release or trapping in the cage structures will be identified and discussed.

While we focus on the individual building block cages, investigating their response to the applied electric field may provide alternative strategies for exploring novel aspects of the CO clathrate hydrates. The tremendous potential for technological applications of the electric field-induced uptake and release of gas molecules from clathrate hydrates have spurred a great deal of theoretical [57–60] and experimental research [61, 62]. It was found that applying an electric field 0.07 V/Å reduced the energy barrier for neon release in a sII clathrate hydrate from 16.4 kJ/mol to 6.5 kJ/mol [59]. At the molecular level, an electric field is what causes the water dipoles to orient along the field direction, which becomes so important at high fields, thereby causing the clathrate’s H-bond network to sufficiently disrupt or break to release the trapped gas molecules. This is investigated in relation to CO clathrate hydrate considering building block cages (CO@5¹², CO@5¹²6², CO@5¹²6⁴) in the presence of the field. This study could provide insights into the controlled release of CO at a specific site in order to host an atomically precise and selective reaction in a constrained environment or space. Undoubtedly, this helps in the atomically precise fabrication and miniaturization of electronic devices [63], which can be considered as a precursor towards the ultimate development of full-scale molecular electronics.

4.3 Methodology and Computational Details

Since we consider cage structures that are covalently bonded as well as H-bonded that confine water and carbon monoxide molecules, respectively, so the types and range of interactions involved differ from one another. Consequently, we employ different functionals appropriate for each system and results are compared while maintaining the usage of the same basis set for all calculations. It is to be noted, though the sizes of the covalently bonded small fullerenes and H-bonded building

block cages of clathrates under consideration differ, they can be viewed as the covalent and hydrogen bond counterparts of one another for comparison purposes in terms of the response of the molecule they confined to the external field.

For a given cage, we consider the energy minimum structure and reoptimized the structure at the same Pople’s basis set, 6-311++G(d,p), using different XC functionals, viz., B3LYP, PBE0, B97-D, ω B97X-D and M06-2X, thereby ensuring that the true local energy minimum structure for all vibrational frequencies are real. Results are then compared with the experimental and decent computational data available in the literature. However, when the electric field is applied in the molecular cages confining a molecule, calculations are carried out at a single functional. The choice for a certain functional is determined by its intrinsic design and the kind of interaction that may exist in the cage system. For the $\text{H}_2\text{O}@\text{(C}_{28}, \text{C}_{30}, \text{C}_{32})$ cages, we consider M06-2X functional as it offers a significant improvement over the conventional functionals (B3LYP, PBE0) and empirically added dispersion corrected functionals, such as B97-D. While the fullerenes considered are much smaller than C_{60} , we believe insignificant long-range dispersion interactions in the $\text{H}_2\text{O}@\text{(C}_{28}, \text{C}_{30}, \text{C}_{32})$ cages, and thus, the M06-2X functional is employed that implicitly takes a balanced account of the short- and medium-range electron correlations, and incorporates as well, the medium-range dispersion-like interactions. On the other hand, in the case of $\text{CO}@\text{(5}^{12}, \text{5}^{12}\text{6}^2, \text{5}^{12}\text{6}^4)$ cages, the dominant interaction is H-bonding that defines the cage structure stabilized by dispersion interactions between the CO and cage wall. Given that the $\text{CO}@\text{5}^{12}$ cage is substantially larger than C_{60} , the long-range dispersion interactions cannot be neglected. Because the ω B97X-D functional also accounts for long-range dispersion interactions, we have chosen ω B97X-D functional over the M06-2X.

As before, fields are applied along the direction of the dipole moment of the system and geometry is optimized at each field value and the vibrational frequencies are calculated. We consider static and uniform fields in the range (0-0.020 a.u.), i.e., (0-1.02 V/Å), and the field is increased in steps of 0.001 a.u.

(≈ 51.42 mV/Å). In no case, we consider the field well over 1 V/Å that could disintegrate the system. All of the calculations presented in the next section correspond to local energy minimum structures that are identified by vibrational frequencies, all real.

4.4 Computed Results and Discussion

We now present the results concerning the response of polar molecules confined in covalent as well as H-bonded molecular cages. Unless otherwise stated, the results for the $\text{H}_2\text{O}@\text{(C}_{28}, \text{C}_{30}, \text{C}_{32})$ and $\text{CO}@(5^{12}, 5^{12}6^2, 5^{12}6^4)$ cages are obtained from calculations carried out at the M06-2X/6-311++G(d,p) and $\omega\text{B97X-D}/6\text{-}311++\text{G(d,p)}$ levels, respectively. We first present and discuss the results for $\text{H}_2\text{O}@\text{(C}_{28}, \text{C}_{30}, \text{C}_{32})$ cages, and then for $\text{CO}@(5^{12}, 5^{12}6^2, 5^{12}6^4)$ cages, followed by general concluding remarks encompassing both.

4.4.1 $\text{H}_2\text{O}@\text{(C}_{28}, \text{C}_{30}, \text{C}_{32})$ cages

The geometries of the $(\text{C}_{28}, \text{C}_{30}, \text{C}_{32})$ cages were taken from the fullerene structure library created by Yoshida [64]. Among several possible conformers for small-size fullerenes (nearly isoenergetic in some cases), we consider the minimum energy conformer for each structure and re-optimize the geometry at the M06-2X/6-311++G(d,p) level of theory. The minimum energy empty $(\text{C}_{28}, \text{C}_{30}, \text{C}_{32})$ cages possess (T_d, C_{2V}, D_3) symmetry, respectively. The radii of the empty cages are determined by considering the carbon atoms of the optimized structures on the surface of a sphere. Water molecule is then inserted into the cage and geometry optimized for local energy minimum configuration characterized by vibrational frequencies, all real. The optimized structures are shown in shown in Fig. 4.2, while the calculated geometrical parameters are presented in Table 4.1 along with that of $\text{H}_2\text{O}@\text{C}_{60}$ and isolated H_2O for comparison, however, the optimized structure of

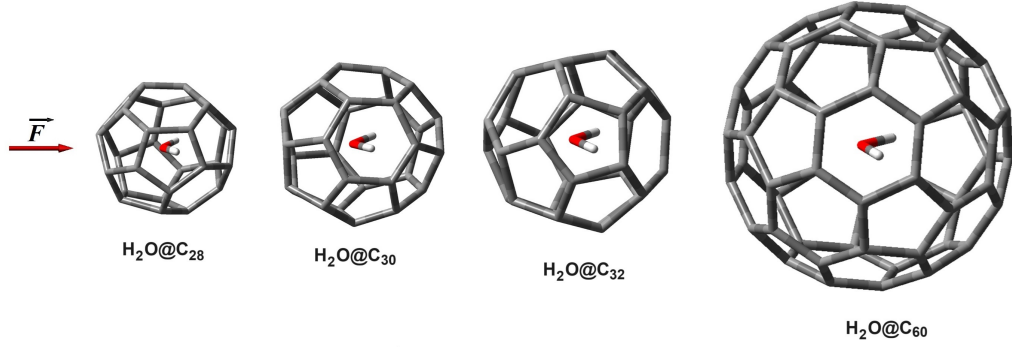


FIGURE 4.2: Optimized structures of $\text{H}_2\text{O}@\text{C}_{28}$, $\text{H}_2\text{O}@\text{C}_{30}$, $\text{H}_2\text{O}@\text{C}_{32}$, $\text{H}_2\text{O}@\text{C}_{60}$ on which electric field \vec{F} is applied along their dipole moment.

$\text{H}_2\text{O}@\text{C}_{60}$ at the M06-2X/6-311++G(d,p) level is not a true energy minimum as it has one imaginary frequency, which is indicative of a transition state structure. As discussed in the introduction chapter, owing to shallow PES of $\text{H}_2\text{O}@\text{C}_{60}$, it is often tricky to locate the true energy minimum structure. For instance, the local energy minimum structure of $\text{H}_2\text{O}@\text{C}_{60}$ at the B3LYP/cc-pVDZ + STO-3G level of theory [22] no longer remains local minimum at the B3LYP/6-311++G(d,p) level [65]. It is evident that there is a significant contraction of the O-H bond

TABLE 4.1: Geometrical parameters calculated at the M06-2X/6-311++G(d,p) level of theory.

Parameter	$\text{H}_2\text{O}@\text{C}_{28}$	$\text{H}_2\text{O}@\text{C}_{30}$	$\text{H}_2\text{O}@\text{C}_{32}$	$\text{H}_2\text{O}@\text{C}_{60}$	H_2O
Cavity radius (Å)	2.4152	2.5087	2.5983	3.5402	
OH bond length (Å)	0.9311	0.9373	0.9376	0.9692	0.9591
				0.9626 ^a	0.9576 ^b
H-O-H angle (deg.)	102.60	100.87	103.71	105.06	105.12
				104.43 ^a	104.48 ^b

^aCalculated at $\omega\text{B97X-D}/\text{aug-ccDZV}$ level with vibrational frequencies, all real.

^bExperimental value in gas phase [66].

and H-O-H angle of the water molecule upon confinement in small-size fullerenes, however, this change is minimal inside C_{60} fullerene. This is further supported by the negative value of the polarizability exaltation $\Delta\alpha$, which is calculated as the polarizability of $\text{H}_2\text{O}@\text{C}_n$ minus the sum of the polarizability of H_2O and that of empty C_n cage. This value is (-0.51, -1.74, -2.47 a.u.) for $\text{H}_2\text{O}@\text{C}_{28}$, C_{30} , C_{32} cages, respectively. The negative value of polarizability exaltation is indicative of

compression of the confined molecule [67]. Accordingly, it can be inferred that $\text{H}_2\text{O} @ (\text{C}_{28}, \text{C}_{30}, \text{C}_{32})$ cages can be regarded as extreme confinement of a water molecule, whereas $\text{H}_2\text{O} @ \text{C}_{60}$ represents fundamental confinement of a gas phase water molecule.

4.4.2 Dipole Screening

We refer “dipole screening” to a peculiar characteristic of the $\text{H}_2\text{O} @ \text{C}_{60}$ guest-host system exhibiting decreased dipole moment, which has not yet been agreed upon [7]. Given that the dipole screening is still not well understood, we examine this in the case of small-size fullerenes as well. A moment’s reflection in Table 4.2 shows reduced dipole moment of $\text{H}_2\text{O} @ (\text{C}_{28}, \text{C}_{30}, \text{C}_{32})$ cages with respect to the values for empty cages $(\text{C}_{28}, \text{C}_{30}, \text{C}_{32})$, which are (0.98, 1.18, 0) Debye, respectively, calculated at the M06-2X/6-311++G(d,p) level of theory, while it is 2.18 Debye for a water molecule, which however, is more than the experimental gas phase value of 1.84 Debye [68]. It must be noted, however, that $\text{H}_2\text{O} @ \text{C}_{32}$ and $\text{H}_2\text{O} @ \text{C}_{60}$, which were

TABLE 4.2: Dipole moment (Debye) in absence of field calculated using different functionals with the 6-311++G(d,p) basis set.

Functional	$\text{H}_2\text{O} @ \text{C}_{28}$	$\text{H}_2\text{O} @ \text{C}_{30}$	$\text{H}_2\text{O} @ \text{C}_{32}$	$\text{H}_2\text{O} @ \text{C}_{60}$
B3LYP	0.59	0.73	0.40	0.57
PBE0	0.59	0.71	0.44	0.58
B97-D	0.33	0.67	0.36	0.49
ω B97X-D	0.89	0.55	0.50	0.64
M06-2X	0.83	0.59	0.47	0.64
				0.51 ^a
				0.54 ^b

^aCalculated using the 6-311G(2d,p) basis set as used in [14].

^bCalculated in [23] for the geometry in [14] using the 6-311G(2d,p) basis set.

nonpolar in the empty state, have the lowest dipole moment. It is tempting to consider that the dipole screening is due to the polarization of the cavity wall by the confined water molecule, counteracting the electron distribution in the water molecule that results in a much lower dipole moment. However, experiments

have found that the cage and the confined water molecule are electrically isolated [15, 25]. We anticipate comprehensive, in-depth and dedicated studies on the issue of dipole screening, until then it remains elusive.

4.4.3 Dipole Moment and HL Gap

We now consider the field evolution of the dipole moment and HOMO-LUMO (HL) gap. As Fig. 4.3 (a) illustrates, the dipole moment increases linearly with the applied field in the range (0-0.02 a.u.). For $\text{H}_2\text{O}@\text{C}_{28}$, a slight deviation at 0.012 a.u. over an otherwise linear increase is due to the adjustment of the cage structure and the orientation of the water dipole orientation along the field direction. However, the linear response no longer holds when the field is gradually increased to larger values. The average polarizability, $\alpha = (\alpha_{xx} + \alpha_{yy} + \alpha_{zz})/3$, of

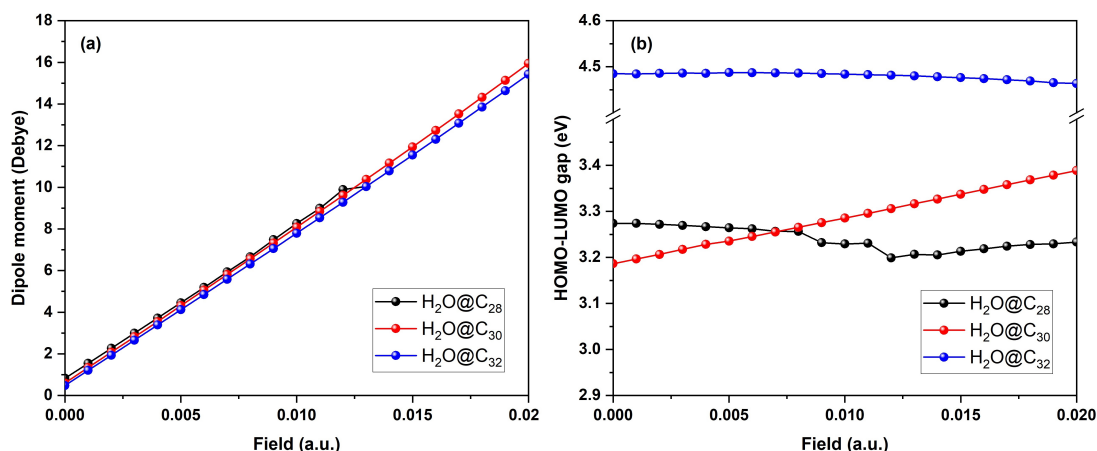


FIGURE 4.3: (a) Dipole moment and (b) HL gap of the $\text{H}_2\text{O}@\text{(C}_{28}, \text{C}_{30}, \text{C}_{32})$ cages as a function of the applied electric field in the range (0-0.02 a.u.).

the $\text{H}_2\text{O}@\text{(C}_{28}, \text{C}_{30}, \text{C}_{32})$ cages are (263.18, 278.18, 296.07) a.u., respectively (1 a.u. polarizability=0.148 Å³). As discussed in Chapter 1, polarizability reflects the molecule's ability to acquire the induced dipole moment in the external electric field \vec{F} , i.e., $\mu_i^{\text{induced}} \simeq \alpha_{ij} F_j$, within a linear response. A quick estimate shows that the dipole moment of the $\text{H}_2\text{O}@\text{(C}_{28}, \text{C}_{30}, \text{C}_{32})$ cages increases by over 0.014 Debye per mV/Å increase of applied field strength. Notably, with a typical field

of 0.65 V/Å, the induced dipole moment of the cages confining a water molecule is well over 10 Debye. This makes it a desirable feature for use in the dipole moment-based molecular devices [75].

TABLE 4.3: HL gap (eV) in absence of field calculated using different functionals with the 6-311++G(d,p) basis set.

Functional	H ₂ O	C ₆₀	H ₂ O@C ₂₈	H ₂ O@C ₃₀	H ₂ O@C ₃₂	H ₂ O@C ₆₀
B3LYP	8.19	2.72	1.45	1.52	2.66	2.68
PBE0	8.82	2.98	1.69	1.83	2.97	2.95
B97-D	6.44	1.65	0.42	0.55	1.53	1.63
ω B97X-D	12.19	5.97	4.81	4.77	5.90	5.93
M06-2X	10.74	4.48	3.27	3.18	4.48	4.44
	7.61 ^a	4.9 ^b				
		1.5 - 2.3 ^c				

^aExperimental value in gas-phase [69].

^bEstimated from experimental gas-phase ionization energy and electron affinity [70].

^cExperimental values reported in [71–74].

Relying on the calculations using the M06-2X functional (cf. Table 4.3), the HL gap is not appealing because it is over 3 eV and remains essentially unaltered or grows with field, making it outside of the range (0.5-3 eV) for any usage in optoelectronic devices. The field variation of the HL gap is shown in Fig. 4.3 (b). As discussed in the preceding chapters, the field variation of the HL gap is due to the modulation of HOMO and LUMO in the field, causing localization and delocalization. Delocalization causes a decrease in orbital energy, while localization causes a rise in energy, and the combined effect results in the overall variation of the HL gap in field [76, 77].

4.4.4 Vibrational Response to Applied Field

The response of a confined water molecule to the applied electric field can be determined from the way its vibrational modes change with the field. The field-induced effect on the vibrational modes of H₂O confined in the (C₂₈, C₃₀, C₃₂) cages are shown in Fig. 4.4. As is known that the symmetric stretch (SS) is a

slightly an easier deformation than the asymmetric stretch (AS), so the symmetric stretch occurs at a lower wavenumber than the asymmetric stretch. Likewise, bending vibration is considerably easier than stretching so this occurs at a much lower wavenumber. For instance, in C_{60} fullerene, SS (AS) occurs at 3869 (3963) cm^{-1} (calculated at $\omega\text{B97X-D/ aug-ccDZV}$ level), while in C_{32} they occur at 4142 (4163) cm^{-1} . However, a closer examination reveals that there is an interchange in the positions of the SS and AS modes in the wavenumber scale when one goes down from $\text{H}_2\text{O}@C_{60}$ or $\text{H}_2\text{O}@C_{32}$ to $\text{H}_2\text{O}@C_{30}$ and $\text{H}_2\text{O}@C_{28}$. This observation is consistent with other functionals as well, suggesting that it is an artifact of extreme geometric confinement. To our knowledge, no prior reports have been made of this observation.

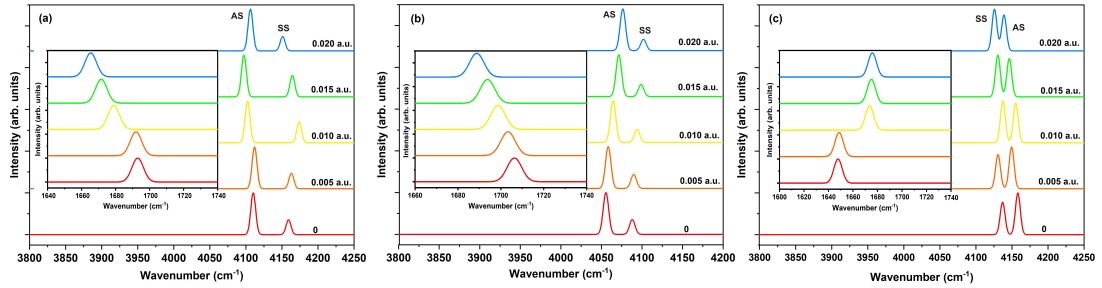


FIGURE 4.4: Comparative field evolution of O-H symmetric stretch (SS) and asymmetric stretch (AS) vibrational peaks of the H_2O molecule in (a) C_{28} , (b) C_{30} , and (c) C_{32} cages. The inset figure depicts the evolution of the bending mode.

In passing, we note that, compared to studies on the more widely used O-H stretch modes, the study of the H-O-H bending mode provides more direct access to the vibrational response or change [78], and sheds light on an efficient mechanism for vibrational energy delocalization and dissipation [79]. Based on H-O-H bending mode as a potential marker to characterize a water molecule, the distinction between a water molecule confined in C_{32} and that in the C_{30} or C_{28} cages can be made by observing how the H-O-H bending mode responds to the applied field. A closer examination of insets in Fig. 4.4 reveals that the H-O-H bending mode in C_{32} shifts towards a higher wavenumber, which is consistent with the observed compression of vibrational spectrum observed in a recent study of

bulk liquid water under static electric fields using ab initio molecular dynamics simulations. In contrast, the bending mode in C_{28} and C_{30} shifts towards a lower wavenumber. This indicates that the confined water molecule in C_{28} and C_{30} differs from that confined in C_{32} , which is potentially an extreme nanoscopic confinement feature.

It is tempting to examine the sensitivity of the vibrational response of confined water to the external field through the calculation of the rate at which the H-O-H bending vibrational frequency shifts in response to the applied field. Calculation of the slope of a linear fit of wavenumber of the bending vibration peaks as a function of external field, for a water molecule confined inside C_{30} cage, shows the Stark tuning rate (STR) $|\Delta\vec{\mu}|$ of $0.20 \text{ cm}^{-1}/(\text{MV}/\text{cm})$, while $0.65 \text{ cm}^{-1}/(\text{MV}/\text{cm})$ for an isolated water molecule, and both of which are far smaller than the experimental value $3.3 \pm 0.3 \text{ cm}^{-1}/(\text{MV}/\text{cm})$ for an argon matrix-isolated water molecule [80]. As discussed in Chapter 1, the local effect, which causes the molecule to experience an actual field different from the applied field, is one possible cause of the discrepancy. Also, we did not calculate the STR for the bending modes of the water molecule in the other two cages C_{28} and C_{32} since the bending peak shifts in those cages were nonlinear.

At this juncture, one may attempt to use the theory of vibrational Stark effect (VSE) to determine the local field \vec{F}_{local} using the confined water molecule as a vibrational probe. However, when the vibrational probe is not a diatomic molecule, ambiguity exists regarding the direction of the difference dipole moment $\Delta\vec{\mu}$ between the ground and excited vibrational states [78, 81]. Instead, here we use the classical theory to estimate the local field, however, the defining parameters are obtained within the DFT calculations.

4.4.5 Local Field and Penetration Factor

A technically significant notion in persistent concerning a molecular cage is its presumed ability to shield the external electric field. This is known as a “Faraday cage”, which is typically a feature of a continuum closed metallic shell. To that end, the electrostatic shielding property of a C_{60} fullerene molecule was studied within the DFT formalism using the B3LYP functional. Calculations reveal that C_{60} acts as a molecular Faraday cage, allowing only a 25% field penetration, thereby preventing the external electric fields from reaching the cage’s interior [82]. On the other hand, a study based on the determination of the static and dynamic dipole polarizabilities of C_{60} using experimental data on the photoabsorption cross-section shows no shielding, with the electric field at the center of the cage being nearly twice as large as its exterior [83]. However, another DFT-based calculation shows that fullerenes with smaller HL gaps have better shielding capabilities than those with larger gaps [84].

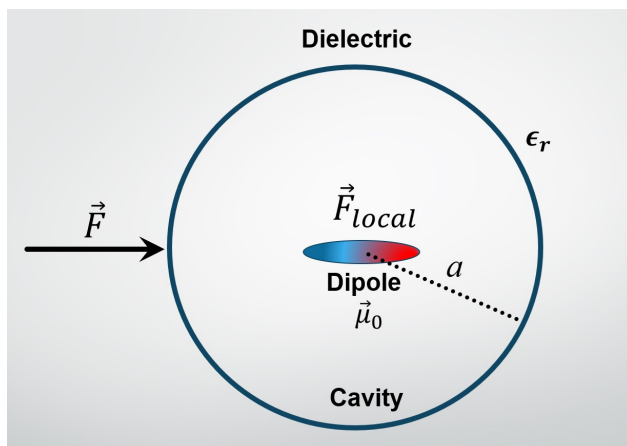


FIGURE 4.5: Onsager’s reaction field model consisting of a spherical cavity of radius ‘ a ’ in a dielectric continuum of relative permittivity ϵ_r subjected to external field \vec{F} , corresponding to which local field at dipole’s position is \vec{F}_{local} .

Here, we study the shielding behavior of small-size fullerenes using a heuristic approach based on Onsager’s reaction field model [85], which consists of a spherical cavity in a dielectric continuum with permittivity ϵ_r confining a permanent dipole $\vec{\mu}_0$ within. A schematic of this model is shown in Fig. 4.5,

which takes into account the back-action field (also known as reaction field) on a dipole inside the cavity subjected to an external field \vec{F} . This results in a net local field at the dipole's position given by [86, 87]

$$\vec{F}_{local} = \vec{F}_{internal} + \vec{F}_{reaction}, \quad (4.1)$$

where $\vec{F}_{internal}$ is the cavity field that can be expressed in terms of the external field as [88],

$$\vec{F}_{internal} = \frac{3\epsilon_r}{2\epsilon_r + 1} \vec{F}. \quad (4.2)$$

The reaction field is proportional to the total dipole moment $\vec{\mu}$, i.e., $\vec{F}_{reaction} = f'\vec{\mu} = f'(\vec{\mu}_0 + \vec{\mu}_{induced}) = f'(\vec{\mu}_0 + \alpha\vec{F}_{local})$, where $f' = 2(\epsilon_r - 1)/(a^3(2\epsilon_r + 1))$ is the reaction field factor, while α is dipole's polarizability. Therefore, the reaction field can be expressed in terms of the external field as [87]

$$\vec{F}_{reaction} = f' \left[\left(1 + \frac{f'\alpha}{1 - f'\alpha}\right) \vec{\mu}_0 + \frac{\alpha}{(1 - f'\alpha)} \frac{3\epsilon_r}{(2\epsilon_r + 1)} \vec{F} \right]. \quad (4.3)$$

Thus, the local electric field at the dipole's position can be estimated from Eq. (4.1) as the sum of internal field and the reaction field. The question of the feasibility of this model depends on the degree to which the physical system resembles this purely theoretical construct. Nevertheless, we believe that the observations based on this model might potentially describe the electric field response of a water molecule confined in the fullerene cages.

Among others [89, 90], another way to gauge the degree to which the external electric field enters the cavity is through the determination of penetration factor for a spherical dielectric shell [88],

$$p = \frac{9\epsilon_r}{(2\epsilon_r + 1)(\epsilon_r + 2) - 2(\epsilon_r - 1)^2(a_1/a_2)^3}, \quad (4.4)$$

obtained as an electric counterpart of magnetic penetration factor employing the

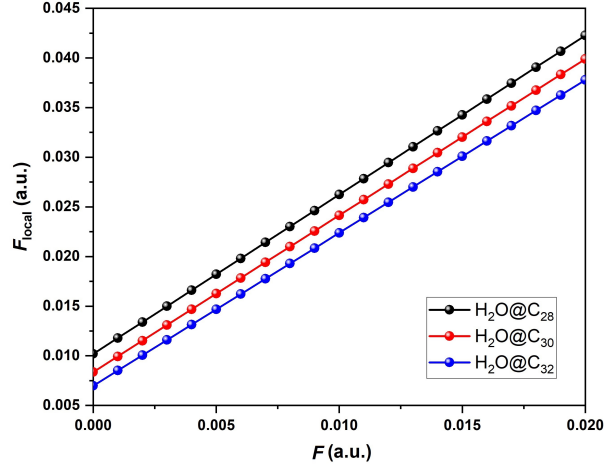


FIGURE 4.6: Local field $|\vec{F}_{local}|$ as a function of external field $|\vec{F}|$.

electromagnetic duality of permeability and permittivity of the medium, i.e., $\mu_r \leftrightarrow \epsilon_r$. In the above equation, $a_1 = a - \delta$ and $a_2 = a + \delta$ are the inner and outer radius of the spherical shell of radius ‘ a ’ and thickness δ . We consider ‘ a ’ to be cavity radius, while $\delta = 0.9$ Å [89]. An essential element in both the expressions for local field (\vec{F}_{local}) and penetration factor (p) is the dielectric constant ϵ_r of the continuum shell. We adopt Penn’s model for dielectric constant, i.e., $\epsilon_r \approx 1 + E_p/E_g$ [91], where E_p is the surface plasmon resonance energy of the dielectric shell and E_g is its energy band gap, which in the case of a molecular system is the HL gap. We consider $E_p \approx 20$ eV uniform for all fullerenes [92, 93].

TABLE 4.4: Calculated zero-field parameters for a water molecule and small-sized fullerenes relevant for the estimation of local field and penetration factor.

Parameters	H ₂ O	C ₂₈	C ₃₀	C ₃₂
$ \vec{\mu}_0 $ (Debye)	2.18			
α (a.u.)	6.95			
E_p (eV)		20.0	20.0	20.0
E_g (eV)		3.22	3.09	4.38
		3.27 ^a	3.18 ^a	4.48 ^a
ϵ_r		39.57	42.89	21.85

^aHL gap with water molecule confined within.

Considering the parameters tabulated in Table 4.4, the local field $|\vec{F}_{local}|$ is obtained by approximating the HL gap of the empty cages in a field comparable

to that of the cages containing water molecule at the corresponding field values. This is reasonable because there is no discernible effect of the confined water on the frontier molecular orbitals of the fullerene cages. The variation of the local field $|\vec{F}_{local}|$ as a function of the external field $|\vec{F}|$ is shown in Fig. 4.6. It is evident that the ratio $|\vec{F}_{local}|/|\vec{F}| \gg 1$ for very small fields, but for larger fields, it gradually approaches 1 and eventually falls below 1 at extremely high fields.

The penetration factor ‘ p ’ for the cages varies depending on how the HL gap changes after field application. Calculation shows that the penetration factor for C_{28} and C_{32} cages is $\sim 12\%$ and $\sim 21\%$, respectively, and decreases gradually as the external field increases. In contrast, for C_{30} , it is $\sim 11\%$ and, it increases as field increases, while for C_{60} it is $\sim 23\%$ which is close to that reported in [82]. Nevertheless, the HL gap generally tends to decrease at high field, leading to a decrease in the penetration factor at high field values. This is consistent with the calculations based on the reaction field theory, which suggests that the ratio $|\vec{F}_{local}|/|\vec{F}|$ decreases with an increase in field. Furthermore, because their HL gaps are less than those of large-sized fullerenes like C_{60} or C_{70} , small-sized fullerenes provide better shielding capabilities. This is in conformity with the observation in [84]. It must be mentioned, however, that our observations are limited to the specific situations where the calculated results in the presence of an external electric field reasonably characterize realistic situations.

4.4.6 $CO@(5^{12}, 5^{12}6^2, 5^{12}6^4)$ cages

We now consider the three basic H-bonded building block cages of the cubic sI and sII lattice structures of clathrate hydrates, viz., 5^{12} , $5^{12}6^2$ and $5^{12}6^4$ that contain 20, 24 and 28 water molecules, respectively. The structures are optimized at the $\omega B97X-D/6-311++G(d,p)$ level of theory and are shown in Fig. 4.7, while the optimized geometrical parameters are presented in Table 4.5. Optimization at the B97D/6-311++G(d,p) level produced comparable results with a deviation within

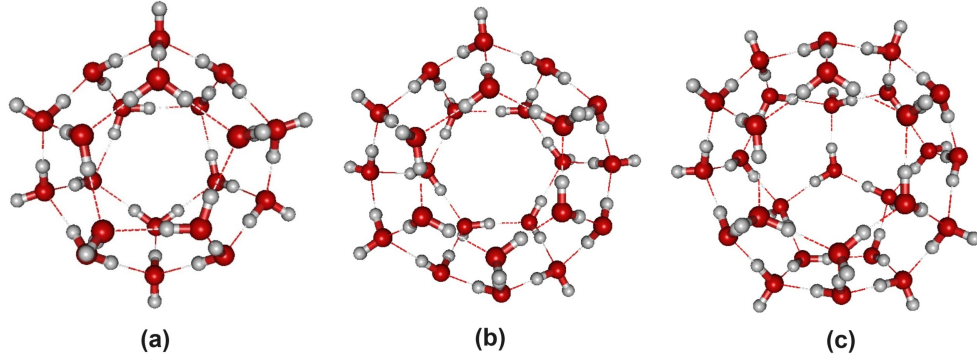


FIGURE 4.7: Energy minimum structure of (a) 5^{12} , (b) $5^{12}6^2$, and (c) $5^{12}6^4$ H-bonded building block cages of the cubic sI and sII lattice structures of the clathrate hydrates.

± 0.01 Å. However, the observed gradual shortening of average O··O distance and H-bond length with an increase in cage size is a manifestation of the cooperativity effects in the H-bonding system, which results from the mutual polarization of the molecules in the system [95]. Carbon monoxide is then inserted inside the optimized (5^{12} , $5^{12}6^2$, $5^{12}6^4$) cages and the resultant geometry is optimized for the study of electric field influence on the building block cages of the CO clathrate hydrates. The optimized structures of the CO@(5^{12} , $5^{12}6^2$, $5^{12}6^4$) cages are shown

TABLE 4.5: Geometrical parameters (Å) calculated at the ω B97X-D/6-311++G(d,p) level.

Parameters	5^{12}	$5^{12}6^2$	$5^{12}6^4$
Cavity radius ^a	3.8821	4.2673	4.6162
Ave. O··O distance	2.7634	2.7604	2.7568
Ave. H-bond length	1.7842	1.7811	1.7792

^aStandard values are respectively 3.95, 4.33, 4.73 [94].

in Fig. 4.8, however, cages' radii are found to slightly decrease to (3.8528, 4.2508, 4.6027 Å), respectively, after CO encapsulation as compared to the empty cages. Similar cage shrinkage has also been seen in other computational investigations when a relatively small molecule occupies the cage [96]. While the CO molecule occupies center position in the CO@ 5^{12} cage, it chooses an off-centered location inside the CO@($5^{12}6^2$, $5^{12}6^4$) cages. In particular, CO is displaced toward one of the cage's pentagonal faces in CO@ $5^{12}6^2$, with a nearest C··O distance of 3.36 Å.

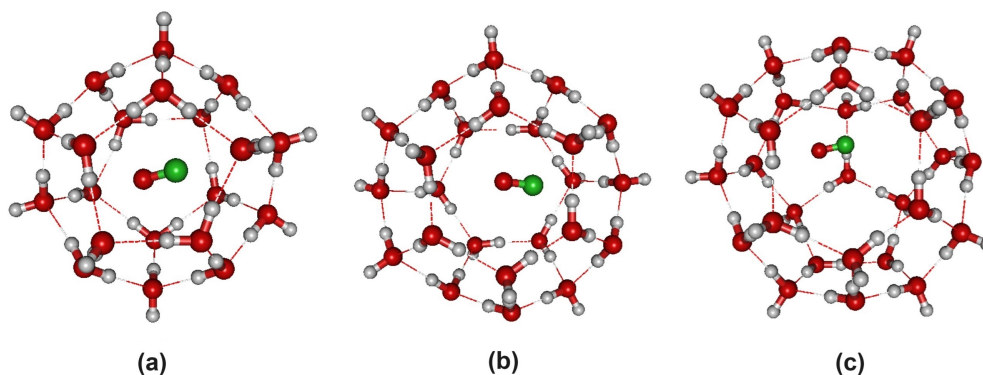


FIGURE 4.8: Energy minimum structure of (a) $\text{CO}@5^{12}$, (b) $\text{CO}@5^{12}6^2$, and (c) $\text{CO}@5^{12}6^4$ H-bonded building block cages of the CO clathrate hydrates.

In contrast, CO rests closer to one of the cage's hexagonal faces in $\text{CO}@5^{12}6^4$, with a nearest $\text{C}\cdots\text{O}$ distance of 3.45 Å. Clearly, the cage structure is not considerably distorted by the encapsulation of a CO molecule.

4.4.7 Energetics and Reactivity Indices

The energetic stability of the building block cages of the CO clathrate hydrates is studied by computing the interaction energy as the energy of a cluster minus the sum of the energies of the constituent molecules in the cluster in isolation. The interaction energies, however, uncorrected for basis set superposition error (BSSE) are presented in Table 4.6. For order of magnitude comparison, results from a calculation based on Møller–Plesset second-order (MP2) perturbative theory are also placed alongside. Stabilization of cages with a growing number of water molecules is evident, while the CO encapsulated cages exhibit a reverse tendency.

In order to investigate the extent of deformation of the water cage structures upon CO encapsulation, we additionally compute the deformation energy. The difference in energy between an empty cage and one that has CO encapsulated is used as a measure of deformation energy, i.e., $E_{\text{Def}} = E_{(\text{empty cage})} - E_{(\text{cage with CO})}$. The computed deformation energy in each of the three cages under consideration is negligible. This reaffirms that the cage structures are barely

TABLE 4.6: Interaction energies (kcal/mol) (BSSE uncorrected) in empty and guest-host complexes. The values in parentheses are the deformation energies.

Structures	ω B97X-D	B97-D	MP2
(5 ¹²)	-233.99	-218.49	-211.52 ^a
(5 ¹² 6 ²)	-280.45	-261.21	
(5 ¹² 6 ⁴)	-329.60	-307.49	
CO@(5 ¹²)	-5.67 (-0.14)	-4.07 (-0.12)	-7.93 ^b
CO@(5 ¹² 6 ²)	-5.14 (-0.13)	-4.50 (-0.08)	
CO@(5 ¹² 6 ⁴)	-3.99 (-0.07)	-4.27 (-0.05)	

^aCalculated with aug-cc-pVDZ basis set [97].

^bCalculated with 6-311++G(d,p) basis set [98].

altered by the encapsulation of a single CO molecule. However, our study is limited to an encapsulation of a single CO molecule, but the cages would deform considerably with the addition of more CO molecules.

As discussed in Chapter 1, reactivity indices, such as chemical hardness (η), electronegativity (χ), and electrophilicity (ω), can be used to assess a molecular system's chemical stability. Table 4.7 displays the reactivity indices computed

TABLE 4.7: Reactivity indices (eV), chemical hardness (η), electronegativity (χ) and electrophilicity (ω), for empty and CO encapsulated cages evaluated at the ω B97X-D/6-311++G(d,p) level of theory. The values in the parentheses are reported to be calculated at the MP2/6-31+G(d) level [99].

Structures	η	χ	ω
(5 ¹²)	11.021 (15.609)	4.802 (5.105)	1.046 (0.831)
(5 ¹² 6 ²)	10.172 (15.132)	4.724 (5.272)	1.096 (0.918)
(5 ¹² 6 ⁴)	10.615	4.564	0.981
CO@(5 ¹²)	11.056	4.797	1.040
CO@(5 ¹² 6 ²)	10.192	4.730	1.097
CO@(5 ¹² 6 ⁴)	10.632	4.590	0.990

at the ω B97X-D/6-311++G(d,p) level of theory, which are also compared to those computed at the MP2 level of the perturbation theory. It is evident that the reactivity indices change to the tune of 0.065 eV (≈ 1.5 kcal/mol) or less in relation to an empty cage. The chemical hardness (η) hardly exhibits an increasing trend, while the electronegativity (χ) and electrophilicity (ω) show insignificant change.

Therefore, CO encapsulation does not affect the physico-chemical properties of the building block cages.

4.4.8 NCI Analysis

A key mechanism in the stabilization of inclusion compounds like clathrate hydrates is the non-covalent interactions between the host and the guest molecule. As discussed in Chapter 1, Bader’s theory of Atoms in Molecules (AIM) allows one to examine the different interactions among the atoms in a molecule by calculating the electron density and associated Laplacian at the bond critical points [100]. However, because of the molecular system’s complexity, it can occasionally be exceedingly challenging to compute the essential parameters that define the nature of a bond within the AIM theory. Nevertheless, a reduced density gradient (RDG)-based direct visualization of the non-covalent interactions in a molecular system has gained popularity as it has specific standards for the characterization of the weak interactions like the van der Waals (vdW) interaction, both the repulsive and attractive components, as well as the steric interactions between the molecules’ constituent parts [101, 102].

The RDG scatter plot and the RDG isosurface map for CO@(5^{12} , $5^{12}6^2$, $5^{12}6^4$) cages are shown in Fig. 4.9. A glance at the map reveals that both H-bonding (blue color) and van der Waals (green color) interactions stabilize the cage structure. Less noticeable inverted peak structures for $\text{sign}(\lambda_2)\rho(\vec{r}) \leq -0.30$ a.u. denotes H-bonding interaction, which becomes more prominent with an increase in cage size, indicating strong H-bonding in the large-sized cage. Furthermore, the presence of two prominent troughs (inverted peaks) on both sides of $\text{sign}(\lambda_2)\rho(\vec{r}) \simeq 0$ indicate that the cages’ structural stability is a result of both the attractive and repulsive components of the van der Waals interaction. These troughs, however, become less prominent as the cage size grows, indicating that the van der Waals interaction between CO and the cage tends to weaken as expected.

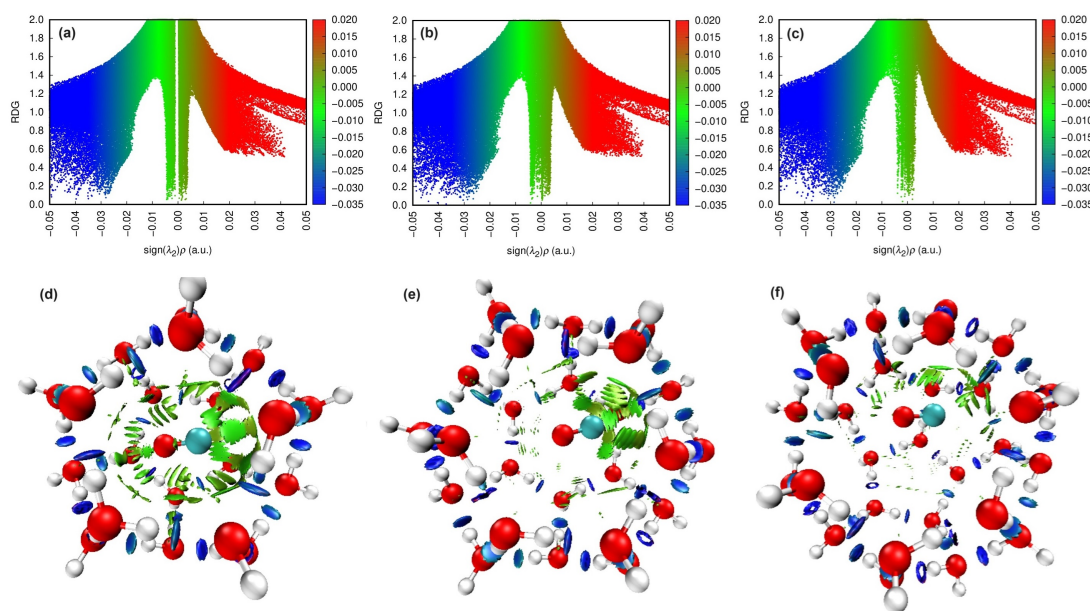


FIGURE 4.9: RDG scatter plot (a)-(c) for $\text{CO}@(\mathbf{5}^{12})$, $\text{CO}@(\mathbf{5}^{12}\mathbf{6}^2)$, $\text{CO}@(\mathbf{5}^{12}\mathbf{6}^4)$, respectively, and the corresponding RDG isosurface (d)-(f) illustrating NCI regions drawn at the RDG value of 0.5.

Importantly, the presence of van der Waals interaction necessitates the use of dispersion-corrected functional, thereby validating our choice of functional for the H-bonded cages having a CO molecule confined within. We now present results on the electric field response of CO confined inside the H-bonded cages.

4.4.9 Electric Field Response of Confined CO

The electric field response of a molecule manifests itself as the molecule's geometric distortion and redistribution of electron density, which causes a change in the bond lengths and the frequency of the vibrational modes. This is observed for CO confined in $(\mathbf{5}^{12}, \mathbf{5}^{12}\mathbf{6}^2, \mathbf{5}^{12}\mathbf{6}^4)$ cages, as shown in Fig. 4.10. The observed abrupt change in CO bond length and CO stretching wavenumber over otherwise its steady variation with the field is due to a substantial change in the geometry and electron density distribution at the corresponding field values.

In the IR spectrum, the CO stretch vibrational peak occurs at (2242, 2233, 2237) cm^{-1} for the $(\mathbf{5}^{12}, \mathbf{5}^{12}\mathbf{6}^2, \mathbf{5}^{12}\mathbf{6}^4)$ cages, respectively. When an electric

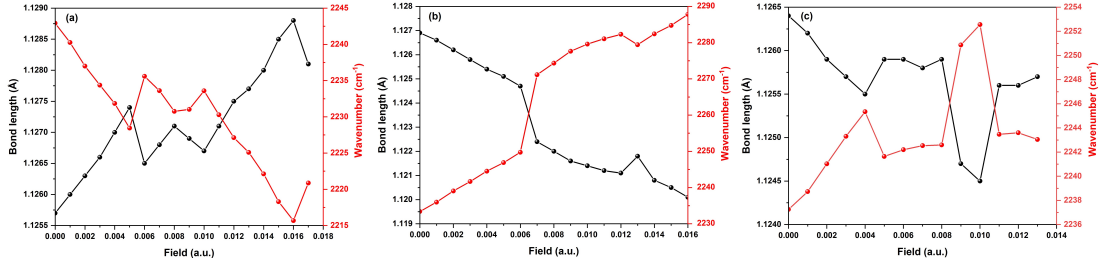


FIGURE 4.10: CO bond length (Å) and CO stretching frequency peak position (cm^{-1}) as a function of applied field in (a) $\text{CO}@5^{12}$, (b) $\text{CO}@5^{12}6^2$, and (c) $\text{CO}@5^{12}6^4$ cages.

field is applied, the peak shifts toward lower wavenumbers (red shift) in $\text{CO}@5^{12}$, while they move toward higher wavenumbers (blue shift) in $\text{CO}@5^{12}6^2$, $5^{12}6^4$ cages. The latter feature, that is directly related to CO bond elongation, is especially relevant since it suggests that CO bond elongation may arise from a substantial disruption of the H-bonded cage to the point where CO confinement is loosened, leading to possible CO escape or release. Nevertheless, what has been observed experimentally is that the O–H stretching peak for clathrate hydrate exhibits a significant blue-shift at high field $\sim 1\text{V}/\text{\AA}$ [61], indicating sufficient distortion of the hydrate lattice structure, enough to release the trapped tetrahydrofuran $(\text{CH}_2)_4\text{O}$ gas molecule. However, this is not evident in the field-induced

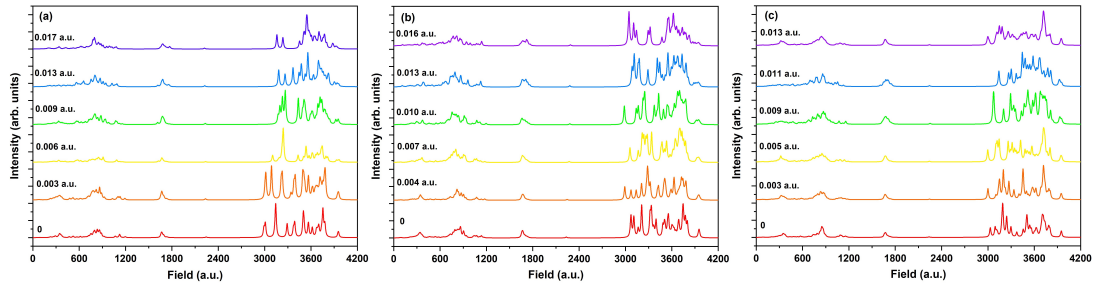


FIGURE 4.11: Field evolution of IR spectra of (a) $\text{CO}@5^{12}$, (b) $\text{CO}@5^{12}6^2$, and (c) $\text{CO}@5^{12}6^4$ cages, showing three characteristic vibrational modes; liberation ($\lesssim 1000 \text{ cm}^{-1}$), H-O-H bending ($\sim 1740 \text{ cm}^{-1}$) and O-H stretching ($> 3000 \text{ cm}^{-1}$).

evolution of the IR spectra shown in Fig. 4.11. This is because, in the condensed phase, due to enhanced intermolecular interactions and mutual polarization, the local electric field considerably weakens the O–H bonds, leading to field-induced disruption of H-bonds at a much lower field than in the isolated or small water

clusters. To that effect, computational studies have shown that the breakup of a small H-bonded system takes place with an emergence of the O-H stretching peaks in the lower wavenumber region, $\sim 2600\text{-}3000\text{ cm}^{-1}$ or less [103, 104]. However, this occurs at sufficiently high fields well over 0.02 a.u. ($\approx 1.02\text{ V/\AA}$), but we did not take such a high field into consideration in the present work.

4.4.10 Field-Induced Structural Evolution

We now discuss the structural evolution induced by the applied field on the $\text{CO}@(\text{5}^{12}, \text{5}^{12}\text{6}^2, \text{5}^{12}\text{6}^4)$ cages. In contrast to the case of H_2O confined in covalently bonded fullerene cages, where the dipole moment increases linearly for fields as large as 0.020 a.u., the dipole moment in the case of CO confined in H-bonded cages increases linearly only in a small field range up until 0.005 a.u., after which

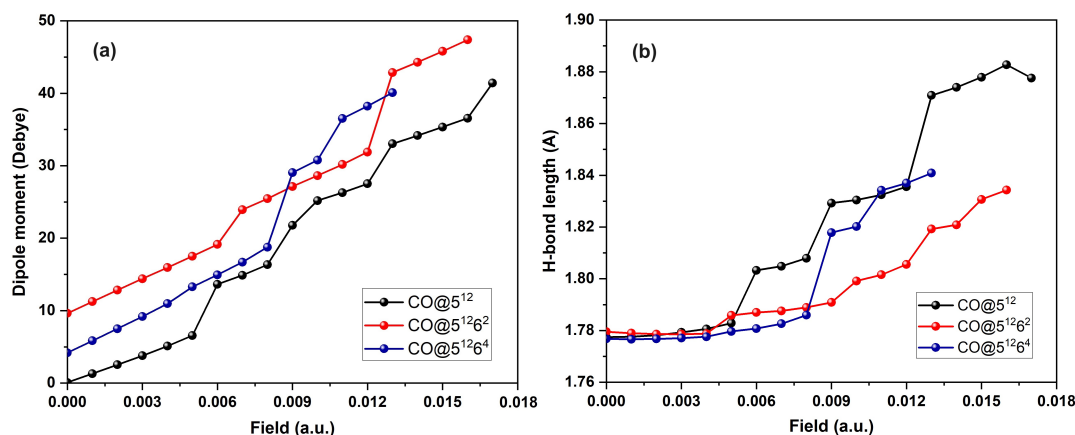


FIGURE 4.12: (a) Dipole moment and (b) average H-bond length in $\text{CO}@(\text{5}^{12}, \text{5}^{12}\text{6}^2, \text{5}^{12}\text{6}^4)$ cages.

it becomes erratic. This variation results from the alignment of individual water dipoles along the direction of the field, which becomes increasingly significant as the field increases. Eventually, the dipole-field interactions ($-\vec{\mu}_i \cdot \vec{F}$) overwhelm the intermolecular interactions at high field, resulting in the rupture of the H-bonds.

The field-induced rearrangement of H-bonds and their eventual breakdown cause the cage structure to differ significantly from the field-free closed form.

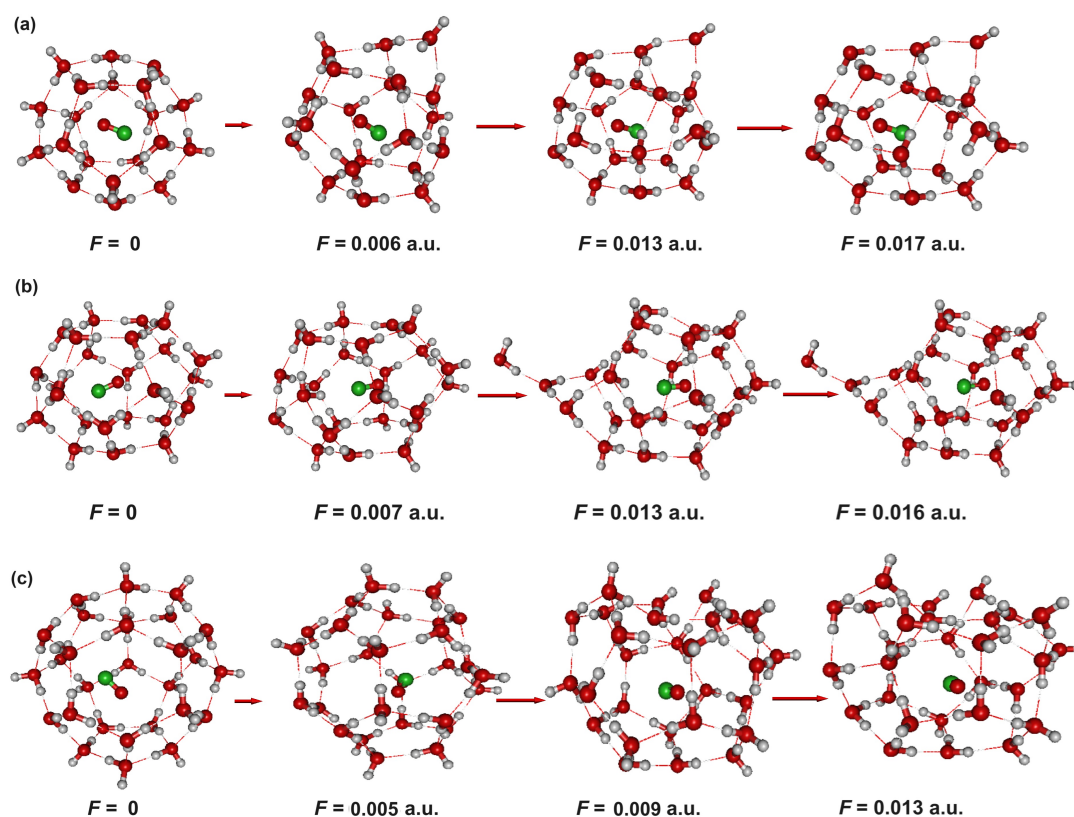


FIGURE 4.13: Field-induced structural evolution of (a) $\text{CO}@5^{12}$, (b) $\text{CO}@5^{12}6^2$, and (c) $\text{CO}@5^{12}6^4$ structures. The applied field \vec{F} is indicated by an arrow, whose length proportionally represents its magnitude..

This is shown in Fig. 4.13 for the characteristic field values marked by an abrupt increase in dipole moment in the corresponding field values as illustrated in Fig. 4.12. Interestingly, a closer examination of the iteration steps in the optimization process revealed migration of the CO molecule towards the H-bond disrupted region of the cage. This observation could potentially indicate a field-induced release or escape of CO, which was found to be more noticeable in the case of $\text{CO}@ (5^{12}6^2, 5^{12}6^4)$ cages. However, to gain a deeper insight into the understanding of the dynamics of CO capture or release in clathrate hydrates, a MD simulations study is indispensable, and this is beyond the scope of the present work. From the technological perspective, a mechanism of this kind increases the possibility of a selective reaction by releasing a molecule under a controlled setup at a specific site of interest. Undoubtedly, this has far-reaching implications for device application and integration. However, we avoid delving too far into this without doing extensive

studies, as else it would merely be a speculation and assumption.

4.5 Summary and Concluding Remarks

We now summarize the key findings of the work presented in this chapter. A molecule nanoconfined in a molecular cage exhibits behavior distinct from that of the condensed phase, which is crucially dependent on the cage size. The geometrical properties of a water molecule are distorted by its confinement inside small-size fullerenes, like C_{28} , C_{30} , and C_{32} . This distortion is particularly severe in the case of C_{28} and C_{30} . Such extreme confinement has a remarkable effect on O-H stretching vibrations, causing the asymmetric stretching at a lower wavenumber than the symmetric stretching. On the other hand, in the case of $H_2@C_{32}$, symmetric stretching occurs at a lower wavenumber than asymmetric stretching, which is a characteristic feature in a typical confinement and condensed phases. This implies that H_2O molecule entirely loses its feature of a typical water when it is confined in small fullerenes of size equal to C_{30} or smaller. Additionally, even though the dipole screening makes the $H_2O@(C_{28}, C_{30}, C_{32})$ cages almost nonpolar in nature, the applied field induces a sizable dipole moment that increases linearly to the tune of 0.014 Debye per $mV/\text{\AA}$. This remarkable characteristic could be useful in the development of dipole-based molecular junction devices [75]. However, the $H_2O@(C_{28}, C_{30}, C_{32})$ cages are not suitable for the optoelectronic applications due to the HL gap being more than 3 eV, which either stays essentially unchanged or steadily increases for field in the range (0-0.02 a.u.). Extremely high fields, much higher than 0.02 a.u., do reduce the HL gap, but they cause the cage structure sufficiently distorted to the point of disintegration. Concerning shielding efficiency, there is a strong correlation with the HL gap. The smaller the gap, the better the shielding efficiency, and thus the small-size fullerenes that have small HL gaps offer better shielding than the larger fullerenes. Furthermore, since the electric field modulates the gap to decrease generally, shielding efficiency varies with field

strength, thereby making larger fields better shielded than small fields. This property may be particularly useful in improving the molecular device performance characteristics in the electrostatic environment.

The confinement of a CO molecule inside the H-bonded building blocks of the sI and sII clathrate hydrates, viz., (5^{12} , $5^{12}6^2$, $5^{12}6^4$) cages, results in negligible structural modifications. Nevertheless, the confinement of CO provides both attractive and repulsive van der Waals interactions, which together with the H-bonding interaction between the water molecules, provide stability to the CO-bound cages. Undoubtedly, the van der Waals interaction becomes less significant in the larger cages, which the NCI analysis concludes affirmatively. Nonetheless, in the presence of an electric field, the CO confined in the ($5^{12}6^2$, $5^{12}6^4$) cages, in particular, exhibits a blue shift in its stretching vibration. This indicates an elongation of the CO bond, which could result from a significant disruption of the H-bonded cage to the extent that CO confinement is loosened, thereby possibly allowing it to escape or be released. Situations indicative of the potential occurrence of such an event are usually marked by an abrupt increase in the dipole moment, and the emergence of O-H stretching of the cage structures in the lower wavenumber region below 3000 cm^{-1} [103, 104]. However, the latter characteristic would be observed only under a situation with exceptionally high field. From the perspective of molecular device technology, a mechanism of this kind enhances the possibility of a selective reaction by releasing a molecule through field application at a specific site of interest under precisely controlled conditions. This certainly has an enormous implication for the possibility of massively parallel integration of the molecular devices with an atomic precession. The computational results that are so impressive must have extraordinary validity, which needs to be tested in experimental setups under comparable situations. We anticipate that in the near future, an experimental enthusiast with ever-improving sophisticated technological setups will validate the current theoretical conclusions.

References

- [1] G. Buntkowsky and M. Vogel, *Molecules*, **25**, 3311 (2020).
- [2] Y. Yu and J. Rebek Jr., *Q. Rev. Biophys.* **53**, e6 (2020).
- [3] H. Takezawa and M. Fujita, *Bull. Chem. Soc. Jpn.* **94**, 2351 (2021).
- [4] A. Braschinsky and J. W. Steed, *Coord. Chem. Rev.* **473**, 214840 (2022).
- [5] B. P. Gorshunov, et al., *J. Phys. Chem. Lett.* **4**, 2015 (2013).
- [6] A. I. Kolesnikov, et al., *Phys. Rev. Lett.* **116**, 167802 (2016).
- [7] Y. Hashikawa and Y. Murata, *Bull. Chem. Soc. Jpn.* **96**, 943 (2023).
- [8] S. Adhikari and R. Chowdhury, *Phys. Lett. A* **375**, 2166 (2011).
- [9] J. B. Howard, A. L. Lafleur, Y. Makarovsky, S. Mitra, C. J. Pope, and T. K. Yadav, *Carbon*, **30**, 1183 (1992).
- [10] J. Cami, J. B.-Salas, E. Peeters, and S. E. Malek, *Science*, **329**, 1180 (2010).
- [11] C. N. Ramachandran and N. Sathyamurthy, *Chem. Phys. Lett.* **410**, 248 (2005).
- [12] S. -C. Chuang, F. R. Clemente, S. I. Khan, K. N. Houk, and Y. Rubin, *Org. Lett.* **8**, 4525 (2006).
- [13] K. Komatsu, M. Murata, and Y. Murata, *Science*, **307**, 238 (2005).
- [14] K. Kurotobi and Y. Murata, *Science*, **333**, 613 (2011).
- [15] C. Thilgen, *Angew. Chem. Int. Ed.* **51**, 587 (2012).
- [16] S. Kaneko, Y. Hashikawa, S. Fujii, Y. Murata, and M. Kiguchi, *Chem. Phys. Chem.* **18**, 1229 (2017).

- [17] B. Liu, J. Chen, Y. Ouyang, M. Zhang, Y. -Z. Tan, and F. Song, *Chinese Phys. B* **32**, 063601 (2023).
- [18] C. Zhu and X. Wang, *Sci. Rep.* **5**, 17932 (2016).
- [19] S. Fujii, H. Cho, Y. Hashikawa, T. Nishino, Y. Murata, and M. Kiguchi, *Phys. Chem. Chem. Phys.* **21**, 12606 (2019).
- [20] P. R. Varadwaj and A. Varadway, *Chem. Eur. J.* **18**, 15345 (2012).
- [21] O. Shameema, C. N. Ramachandran, and N. Sathyamurthy, *J. Phys. Chem. A* **110**, 2 (2006).
- [22] K. Yagi and D. Watanabe, *Int. J. Quant. Chem.* **109**, 2080 (2009).
- [23] B. Ensing, F. Costanzo, and P. L. Silvestrelli, *J. Phys. Chem. A* **116**, 12184 (2012).
- [24] D. Bucher, *Chem. Phys. Lett.* **534**, 38 (2012).
- [25] S. P. Jarvis, et al., *Commun. Chem.* **4**, 135 (2021).
- [26] B. Meier, S. Mamone, M. Concistre, J. A. -Valdesueiro, A. Krachmalnicoff, R. J. Whitby, and M. H. Levitt, *Nat. Commun.* **6**, 8112 (2015).
- [27] A. Shugai, U. Nagel, Y. Murata, Y. Li, S. Mamone, A. Krachmalnicoff, S. Alom, R. J. Witby, M. H. Levitt, and T. Room, *J. Chem. Phys.* **154**, 124311 (2021).
- [28] H. W. Kroto, *Nature*, **329**, 529 (1987).
- [29] J. M. L. Martin, *Chem. Phys. Lett.* **255**, 1 (1996).
- [30] P. R. C. Kent, M. D. Towler, R. J. Needs, and G. Rajagopal, *Phys. Rev. B* **62**, 15394 (2000).
- [31] P. W. Dunk, et al., *J. Am. Chem. Soc.* **134**, 9380 (2012).

- [32] A. G. -Torres, R. Esper, P. W. Dunk, R. M. -Martínez, A. R. -Forteza, L. Echegoyen, and J. M. Poblet, *Helv. Chim. Acta*, **102**, e1900046 (2019).
- [33] K. Xu, T. Yang, Y. Feng, X. Ruan, Z. Liu, G. Liang, and X. Wang, *Nanomater.* **9**, 1068 (2019).
- [34] C. E. Spano, F. Mo, Y. Ardesi, M. R. Roch, G. Piccinini, and M. Graziano, *In Proceedings of the 8th World Congress on New Technologies (NewTech'22), Prague, Czech Republic*, Paper No. ICNFA 138 (August 03-05, 2022).
- [35] J. Klos, E. Tiesinga, and S. Kotochigova, *Sci. Rep.* **14**, 9267 (2024).
- [36] E. D. Sloan Jr., C. A. Koh, *Clathrate Hydrates of Natural Gases*, CRC Press, Boca Raton, 3ed. (2007).
- [37] C. I. Ratcliffe, *Energy Fuels*, **36**, 10412 (2022).
- [38] K. C. Hester and P. G. Brewer, *Annu. Rev. Mar. Sci.* **1**, 303 (2009).
- [39] P. E. Chibura, W. Zhang, A. Luo, and J. Wang, *J. Nat. Gas Eng.* **100**, 104441 (2022).
- [40] W. Liu, J. Hu, X. Li, Z. Sun, F. Sun, and H. Chu, *J. Nat. Gas Eng.* **60**, 256 (2018).
- [41] Y. Guimin, J. Hao, and K. Qingwen, *Front. Earth Sci.* **9**, 816873 (2022).
- [42] J. Zhao, C. Lang, J. Chu, L. Yang, and L. Zhang, *J. Phys. Chem. C* **127**, 13439 (2023).
- [43] Y. -S. Yu, X. Zhang, J. -W. Liu, Y. Lee, and X. -S. Li, *Energy Environ. Sci.* **14**, 5611 (2021).
- [44] M. Kastner, M. Myers, C. A. Koh, G. Moridis, J. E. Johnson, and J. Thurmond, *Energy Fuels*, **36**, 2923 (2022).
- [45] E. D. Sloan Jr, *Nature*, **426**, 353 (2003).

- [46] W. L. Mao, C. A. Koh, and E. D. Sloan, *Phys. Today*, **60**, 42 (2007).
- [47] Y. Matsumoto, R.G. Grim, N.M. Khan, T. Sugahara, K. Ohgaki, E.D. Sloan, C.A. Koh, A.K. Sum, *J. Phys. Chem. C* **118**, 3783 (2014).
- [48] E. Dartois, *Icarus*, **212**, 950 (2011).
- [49] D. W. Davidson, M. A. Desando, S. R. Gough, Y. P. Handa, C. I Ratcliffe, J. A. Ripmeester, and J. S. Tse, *Nature*, **328**, 418 (1987).
- [50] J. Zhu, et al., *Nat. Commun.* **5**, 4128 (2014).
- [51] P. Kumar, B. J. Mishra, and N. Sathiyamurthy, *Comput. Theor. Chem.* **1029**, 26 (2014).
- [52] C. Petuya, L. M. -Gondre, P. Aurel, F. Damay, A. Desmedt, *J. Chem. Phys.* **150**, 184705 (2019).
- [53] E. Wang and Y. Gao, *J. Phys. Chem. A* **127**, 1190 (2023).
- [54] A. Kumar and P. Kumar, *Comput. Theor. Chem.* **1206**, 113493 (2021)
- [55] D. Rai, A. D. Kulkarni, S. P. Gejji, and R. K. Pathak, *Theor. Chem. Acc.* **123**, 501 (2009).
- [56] Y. Yasutake, Z. Shi, T. Okazaki, H. Shinohara, and Y. Majima, *Nano. Lett.* **5**, 1057 (2005).
- [57] D. P. Luis, E. C. H. -Hernandez, and H. S. -Martin, *J. Chem. Phys.* **143**, 204503 (2015).
- [58] M. R. Ghaani and N. J. English, *J. Phys. Chem. C* **122**, 7504 (2018).
- [59] Y. Krishnan, M. R. Ghaani, and N. J. English, *J. Phys. Chem. C* **123**, 27554 (2019).
- [60] Y. Krishnan, P. G. Rosingana, M. R. Ghaani, and N. J. English, *RCS Adv.* **12**, 4370 (2022).

- [61] Z. Li, M. Lyu, H. Jonsson, and C. R. -Petruck, *J. Phys. Chem. Lett.* **12**, 10410 (2021).
- [62] M. Lyu, Z. Li, M. van den Bossche, H. Jonsson, and C. R. -Petruck, *Chem. Phys.* **568**, 111839 (2023).
- [63] J. Pitters, et al., *ACS Nano*, **18**, 6766 (2024).
- [64] Yoshida’s Fullerene Library, <https://nanotube.msu.edu/fullerene/fullerene-isomers.html>
- [65] Optimized geometries at the B3LYP/cc-pVDZ + STO-3G level were obtained from Prof. K. Yagi (personal communication), while reoptimization at the B3LYP/6-311++G(d,p) level shows two imaginary vibrational frequencies.
- [66] W. S. Benedict, N. Gailar, and E. K. Plyler, *J. Chem. Phys.* **24**, 1139–1165 (1956).
- [67] D. Sh. Sabirov and R. G. Bulgakov, *JETP Lett.* **92**, 662 (2010).
- [68] S. A. Clough, Y. Beers, G. P. Klein, and L. S. Rothman, *J. Chem. Phys.* **59**, 2254 (1973).
- [69] C. G. Elles, C. A. Rivera, Y. Zhang, P. A. Pieniazek, and S. E. Bradforth, *J. Chem. Phys.* **130**, 084501 (2009).
- [70] X. Blasé, C. Attaccalite, and V. Olevano, *Phys. Rev. B* **83**, 115103 (2011).
- [71] S. H. Yang, C. L. Pettiette, J. Conceicao, O. Cheshnovsky, and R. E. Smalley, *Chem. Phys. Lett.* **139**, 233 (1987).
- [72] P. L. Hensen, P. J. Fallon, and W. Krätschmer, *Chem. Phys. Lett.* **181**, 367 (1991).
- [73] R. W. Lof, M. A. van Veenendaal, B. Koopmans, H. T. Jonkman, and G. A. Sawatzky, *Phys. Rev. Lett.* **68**, 3924 (1992).

- [74] R. K. Kremer, *Appl. Phys. A* **56**, 211 (1993).
- [75] S. Tanimoto, M. Tsutsui, K. Yokota, and M. Taniguchi, *Nanoscale Horiz.* **1**, 399 (2016).
- [76] L. R. C. Wang, H. J. Kreuzer and O. Nishikawa, *Org. Electron.* **7**, 99 (2006).
- [77] M. Karahka and H.J. Kreuzer, *Polym.* **3**, 51 (2011).
- [78] T. Seki, K. -Y. Chiang, C. -C. Yu, X. Yu, M. Okuno, J. Hunger, Y. Nagata and M. Bonn, *J. Phys. Chem. Lett.* **11**, 8459 (2020).
- [79] C. -C. Yu, M. Okuno, T. Seki, T. Ohto, X. Yu, V. Korepanov, H.-o. Hamaguchi, M. Bonn, J. Hunger and Y. Nagata, *Nat. Commun.* **11**, 5977 (2020).
- [80] Y. Park, J. H. Lim, J. Y. Lee, and H. Kang, *J. Phys. Chem. C* **123**, 9868 (2019).
- [81] Y. Park, H. Kang, and H. Kang, *Angew. Chem. Int. Ed.* **56**, 1046 (2017).
- [82] P. Delaney and J. C. Greer, *Appl. Phys. Lett.* **84**, 431 (2004).
- [83] M. Ya. Amusia and A. S. Baltenkov, *Phys. Lett. A* **360**, 294 (2006).
- [84] Jun-ya Sorimachi and S. Okada, *Jpn. J. Appl. Phys.* **55**, 04EP02 (2016).
- [85] L. Onsager, *J. Am. Chem. Soc.* **58**, 1486 (1936).
- [86] S. A. Sorenson, J. G. Patrow, and J. M. Dawlaty, *J. Am. Chem. Soc.* **139**, 2369 (2017).
- [87] Y. Park, H. Kong, and H. Kang, *Angew. Chem. Int. Ed.* **56**, 1046 (2017).
- [88] D. Jackson, *Classical Electrodynamics*, Wiley, New York (2007).
- [89] L. Liu, L. Li, Q. Li, and Q. Zeng, *Phys. Chem. Chem. Phys.* **19**, 4751 (2017).

- [90] X. Peng, L. Chen, J. Dang, C. Wang, and Y. Mo, *Chem. Nano Mat.* **8**, e202200405 (2022).
- [91] D. Penn, *Phys. Rev.* **128**, 2093 (1962).
- [92] G. K. Gueorguiev, J. M. Pacheco, and D. Tomanek, *Phys. Rev. Lett.* **92**, 215501 (2004).
- [93] N. L. Matsko and I. A. Kruglov, *J. Phys. Chem. Lett.* **12**, 11873 (2021).
- [94] E. D. Sloan and C. A. Koh, *Clathrate Hydrates of Natural Gases*, 3ed. CRC Press, Boca Raton (2008).
- [95] S. Scheiner, *Hydrogen Bonding: A Theoretical Perspective*, Oxford University Press, New York (1997).
- [96] N. Sun, et al., *J. Phys. Chem. A* **121**, 2620 (2017).
- [97] G. S. Fanourgakis, E. Para, and S. S. Xantheas, *J. Chem. Phys.* **121**, 2655 (2004).
- [98] P. Kumar and N. Sathyamurthy, *J. Phys. Chem. A* **115**, 14276 (2011).
- [99] P. K. Chattaraj, S. Bandaru, and S. Mondal, *J. Phys. Chem. A* **115**, 187 (2011).
- [100] R. F. W. Bader, *Atoms in Molecules: A Quantum Theory*, Oxford University Press, Oxford (1990).
- [101] E.R. Johnson, S. Keinan, P.M. -Sánchez, J.C. -García, A. J. Cohen and W. Yang, *J. Am. Chem. Soc.* **132**, 6498 (2010).
- [102] G. Saleh, C. Gatti, and L. Lo Presti, *Comput. Theor. Chem.* **998**, 148 (2012).
- [103] L. J. Bartolotti, D. Rai, A. D. Kulkarni, S. P. Gejji, and R. K. Pathak, *Comput. Theor. Chem.* **1044**, 66 (2014).

- [104] N. D. Gurav, A. D. Kulkarni, S. P. Gejji, and R. K. Pathak, *J. Chem. Phys.* **142**, 214309 (2015).

Chapter 5

Future Prospects

The structure, response and properties of nanoconfined water in a uniform and static electric field are studied. The response of nanoscopic linear and ring structured water to the applied uniform and static electric field is explored from the perspective of potential device applications that exploit their in-field structural behaviors, field-dependent characteristics, and other attributes of technological relevance. A careful consideration of the results may prove beneficial for the development of water-based molecular devices. Furthermore, the response of a molecule to an external field when it is nanoconfined in molecular cages comprised of hydrogen bonds and covalent bonds is investigated. Towards the end of the thesis, the shielding property of small-size fullerene cages and the potential indications of field-induced controlled release of CO molecule from the building blocks of the CO clathrate hydrates are explored. Both have enormous technological implications.

While the major objectives of the thesis have been accomplished, however, thorough evaluations including experimental validations are highly warranted. The future prospective research endeavors in this field are anticipated to encompass experimental demonstration, or at the very least, molecular dynamics simulation studies closely reflecting the realistic scenario in the actual practical setup. We strongly believe that this thesis provides the necessary background for future studies and stimulates further discussions in the areas related to the topics covered herein. In addition, the following are a few of the topics that have been identified to merit additional research.

- ☞ (1) Chapter 2: Additional investigation on structured water nano-chains.

- ✎ (2) Chapter 3: Experimental study of water nano-rings in electric field.
- ✎ (3) Chapter 4: Study of shielding properties of molecular cages.
- ✎ (4) Chapter 4: Study of field-assisted gas release in clathrate hydrates.
- ✎ (5) Chapter 4: Photolysis of nano-confined water.

The aforementioned key points highlight the directions for future endeavors. Nevertheless, some justifications are necessary, and thus the following brief overview is important.

(1) The results inferred from our work on the structured water nano-chains are based on the DFT-based computations, which begin with geometry optimization in an electric field and continue until the structure is stretched to the point where the extreme distortion of the geometry under field prevents further optimization. The observed field-induced hydrogen bond strengthening is particularly significant in the development of flexible and self-healing device components in the water-based electronics, where external stimuli resulting from an electric field may prove crucial [1, 2]. Nevertheless, the molecular dynamics simulation studies on the stability of such nanoscopic structured water is crucial in making a way forward to demonstrate its manifestation and realize its application in a physical setup. An in-depth study of structured water chains is important in understanding the formation mechanism of a floating water bridge [3, 4], its molecular scale structure and extraordinary stability. Any characteristics of the structured water chains that are of technological relevance may be unveiled and discussed.

(2) Although the DFT computations have yielded intriguing results regarding water nano-rings, further experimental research is needed to fully comprehend how these nano-sized water ring formations manifest and what makes them unique for technological uses. While such ring water structures may not emerge in a free-standing form, their formation on the hydrophobic surface cannot be ruled out.

Examining the quantum interference effect in these types of hydrogen-bonded ring topologies and how it could show up in their conduction properties would be absolutely fascinating. Due to the significant field-induced dipole moment, such ring structures would undoubtedly find applications in dipole-based devices, where the orientation of the dipole moment determines the conduction behavior [5]. It is envisaged that with the profound technical advancements that enable local manipulation of water molecules on the surface by STM tip, the ring water structures may be suitably designed for use in device applications [6, 7]. To that end, experimental enthusiasts may benefit from the results of our present study.

(3) One of the concerns with a molecular device's operation is interference with local stray electric fields, which can alter the device's characteristics and impair its functionality [8]. This is where the significance of the concepts of shielding and shielding efficiency of cage structures become important considerations. Molecular cages are particularly important to consider for the purpose due to their minuscule size and ease of device integrity. Fullerenes, among other cage structures, are very promising because of covalent bonding forming the cage structure, which offers geometric stability against distortion from external influences like electric fields. When field enhancement is present inside the cage, it can be used to enable some odd interactions that result in exotic molecular species that would not otherwise be possible to find in a free environment. Detailed theoretical and experimental studies are indispensable for quantifying the shielding efficiency of covalent bond molecular cages. This greatly helps in improving the performance and reliability issues of the molecular devices.

(4) Experimental study of the electric field-assisted gas release in clathrate hydrates is limited [9]. However, this is the area of study that holds enormous promise, primarily because of the possibility of precise manipulation of the clathrate hydrates to release enclosed gas under controlled conditions. Viewed from another perspective, the field-assisted gas release at a specific site would open up a new

avenue in the precision anchoring of molecular devices making them compatible for large-scale integration. This is because, when an electric field is employed, dipole-bound clathrate hydrates may be precisely adjusted and directed at the microscopic scale, something that is not possible when temperature and pressure are used. In particular, field-assisted gas capture or release in hydrogen or methane clathrate hydrates holds tremendous technological significance, with uses ranging from in-situ nanoscopic operation for a specific purpose to onboard applications. For field-assisted gas capture or release in clathrate hydrates, a comprehensive computational and experimental investigation at the microscopic level is highly desirable.

(5) Water in nano-confinement has several interesting features that make it an ideal setup for photolysis. In particular, high proton conductivity and low dielectric constant are very appealing. To that end, a vertically stacked bilayer hetero-junction formed by two transition-metal dichalcogenide (TMD) materials, such as MoS_2 and WSe_2 , may be taken into consideration. This bilayer material exhibits a direct band gap [10] and has a strong photon absorption capability. Under illumination and immersion in water, photoexcitation generates long-lived interlayer excitons, which cause the MoS_2 layer to form the hole layer and the WSe_2 layer to form the electron layer. In a suitable setup [11, 12], like the spiral pyramid-shaped bilayer TMDs exposed to sunlight, which has nanoscopic space between the consecutive turns with oppositely charged faces, the protons produced as a byproduct of the oxidation reaction at the positively charged face take advantage of the characteristics of nano-confined water to efficiently reach the negatively charged face, where they are reduced to hydrogen gas. It is therefore possible to increase the efficiency of hydrogen production if the unique characteristics of nano-confined water are properly exploited. It is imperative that thorough calculations be performed in order to validate the intended mechanism that exploits the characteristics of nano-confined water. Furthermore, any experimental demonstration would provide a fresh impetus for the development of an efficient hydrogen gas

production system using the nano-confinement technologies.

Although there are endless related subjects yet to explore, we feel that the insights gleaned from the present endeavor stand as a testament to the pursuit of further understanding and the relentless quest for the above-intended subjects. We believe that the hitherto unexplored areas examined over the years, culminating in the form of this thesis, represent the true physical characteristics of the nano-confined water in an electric field. Nonetheless, a meticulous and comprehensive evaluation using the molecular dynamics simulations and the state-of-the-art experimental methods is essential to validate our results. Though more research is undoubtedly necessary, and with the race for rapid development of sophisticated experimental techniques, we hope that the outcomes of the systematic research work presented in this thesis will either be realized soon or at the very least put to the test. Until then, some of our predictions made and the trends we've observed in the present endeavor shall continue to remain elusive.

References

- [1] B. Guo, J. Zhang, K. P. Ananth, S. Zhao, X. Ji, and J. Bai, *Compos. Part A*, **133**, 105863 (2020).
- [2] X. Wan, T. Mu, and G. Yin, *Nano-Micro Lett.* **15**, 99 (2023).
- [3] L. B. Skinner, C. J. Benmore, B. Shyam, J. K. R. Weber, and J. B. Parise, *Proc. Natl. Acad. Sci. U.S.A.* **109**, 16463 (2012).
- [4] E. C. Fuchs, J. Woisetschläger, A. D. Wexler, R. Pecnik, and G. Vitiello, *Water*, **13**, 602 (2021).
- [5] S. Tanimoto, M. Tsutsui, K. Yokota, and M. Taniguchi, *Nanoscale Horiz.* **1**, 399 (2016).
- [6] J. Guo, K. Bian, Z. Lin, and Y. Jiang, *J. Chem. Phys.* **145**, 160901 (2016).
- [7] L. Zhao, M. Tao, K. Sun, Y. Tu, D. Yang, Z. Wang, M. Shi, and J. Wang, *Appl. Surf. Sci.* **515**, 145973 (2020).
- [8] H. Kashani, M. Giroux, I. Johnson, J. Han, C Wangm and M. Chen, *Matter*, **1**, 1077 (2019).
- [9] Z. Li, M. Lyu, H. Jonsson, and C. R. -Petruck, *J. Phys. Chem. Lett.* **12**, 10410 (2021).
- [10] N. Lu, H. Guo, L. Li, J. Dai, L. Wang, W. -N. Mei, X. Wu, and X. C. Zeng, *Nanoscale*, **6**, 2879 (2014).
- [11] T. H. Ly, J. Zhao, H. Kim, G. H. Han, H. Nam, and Y. H. Lee, *Adv. Mater.* **28**, 7723 (2016).
- [12] Y. Zhao, C. Zhang, D. D. Kohler, J. M. Scheeler, J. C. Wright, P. M. Voyles, and S. Jin, *Science*, **370**, 442 (2020).

Index

A

AIM analysis, 13

B

B3LYP, 9

B97D, 11

Binding energy, 59

Buckingham expansion, 16

C

Chemical hardness, 135

Chemical stability, 60, 135

Clathrate hydrates, 116

CO hydrates, 118

Confinement, 25

Cooperativity, 55, 133

D

DFT, 5

Dipole moment, 55, 125, 139

Dipole screening, 124

E

Electronegativity, 135

Electrophilicity, 135

Energetic stability, 59

Energetics, 134

F

Field effects, 16

Field response, 19

Frontier molecular orbitals, 62, 90

H

Hexamer structured water chain, 54

Hohenberg and Kohn, 6

HOMO-LUMO gap, 59, 90, 125

Hydrogen bond length, 55, 139

Hydrophobic surface, 26

I

Infrared spectra, 92

Interaction energy, 134

IR spectra, 126

K

Kohn-Sham ansatz, 8

L

Local dipole moment, 57

Local field, 129

M

M06-2X, 12

Molecular cages, 27

N

Nanoscale water bridge, 29

NCI, 12, 88, 136

O

Onsager's reaction field model, 129

Optimization, 20

P

Pentamer structured water chain, 52

Petration factor, 129

Photolysis, 30

polarizability, 125

R

Raman spectra, 98

RDG analysis, 14, 88, 136

Reaction field, 130

Reactivity indices, 18, 134

S

Single-file water chain, 50

Structural evolution, 139

T

Tetramer structured water, 51

Threshold field, 61, 90

V

Vibrational response, 126

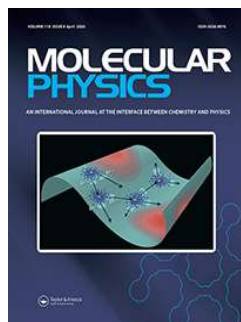
Vibrational Stark effect, 22

W

Weak interaction, 10

X

XC functional, 9



Molecular Physics

An International Journal at the Interface Between Chemistry and Physics

ISSN: 0026-8976 (Print) 1362-3028 (Online) Journal homepage: <https://www.tandfonline.com/loi/tmph20>

Structured water chains in external electric fields

Smita Rai, Nayan Sharma & Dhurba Rai

To cite this article: Smita Rai, Nayan Sharma & Dhurba Rai (2020) Structured water chains in external electric fields, Molecular Physics, 118:8, e1662957, DOI: [10.1080/00268976.2019.1662957](https://doi.org/10.1080/00268976.2019.1662957)

To link to this article: <https://doi.org/10.1080/00268976.2019.1662957>



View supplementary material [↗](#)



Published online: 10 Sep 2019.



Submit your article to this journal [↗](#)



Article views: 326



View related articles [↗](#)



View Crossmark data [↗](#)



Citing articles: 2 View citing articles [↗](#)

RESEARCH ARTICLE



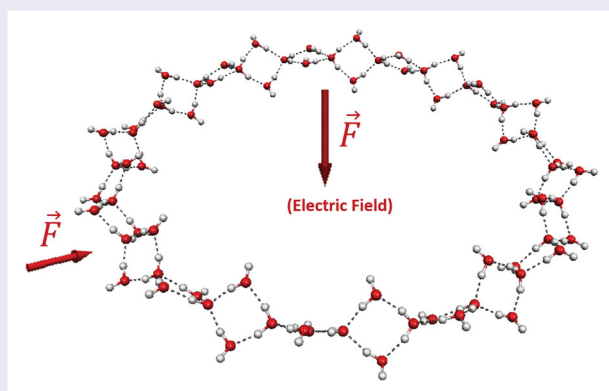
Water nano-rings in electric fields

Smita Rai^a, Dhurba Rai^a and Vivekanand V. Gobre^b

^aDepartment of Physics, Sikkim University, Samdur, India; ^bSchool of Chemical Sciences, Goa University, Taleigao, India

ABSTRACT

Density functional theory (DFT)-based calculations were performed for 36, 72 and 108 water molecules forming twisted ribbon-like nano-ring structures of diameter 1.54, 3.10 and 4.56 nm, respectively. We explore the electric field evolution of the structure, energetics and stability of the water nano-ring structures that are essentially symmetric and non-polar, or less-symmetric and polar, hydrogen-bonded clusters. The results suggest that for fields applied perpendicular to the ring, larger rings are more susceptible to the field influence, while fields applied parallel to the ring quickly transform the ring structures into arbitrary ones, regardless of the ring size. Infrared and Raman spectral analysis of local modes demonstrate the typical vibrational response of water molecules to various H-bonding environments and applied fields, providing a spectroscopic signature that can be used to identify the manifestation of such H-bonded ring networks. Our study underscores the implications of the nano-sized ring water clusters, which have the potential to be exploited in a variety of device applications.



ARTICLE HISTORY

Received 29 August 2023
Accepted 17 October 2023




KEYWORDS


Water nano-ring; electric field; dipole moment; HOMO–LUMO gap; vibrational modes

1. Introduction

Confined water in nano space exhibits properties different from those of bulk. Such water with characteristic hydrogen bonding between the water molecules is found in biological nanochannels like aquaporins [1], microporous crystalline compounds like zeolites [2], or carbon-based hollow structures like carbon nanotubes (CNTs) [3–5], fullerenes [6–8], nanocavities [9], and metal–organic frameworks (MOFs) [10]. In such systems, the confining framework and the water molecules interact through van der Waals and other non-bonding interactions. Significant experimental and theoretical

studies have been carried out on the water clusters to understand hydrogen bonding structure in bulk water and the origin of anomalies that it exhibits under different physical conditions [11–15], and beyond [16–18]. However, despite enormous scientific and technological advancements, water continues to be a mysterious liquid with unusual properties for which there are no satisfactory explanations. Nevertheless, the study of water clusters provides an ideal route for understanding the structural changes, bonding mechanisms, and properties that occur as the size of the clusters grows from small to larger ones towards the bulk limit. Thus, the study of

CONTACT Dhurba Rai  drai01@cus.ac.in  Department of Physics, Sikkim University, Samdur 737102, India; Vivekanand V. Gobre  vvgobre@gmail.com School of Chemical Sciences, Goa University, Taleigao 403206, India

 Supplemental data for this article can be accessed online at <https://doi.org/10.1080/00268976.2023.2273977>.



Certificate of Completion

THIS ACKNOWLEDGES THAT

Smita Rai

has completed the workshop:

Introduction to Gaussian: Theory and Practice

Delhi, India

January 8-12, 2018

Michael Frisch

MICHAEL FRISCH, PRESIDENT



**1st International e-Conference on
Recent Advances in Physics & Materials Science-2020
(IC-RAPMS-2020)**

Organized by

Kurseong College, Darjeeling, West Bengal, India-734203

In collaboration with

St. Joseph's College, Darjeeling, West Bengal, India-734104



*This is to certify that **Ms. Smita Rai**
of*

Sikkim University

*has participated in the 1st International e-Conference on Recent Advances in Physics & Materials Science
(IC-RAPMS-2020) held during 9 & 10 July, 2020 and presented a paper entitled*

Structured water chains in external electric fields

Samir Bal

**Dr. Samir Bal
Principal
Kurseong College**

Amit Shankar

**Dr. Amit Shankar
Convener**

Fr. Dr. Donatus Kujur S.J.

**Fr. Dr. Donatus Kujur S.J.
Principal
St. Joseph's College**





CERTIFICATE OF PARTICIPATION

IS PRESENTED TO

Smita Rai

for participating and presenting a poster on Water Nano-Rings in Electric Field: DFT Study in National Symposium on Condensed Matter, Materials Science and Statistical Physics in Presidency University, Kolkata on April 28-29, 2023.

Sankar Bose

*Dean
Faculty of Natural and
Mathematical Sciences
Presidency University*

Arunava Chakrabarti

*Head of the Department
Department of Physics
Presidency University*